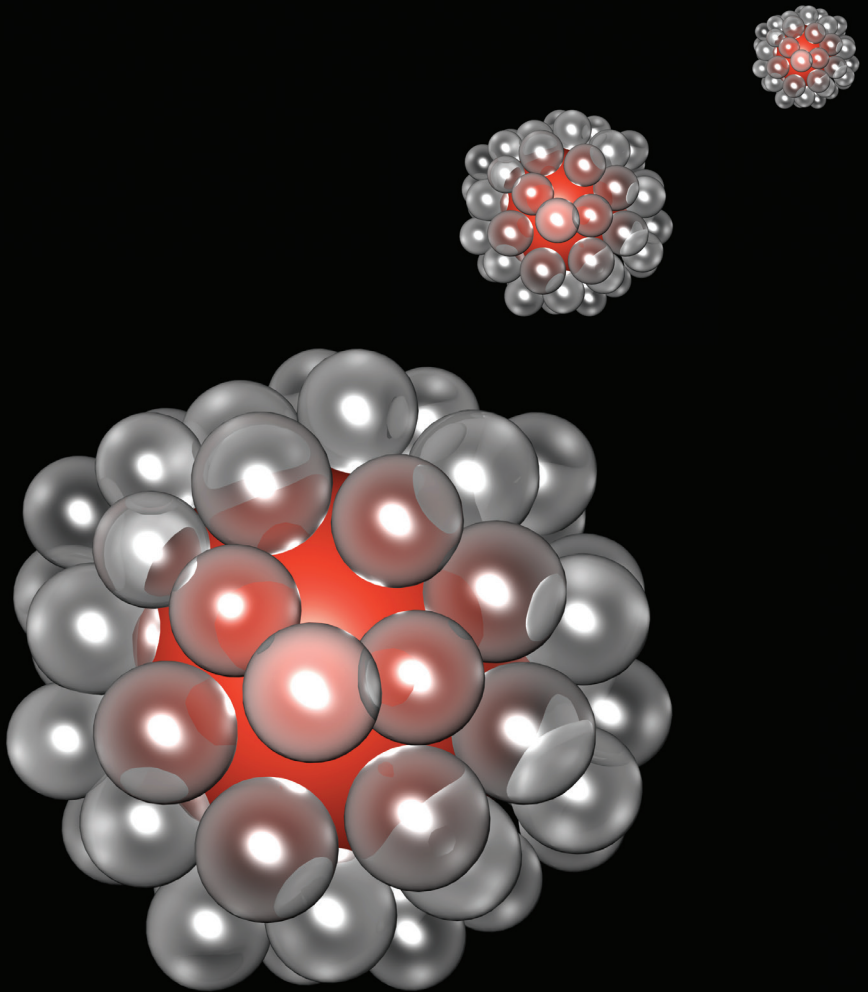


StemBells

A novel stem cell delivery platform
using microbubbles and ultrasound



Tom **Kokhuis**

StemBells

**A novel stem cell delivery platform using
microbubbles and ultrasound**

Tom Johannes Albertus Kokhuis

Colophon

ISBN: 978-94-610-8811-6

Cover design: Tom Kokhuis

Printed by: Gildeprint, Enschede, the Netherlands

©2014, T.J.A. Kokhuis, the Netherlands

Except for the following chapters:

Chapter 2,4: ©2014 John Wiley & Sons, Inc.

Chapter 3: ©2013 Elsevier B.V. 2013

All rights reserved. No part of this publication may be reproduced, stored in a retrieval system, or transmitted, in any form, or by any means, electronic, mechanical, photocopying, recording, or otherwise, without the prior consent from the author.

StemBells

A novel stem cell delivery platform using
microbubbles and ultrasound

StemBells

Nieuwe stamceltherapie
met bellen en ultrageluid

Proefschrift

ter verkrijging van de graad van doctor aan de
Erasmus Universiteit Rotterdam
op gezag van de
rector magnificus

Prof.dr. H.A.P. Pols

en volgens besluit van het College van Promoties.

De openbare verdediging zal plaatsvinden op
woensdag 19 november 2014 om 15.30 uur door

Tom Johannes Albertus Kokhuis
geboren te Geesteren, Overijssel



Samenstelling promotiecommissie

Promotoren

Prof.dr.ir. N. de Jong

Prof.dr.ir. A.F.W. van der Steen

Prof.dr. M. Versluis

Overige leden

Prof.dr. A. van der Lugt

Prof.dr.ing. G.C. van Rhoon

Prof.dr.ir. H. Wijkstra

These studies were performed at the Department of Biomedical Engineering of the Erasmus Medical Center, Rotterdam, the Netherlands. The research is supported by the Dutch Technology Foundation STW, which is part of the Netherlands Organisation for Scientific Research (NWO) and partly funded by the Ministry of Economic Affairs (project 10507). Financial support by the Dutch Heart Foundation for the publication of this thesis is gratefully acknowledged.

Financial support

The publication of this thesis was financially supported by:

- Erasmus Medical Center
- Dutch Heart Foundation
- Oldelft Ultrasound
- Dutch Technology Foundation STW
- FBD Bankmensen
- TL Makelaardij Almelo
- Bracco Suisse SA

The importance of mutual understanding

An entrepreneur submitted to the Department of Trade and Industry (DTI) a proposal for collaboration with academia in the prediction of racehorse winners. Enthusing on the value of such a project, the Department financed three years of research, whereby the entrepreneur provided field data, which was subsequently analysed by the Statistics group of a Mathematics department at a certain university. At the end of three years, the university submitted a written report to the entrepreneur and the DTI which they stated was '100%' certain. Passing rapidly over the pages of formulae, the entrepreneur read the one-line conclusion at the end: "One horse always wins." Somewhat dismayed, but still feeling the project had worth, the entrepreneur approached the Science and Engineering Research Council (SERC). They suggested that, since the problem of a fast racehorse might reduce to the drag factor of the horse, the circulation of the blood etc., for a more practical input the entrepreneur should collaborate with the Fluid Dynamics group at the university. The project went ahead along these lines, and at the end of three years the entrepreneur turned up to take possession of the report, which he would personally pass on to the SERC. "It is 100% certain to predict the result?" he asked, as the researchers handed over the thick bound copy. "No, no" they replied, "This is a practical science, and nothing is ever certain. But we have 95% confidence in the winner that the theory predicts for any given race." The entrepreneur beamed. "That's good enough for me!" he smiled, and opening the report, read the first line: *Assume a spherically-symmetric horse...*

In: *The Acoustic Bubble*, 1992
Timothy G. Leighton

Contents

1	General introduction and thesis outline	1
1.1	Bubbles	1
1.2	Medical microbubbles	2
1.3	Outline of this thesis	6
2	DSPC or DPPC as main shell component influences ligand distribution and binding area of lipid-coated targeted microbubbles	9
2.1	Introduction	11
2.2	Materials and Methods	13
2.3	Results	19
2.4	Discussion	24
2.5	Conclusions	28
3	Secondary Bjerknes forces deform targeted microbubbles	29
3.1	Introduction	31
3.2	Theoretical framework and numerical modeling	34
3.3	Materials and Methods	40
3.4	Results	44
3.5	Discussion	55
3.6	Conclusions	61
3.7	Appendix	63
4	Intravital microscopy of localized stem cell delivery using microbubbles and acoustic radiation force	67
4.1	Introduction	69
4.2	Materials and methods	71
4.3	Results	76
4.4	Discussion	79
4.5	Conclusions	83
5	On the dynamics of StemBells: microbubble-conjugated stem cells for ultrasound-controlled delivery	85
5.1	Introduction	87
5.2	Materials and Methods	87
5.3	Results and Discussion	89

5.4	Conclusions	94
6	Directing stem cells to the infarcted area using targeted microbubbles: StemBells.	97
6.1	Introduction	99
6.2	Materials and methods	100
6.3	Results	108
6.4	Discussion	112
7	Conclusions and future perspectives	117
	Bibliography	129
	Summary	155
	Samenvatting	159
	Dankwoord	163
	Publications and presentations	167
	PhD portfolio	175
	About the author	179

General introduction and thesis outline

1.1 Bubbles

Bubbles are omnipresent. It is the popping of bubbles present in the water that produces the characteristic sound of meandering brooks, boiling water [1] and breaking waves at the beach. The popping of bubbles can generate great forces, an effect which is employed in ultrasound baths to remove dirt and biofilms from all kind of objects, such as jewelry. In the ocean, pistol shrimps make use of the violent collapse of bubbles, produced by the rapid closure of their special snapper claw, to daze their preys¹[2]. Furthermore, without the presence of tiny (carbon dioxide) bubbles, soft drinks would not have the sparkling taste and beers not a foamy head. Bubbles are also good adsorbers of dirt, which is used in industry to clean greasy machinery and piping².

The behaviour of bubbles has intrigued scientists and engineers for centuries. Leonardo da Vinci (1452-1519) already studied the motion of bubbles in water, as evidenced by the sketches in his manuscript *The Codex Hammer* [3]. Da Vinci was puzzled by the fact that millimeter-sized air bubbles rising in water as a result

¹See also: BBC Weird Nature: "Stunning shockwave"
<http://www.bbc.co.uk/programmes/p00z9l6q>

²See also:
<http://www.mitsubishielectric.com/company/environment/ecotopics/water/microbubbles/>

of buoyancy follow a spiraling path, instead of rectilinear, a phenomenon later referred to as *Leonardo's Paradox* [4]. A few centuries later another great scientist, Lord Rayleigh (1842 - 1919), investigated the formation of vapour bubbles (or cavities) in liquid, an effect known as *cavitation*. At that time, the cause of the deterioration of ship propellers due to the formation of pits was still unknown. The research of Rayleigh, by order of the British admiralty, showed that the implosion of vapour bubbles created by the fast rotating propeller, were the cause of the damage. The research resulted in a theoretical description of the dynamics of bubbles in a liquid [5]. The equation was elaborated afterwards by Milton S. Plesset (1908-1991) [6], resulting in the well-known Rayleigh-Plesset equation, on which many models for bubble dynamics are still based today. The work led to a better understanding of the behaviour of bubbles, which also turned to be very useful outside the field of marine research.

1.2 Medical microbubbles

Ultrasound contrast imaging

Since decades, bubbles also find their application in medical science. The reason for this however was rather coincidental. In 1968 it was observed that the intracardiac injection of a saline (NaCl) solution produces a cloud of echoes improving the contrast during echocardiography. This contrast improvent was attributed to the presence of "mini bubbles" within the solution [7]. Since then, special microbubble ultrasound contrast agents (UCA) were developed to boost the contrast during echography. In 1991 the first microbubble UCA became commercially available as Echovist® (Bayer Schering Pharma, Berlin, Germany) and consisted of an air core coated with galactose shell, a sugar commonly found in the diet. The coating serves to prevent coalescence and reduces dissolution of the bubbles. Since then, continuous improvements have been made to the formulations, for instance by using low solubility gases, such as perfluorobutane (C₄F₁₀), improving the persistency of the bubbles. Instead of a sugar coating, microbubbles can have

a biodegradable phospholipid, polymer or protein shell [8]. After injection, microbubbles are retained within the circulatory system for several minutes [9], until being cleared by the immune system [10]. The size of microbubbles typically varies between 1 – 10 μm , i.e. smaller than red blood cells, allowing them to pass unhindered through the capillary vasculature of the body. The resonance frequency of these microbubbles is close to the imaging frequencies used in clinical ultrasound scanners (2 - 10 MHz). Therefore, microbubbles respond to the incoming ultrasound waves with volumetric oscillations, generating a secondary ultrasound wave, that can be picked up again by the ultrasound scanner. It is this vibration, in combination with the large difference in the acoustical impedance with the surrounding tissue, that is responsible for the enhanced contrast generated by the microbubbles during ultrasound scanning. Parallel with the improvements in the fabrication of microbubbles, new microbubble detection techniques were developed (for an overview of the most common techniques see [11]). These techniques employ the non-linear scattering properties of vibrating bubbles [12], facilitating a better discrimination from the surrounding (linear-responding) tissue. The combination of stable bubbles and improved detection techniques, makes ultrasound contrast imaging nowadays an excellent tool for studying blood perfusion, e.g. for cardiac applications [13].

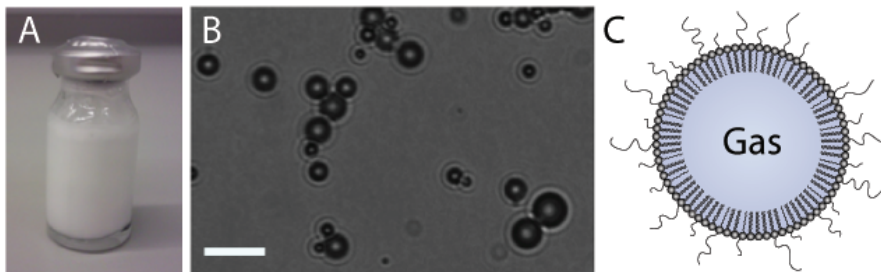


FIGURE 1.1: (A) Vial of homemade phospholipid-coated microbubble suspension (B) Microscopic image of the microbubbles, the scalebar represents 10 μm (C) Molecular architecture of a phospholipid coated microbubble

In this thesis, we have focused on phospholipid-coated bubbles, as this group comprises the majority of the microbubbles that are currently approved or in clinical trials [14]. Figure 1.1A shows a vial of homemade phospholipid-coated

microbubble suspension with the characteristic milky appearance; Figure 1.1B shows a microscopic image of the microbubbles, the scalebar represents 10 μm . The molecular architecture of the coating of the bubbles is depicted in Figure 1.1C. The gas core is surrounded by a monolayer of phospholipids, with their polar head (grey circles) directed outward and the apolar tail inward. The coating also contains a polymer brush, which serves as an repulsion barrier inhibiting microbubble fusion and acts as a steric barrier to minimize interaction with blood components and improve the circulation time *in vivo* [8].

In the 1990s, the first microbubbles equipped with ligands to specific molecular markers were introduced [15, 16]. This addition of ligands to the shell creates so-called *targeted* or *functionalized* microbubbles which can be tailored to specific molecules inside the body, for instance markers for a disease. Targeted microbubbles bind selectively to the areas of interest, which will produce a strong echo during ultrasound examination, facilitating molecular ultrasound imaging [17]. In 2012, the first molecular ultrasound imaging study in humans was completed [18]. In this study it was shown that microbubbles targeted against the Vascular Endothelial Growth Factor Receptor 2 (VEGF-R2), which has been identified as a marker for the progression and aggressiveness of prostate cancer, can improve the detection and localization of prostate cancer. Therefore, molecular ultrasound imaging might eventually replace the invasive and painful biopsy investigation, by which prostate cancer is still diagnosed today.

Therapeutic applications

Besides diagnostic, bubbles can also be used for therapeutic applications. Microbubble-mediated local drug delivery obtained significant attention since its discovery in 1997 [19]. It was shown that vibrating microbubbles can cause a transient increase in the cell membrane permeability [20], an effect often referred to as *sonoporation*. Sonoporation will therefore increase the internalization and efficacy of the co-administered drug within the insonified area. The exact mechanism by which microbubbles increase the cell permeability is still under investigation, but several

mechanisms including pore formation, stimulated endocytosis and opening of cell-cell junctions have been proposed (for a review see [21]). Microbubbles can also be used as drug carriers, e.g. by incorporating drugs in the bubble or in the bubble coating [22]. The drugs can then be released upon ultrasound insonification in both a spatially and temporally controlled manner. Another promising therapeutic application of vibrating microbubbles is the enhancement of clot dissolution, a process known as *sonothrombolysis* [14]. Rapid recovery of the blood flow after a stroke or heart attack is important to improve the outcome. The option to dissolve clots with ultrasound and microbubbles opens possibilities for more patency at an earlier stage. The feasibility of the technique for the treatment of patients suffering from an acute myocardial infarction is currently assessed in a prospective clinical trial in Amsterdam, the Netherlands [23, 24].

Acoustic radiation force

The intravascular distribution of microbubbles resembles that of red blood cells, with the majority of the bubbles being located around the centerline of the vessel [25]. This axial migration of the microbubbles within vessels impedes a successful interaction between the ligand and the receptor at the endothelium, especially in larger vessels. To improve the delivery of microbubbles, researchers made use of the *acoustic radiation force*: a propulsive force experienced by bubbles when subjected to a periodic sound field. The existence of such a force was already reported in 1906 by the Norwegian scientist Vilhelm F.K. Bjerknes [26]:

"A pulsating body in a synchronously oscillating current is subject to the action of a resultant force, the direction of which is that of the acceleration in the current at the time when the pulsating body has its maximum volume."

Vilhelm F.K. Bjerknes (1862-1951),
in: *Fields of force*, 1906

The resultant acoustic radiation force experienced by bubbles due to the primary sound field from the transducer is therefore often referred to as the *primary Bjerknes force*. Because pulsating bubbles also become sound sources themselves, there also exists a mutual interaction between pulsating bubbles, which is referred to as *secondary radiation force* or *secondary Bjerknes force*.

The propulsory effect of the primary Bjerknes force allows for the translation of microbubbles from the center of the vessel toward the target endothelium, enforcing contact between the microbubble and target [27–29]. Ultrasound application can therefore actively assist in the delivery of microbubbles to the area of interest, prior to the diagnostic imaging or therapeutic insonification step.

1.3 Outline of this thesis

The research described in this thesis focuses on the application of targeted microbubbles. The first chapters deal with some of the more fundamental aspects of targeted microbubbles. Chapter 2 describes the effect of the phospholipid composition of the shell on the distribution of the ligands, binding area and bound microbubble shape. Chapter 3 reports on the mutual interaction between vibrating adherent microbubbles during ultrasound application. We demonstrate there is a strong interaction (secondary Bjerknes force) between neighbouring bubbles, which can eventually detach the microbubbles from their target surface. Experimental translations are compared to the predictions of a simplified hydrodynamic model. In Chapter 4, 5 and 6 we describe the development of a novel therapeutic application of targeted microbubbles: local stem cell delivery. By coating stem cells with targeted microbubbles, echogenic complexes called *StemBells* can be created which are sensitive to acoustic radiation forces. The feasibility of this ultrasound-mediated cell delivery technique was studied using intravital microscopy in a chicken embryo, which is described in Chapter 4. Chapter 5 focuses on the vibrational dynamics of *StemBells*, which were studied using high-speed optical imaging. A theoretical model, based on a modified Rayleigh-Plesset

equation, was developed to corroborate our experimental results. To investigate whether our novel stem cell delivery technique also resulted in improved cardiac functioning, we performed a long-term functional study in rats using an acute myocardial infarction model. The results of this study are discussed in Chapter 6. Concluding remarks and future perspectives are presented in Chapter 7.

DSPC or DPPC as main shell component influences ligand distribution and binding area of lipid-coated targeted microbubbles

Klazina Kooiman¹, Tom J.A. Kokhuis^{1,2}, Tom van Rooij¹, Ilya Skachkov¹, Alex Nigg³, Johannes G. Bosch, Antonius F.W. van der Steen^{1,2,4,5}, Wiggert A. van Cappellen³ and Nico de Jong^{1,2,4}

¹Biomedical Engineering, Thorax Center, Erasmus MC, Rotterdam, The Netherlands

²Interuniversity Cardiology Institute of the Netherlands, Utrecht, The Netherlands

³Erasmus Optical Imaging Centre, Department of Pathology, Erasmus MC, Rotterdam, the Netherlands

⁴Acoustical Wavefield Imaging, Delft University of Technology, Delft, The Netherlands

⁵Shenzhen Institutes of Advanced Technology, Shenzhen, China

European Journal of Lipid Science and Technology, 116(9):1217-1227, 2014

Abstract

Ultrasound contrast agents (UCA) consist of gas-filled coated microbubbles with diameters of 1 – 10 μm . Targeted UCA can bind to biomarkers associated with disease through coating-incorporated ligands, making ultrasound molecular imaging possible. The aim of our research was to compare the ligand distribution, binding area, and bound microbubble shape of 1,2-distearoyl-sn-glycero-3-phosphocholine (DSPC) based and 1,2-dipalmitoyl-sn-glycero-3-phosphocholine (DPPC) based lipid-coated microbubbles using super-resolution microscopy. Ligand distribution was studied by conjugating the fluorescent streptavidin Oregon Green 488 to the biotinylated microbubbles. An inhomogeneous streptavidin distribution was found when DSPC was the main coating lipid. When DSPC was replaced by DPPC, a more homogeneous streptavidin distribution was observed. Binding area of targeted microbubbles was studied using biotinylated microbubbles bound to a streptavidin-coated surface. DSPC microbubbles had a significantly smaller binding area than DPPC microbubbles. Whereas the bound DSPC microbubbles remained spherical, the DPPC microbubbles were dome-shaped. This study reveals that lipid-coated microbubbles differ in ligand distribution, binding area, and bound microbubble shape solely on the basis of their main lipid component.

2.1 Introduction

Ultrasound imaging is a widely used non-invasive diagnostic imaging modality. In the 1990s the first ultrasound contrast agents (UCA) became available for clinical use [30, 31]. UCA consist of a fluid comprised of coated gas microbubbles with diameters between 1 and 10 μm . Upon intravenous administration, UCA stay within the vascular tree as they are too large to extravasate [31, 32]. Initially, UCA were mainly used to improve diagnostic ultrasound imaging, such as enhancing the contrast for the detection of the heart wall border. Current applications also include detailed analysis of blood volume and flow in cardiology and radiology, for example to detect myocardium perfusion defects and tumors [32–35]. Recent research has also shown the potential of UCA for therapeutic applications such as drug delivery and molecular imaging [36–38]. The UCA shell improves the lifetime of the microbubbles after intravenous administration. Current clinically available UCA are comprised of a lipid monolayer or albumin coating with a gas core composed of a high molecular weight inert gas, for example perfluorobutane (C_4F_{10}) [39, 40]. Ligands can be conjugated to the UCA shell, resulting in targeted or functionalized microbubbles, making ultrasound molecular imaging possible. Molecular imaging is an emerging field and aims to image molecular changes associated with diseases by imaging biological processes in living systems at the cellular and molecular level. Preclinically, ultrasound molecular imaging has shown its potential for inflammation, ischemia-reperfusion injury, angiogenesis, and thrombi [37, 38]. Recently, the successful first human phase 0 clinical trial for prostate cancer was presented [18], using a lipid coated microbubble targeted to vascular endothelial growth factor receptor 2 (VEGFR2). For ultrasound molecular imaging, two steps are important: 1) binding of the targeted microbubble to the biomarker, and 2) imaging of the bound targeted microbubble using ultrasound. Several groups have focused on increasing binding of targeted microbubbles by applying acoustic radiation force to push the bubbles to the biomarkers on the vessel wall [28], deflating the microbubble which results in excess shell surface area [41], conjugating two [42] or three [43] different ligands to the coating, or

varying ligand linker length [44]. Studies have not focused on the distribution of the ligand on the microbubble coating, even though Borden et al reported an heterogeneous ligand distribution, where the ligand was located in fine lines between domains [45]. However, this was reported for a microbubble $\sim 20 \mu\text{m}$ in size, which is not a clinically relevant size. It is not thoroughly investigated whether ligand distributions are also heterogeneous for microbubbles of clinically relevant sizes or for different lipid coating compositions. A homogeneous ligand distribution could be more advantageous than a heterogeneous ligand distribution due to an increased probability of a successful binding event, especially in large vessels with high blood flow [46]. Research is ongoing to distinguish bound from unbound targeted microbubbles using ultrasound [47–49], and to determine the binding force of bound targeted microbubbles [50–52]. Larger targeted microbubbles have a larger binding area and therefore a higher binding force as more bonds can be formed. At the same time, the shear forces on the bound microbubble as a result of blood flow will also be higher for larger microbubbles, and thus persistence after binding will be lower for larger microbubbles. Modeling has predicted the optimal targeted microbubble size for binding to be $2 - 4 \mu\text{m}$ in diameter [53]. However, the shape of the bound microbubble was assumed spherical, but it is not known if targeted microbubbles remain spherical upon binding. The aim of our research was to compare the ligand distribution, binding area, and bound microbubble shape of 1,2-distearoyl-sn-glycero-3-phosphocholine (DSPC) based and 1,2-dipalmitoyl-sn-glycero-3-phosphocholine (DPPC) based lipid-coated targeted microbubbles using high-resolution microscopy. The DSPC microbubble, which we previously used in a drug delivery study [54], resembles the clinically approved UCA SonoVueTM in coating composition (coating composition: polyethylene glycol (PEG4000; Molecular weight (MW) 4000), DSPC, and 1,2-dihexadecanoyl-sn-glycero-3-phospho-(1'-*rac*-glycerol) (DPPG) [55]). The DPPC based microbubbles resemble the clinically approved UCA Definity[®] (coating composition: DPPC, 1,2-dihexadecanoyl-sn-glycero-3-phosphate (DPPA), and 1,2-dipalmitoyl-sn-glycero-3-phosphoethanolamine(polyethylene glycol) (DPPE-PEG5000; Molecular weight 5000) [56]).

2.2 Materials and Methods

Materials

DPPC, 1,2-distearoyl-sn-glycero-3-phosphoethanolamine-N-carboxy(polyethylene glycol) (DSPE-PEG2000; MW 2000), 1,2-distearoyl-sn-glycero-3-phosphoethanolamine-N-biotinyl(polyethylene glycol) (DSPE-PEG2000-biotin; MW 2000) were purchased from Avanti Polar Lipids, USA. DSPC, polyoxyethylene (40) stearate (PEG-40 stearate) were obtained from Sigma. Perfluorobutane (C_4F_{10}) was purchased from Linde Gas Benelux. Streptavidin Oregon Green 488, streptavidin Oregon Green 514, 1,1'-dioctadecyl-3,3,3',3'-tetramethylindodicarbocyanine perchlorate (DiD), 100 nm yellow-green fluorescent beads were obtained from Molecular Probes (F8803), Life Technologies. PD-10 desalting columns were purchased from GE Healthcare Bio-Sciences. Custom polycarboxylate hydrogel-coated (1.5 μm) quartz glasses (30 mm in diameter, 0.22 mm thickness), amine coupling kit (containing EDC \cdot HCl, activation buffer, borate elution buffer, and quenching buffer) were purchased from XanTec bioanalytics GmbH, Germany.

Methods

Preparation of microbubbles

Biotinylated lipid coated microbubbles (composition in mol %: DSPC or DPPC 59.4; PEG-40 stearate 35.7; DSPE-PEG2000 4.1, DSPE-PEG2000-biotin 0.8) with a C_4F_{10} gas core were made by sonication for 10 seconds using the method described by Klivanov et al [57]. DSPC microbubbles refer to the microbubbles with DSPC as main coating component, DPPC microbubbles to those with DPPC as main coating component.

Microbubble size distribution

Microbubble size distributions were measured on a Coulter Counter Multisizer 3 (n=3) (Beckman Coulter, Mijdrecht, the Netherlands). A 50 μm aperture tube was used, allowing quantification between 1 and 30 μm using a linear spacing between the 256 channels. Polydispersity of the samples was assessed by the SPAN, defined as $(d_{90\%}-d_{10\%})/d_{50\%}$ where $d_{90\%}$, $d_{10\%}$ and $d_{50\%}$ are the microbubble diameters below which 90%, 10%, and 50% of the cumulative amount of microbubbles is found.

Ligand distribution within microbubble coating

Ligand conjugation

The ligand fluorescent streptavidin Oregon Green 488 was conjugated to the biotinylated microbubbles as described by Lindner et al [58]. Briefly, microbubbles were washed by flotation by placing the microbubble solution in a 3 mL syringe with one-way tap and leaving to stand. After 45 minutes, the supernatant was drained, and the microbubbles were suspended in 1 mL of PBS saturated with C_4F_{10} and drained. Then, 110 μL of streptavidin (1 mg/mL) was quickly spinned using a Microspin FV-2400 (Biosan Ltd), and 90 μL of the streptavidin solution was added to 7×10^8 microbubbles. This was incubated on ice for 30 minutes. Excess streptavidin was washed by flotation as above.

Ligand distribution visualization

The streptavidin-conjugated microbubbles were mounted in 87% glycerol (v/v in PBS) and were visualized three dimensionally with super resolution on a Leica TCS 4Pi confocal laser-scanning microscope [59, 60] using a matched pair of aligned opposing 100x glycerol HCX PL APO objective lenses (Numerical aperture 1.35). The lenses were aligned using 100 nm fluorescent beads [61]. Image stacks were recorded as y-stacked xz -scans in a green (500-550 nm) spectral channel. Each xz -slice consisted of 512x512 pixels with a pixel size of 30x30 nm and was averaged

twofold. The y -distance between neighboring xz -slices was 90 nm. An Argon laser (488 nm) was used for excitation. Volume rendering of the image stacks was performed using the "voltex" function of the program AMIRA (Version 5.2.2, FEI, Mérégnac Cedex, France).

Semi-automatic analysis of ligand distribution heterogeneity

The heterogeneity of the ligand distribution was analyzed with custom software written in MATLAB (Mathworks, Natick, MA, USA) using the 3D-stacks described above. For both microbubble types, 30 randomly chosen microbubbles were analyzed. In a first step, the center point of the microbubble was manually annotated in one of the xz -slices. Next, the program computed the radial intensity profiles for 100 angles (i.e. at multiples of $2\pi/100$ radians), using the manually selected center as starting point. After this, a circle was fitted through the intensity maxima using a MATLAB routine based on the method as described by Taubin [62], from which the radius (R_{fit}) and origin (O_{fit}) of the fluorescent contour within the xz -slice were obtained. All the pixels located within 90 nm from R_{fit} , defined as the region of interest (ROI), were included in the heterogeneity analysis. The ROI was subdivided in 32 angular parts (i.e. each $\pi/16$ radians); for each angular part the mean fluorescence pixel intensity (I_{part}) was calculated. This procedure was repeated for a range of xz -slices spatially distributed around the equatorial plane of the bubble, whereby the origin of the best circle fit (O_{fit}) within a slice was used as starting center point for the radial intensity profiles in the adjacent xz -slice. Only xz -slices with a value for R_{fit} which was larger than 75% of the value of R_{fit} in the equatorial plane of that particular bubble were included in the analysis. This was because towards the caps of the microbubbles, the xz -slices had a fluorescence pattern of filled circles, instead of a fluorescent rim surrounding a dark core, which could not be processed with the same contour tracking algorithm. On average, 35 xz -slices were included per bubble, resulting in on average $35 \cdot 32 = 1120$ angular parts per bubble, from which the median part intensity per bubble (\hat{I}_{median}) was calculated. An individual angular part was classified as an inhomogeneity when the absolute difference between the mean fluorescence intensity of this part (I_{part}) and the median part intensity of the bubble

(\hat{I}_{median}) was more than two-third of the value of \hat{I}_{median} (i.e. $|I_{part} - \hat{I}_{median}| > 2/3 \times \hat{I}_{median}$). From this, the percentage of parts classified as an inhomogeneity per microbubble, being a measure for inhomogeneous ligand distribution, was calculated for both microbubble types.

Statistics

Statistical analysis was performed using IBM SPSS Statistics 20. First, Shapiro-Wilk normality tests were performed to determine if the standard deviation and mean were significantly different from a normal distribution. Both distributions were not normally distributed (DSPC: $p = 0.001$, DPPC: $p < 0.001$) and hence we used non-parametric testing. The Mann-Whitney U test was used to identify whether the percentages of parts classified as an inhomogeneity were significantly different between both microbubble types. A p-value < 0.05 was regarded as significant.

Binding area of targeted microbubbles

Targeted microbubbles and surface coating

The binding area of biotinylated microbubbles and a streptavidin surface was studied by adding the lipid dye DiD to the microbubbles before sonication and covalently linking fluorescent streptavidin Oregon Green 514 to the hydrogel-coated quartz glass. For the covalent linkage, streptavidin was first dissolved in acetate buffer (2 mM, pH 5.4) (1 mg/mL), and desalted using a PD-10 desalting column according to the manufacturer's instructions. After desalting, the concentration of streptavidin was determined spectrophotometrically using a calibration curve on a VarioskanTM Flash (Thermo Scientific). The desalted streptavidin was covalently linked to the hydrogel-coated quartz glasses according to the instructions of the manufacturer. Briefly, the quartz glass was placed in a 6-well plate (BD) and incubated with 2.5 mL of borate elution buffer (1 M sodium chloride, 0.1 M sodium carbonate buffer, pH 10) for 10 min on a rotating shaker (model KM-2, Edmund Bühler GmbH, 125 Mot 1/min). After three washes with 3 mL MilliQ,

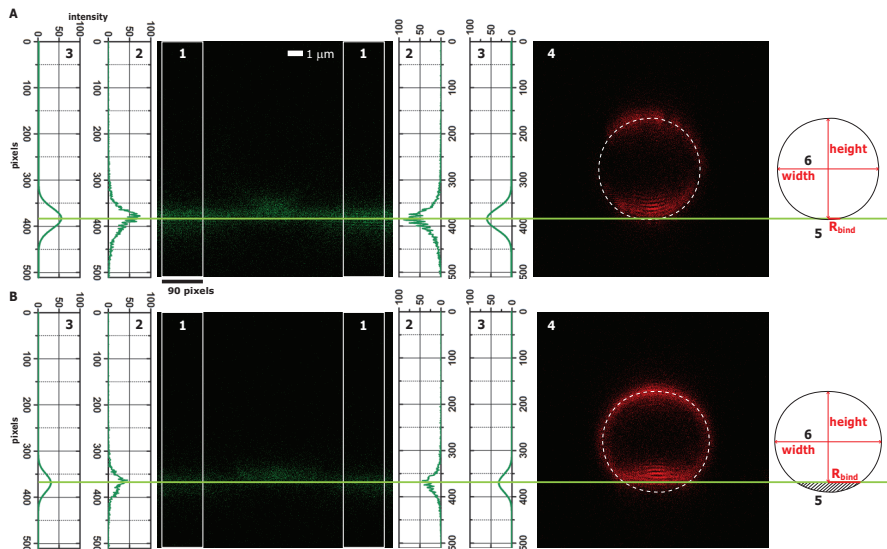


FIGURE 2.1: Method of calculation of binding area and microbubble shape for targeted microbubbles. Example of a DSPC microbubble (A) and a DPPC microbubble (B).

the glasses were rinsed with 2 mL of 1.0% (w/v) EDC · HCl in activation buffer, and then incubated for 15 minutes in the dark in 3 mL of 1.0% (w/v) EDC · HCl in activation buffer. After three washes with MilliQ, the glasses were incubated for two hours with 1.6 mL of desalted streptavidin Oregon Green 514 (40 $\mu\text{g}/\text{mL}$) on the rotating shaker. This was followed by 30 minutes incubation with 2.5 mL quenching buffer. Then, the glasses were washed three times with PBS. Just before adding the microbubbles, the glass was washed once with PBS containing calcium and magnesium (PBS^{+/+}) and the microbubbles were allowed to adhere to the streptavidin-coated surface by flotation. For this, the glasses were placed in a custom-made holder with a 10 mL volume filled with PBS^{+/+}. The microbubbles were injected under the glass using a bended blunt 19 G-needle. After 5 minutes, the glass was gently washed three times with PBS^{+/+} using a 3 mL plastic Pasteur pipet, and mounted in 87% (v/v) glycerol such that the bound targeted microbubbles were on top of the coated surface.

Targeted microbubble and surface visualization

The microbubbles and streptavidin coating were visualized three dimensionally with the 4Pi setup as described under 2.2.3.2. Image stacks were recorded as y -stacked xz -scans in a green (500-550 nm) and far red (647-703 nm) spectral channel. An Argon laser (488 nm) and HeNe laser (633 nm) were used for excitation. Volume rendering of the image stacks was performed using the "voltex" function (for microbubbles) and "isosurface" function (for streptavidin) of the program AMIRA.

Analysis of binding area and bound microbubble shape

The microbubble binding area was calculated from the cross-section of the streptavidin plane with the bubble surface using Fiji (<http://fiji.sc/wiki/index.php/Fiji>; [63]) as illustrated in Figure 2.1A for a DSPC microbubble, and in Figure 2.1B for a DPPC microbubble. First, the streptavidin plane was determined by the z -position in the xz -plane where the green fluorescence intensity was maximal. This was done at the left and right of the plane (90 pixels wide) as illustrated by the white boxes labeled 1 in Figure 2.1. The edges of the recording were chosen to avoid possible interference with the microbubble signal. The fluorescence intensity derived at the two fixed z -positions is given in 2 in Figure 2.1, and the Gaussian fit through the data in 3 in Figure 2.1. The maximum was derived from the Gaussian fit and averaged between the two z -positions. The difference between the left and right maxima was 0.2 ± 2.2 pixels (i.e. 6 ± 66 nm; $n = 47$), which was within the z -resolution of the microscope (~ 130 nm [59, 60]), indicating the streptavidin plane was level within 0.3 degrees. The microbubble contour was determined in both the xz and yz -plane of the far red channel by manually drawing an ellipsoid through the top half of the microbubble as illustrated by 4 in Figure 2.1 for the xz -plane. Then, the cross section between the streptavidin plane and the microbubble contour was determined in both planes (5 in Figure 2.1), from which the radius of the binding area (R_{bind}) was derived. The microbubble radius before binding to the streptavidin surface (R_0) was calculated by $R_0 = \sqrt[3]{3V_0/4\pi}$, where V_0 is the volume of the total ellipsoid minus the part of the ellipsoid below the streptavidin

plane (hatched in schematic of microbubble in Figure 2.1). A linear trend line was fitted through the origin and the data points using GraphPad InStat verion 5.04 (GraphPad Software). To characterize the shape of the bound microbubbles, we derived the width and height of the bound microbubble, as illustrated in 6 in Figure 2.1. The Mann-Whitney U test (IBM SPSS Statistics 20) was used to identify whether the shape of the bound microbubbles was significantly different between both microbubble types. A p-value < 0.05 was regarded as significant.

2.3 Results

Size distribution

The size distribution of the streptavidin-conjugated DSPC and DPPC microbubbles is shown in Figure 2.2. The number weighted mean diameter was $4.2\ \mu\text{m}$ for the DSPC and $3.9\ \mu\text{m}$ for the DPPC microbubbles. The volume weighted mean diameter of $8.0\ \mu\text{m}$ for the DSPC microbubbles was also higher than the diameter of $7.7\ \mu\text{m}$ for the DPPC microbubbles. These small differences were also reflected in the SPAN, which was 1.4 for DSPC and 1.3 for DPPC microbubbles.

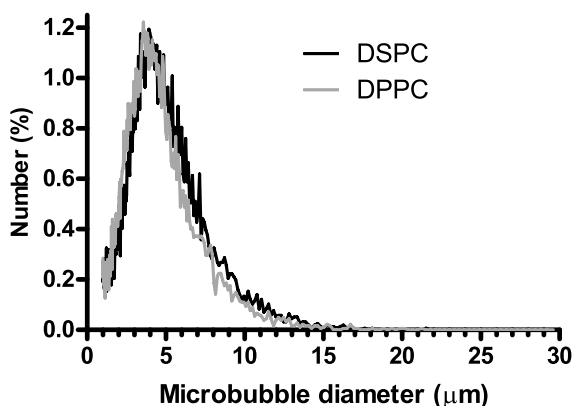


FIGURE 2.2: Size distribution of microbubbles.

Ligand distribution within the coating

The distribution of the ligand streptavidin was studied in 66 DSPC and 55 DPPC microbubbles. As shown in Figure 2.3A, we observed heterogeneous ligand distributions for the DSPC microbubbles. Since streptavidin only conjugates to DSPE-PEG2000-biotin, a high fluorescence intensity area indicates a higher concentration of this lipid in that part of the coating. Also, areas with hardly any fluorescence were detected, indicating an exclusion of the DSPE-PEG2000 lipid and hence a little higher concentration of one or both of the other coating components, namely DSPC and PEG-40 stearate. Interestingly, different patterns were found for microbubbles of the same size, for example Figure 2.3A4 and A5. Whereas the microbubble in Figure 2.3A4 had larger areas of hardly any fluorescence and no areas of higher fluorescence intensity, the microbubble in Figure 2.3A5 had small areas of hardly any fluorescence and small areas of higher fluorescence intensity. Although we observed patchy heterogeneous fluorescence distributions in all DSPC microbubbles, some microbubbles showed more heterogeneity than others. Two of the most heterogeneous DSPC microbubbles are shown in Figure 2.3A3 and 3A5. The microbubble in Figure 2.3A3 has a large area that contains hardly any fluorescence, whilst the microbubble in Figure 2.3A5 has a more patchy character with areas that differ in fluorescence intensity, as areas with minimum and maximum intensity were observed. In contrast to the DSPC microbubbles, the DPPC microbubbles showed a more uniform ligand distribution, indicated by the more homogeneous fluorescence, as shown in Figure 2.3B. Dark domains with hardly any fluorescence were not observed. Occasionally a higher fluorescence intensity spot was observed (see Figure 2.3B5 and B6), indicating a higher concentration of the DSPE-PEG2000 lipid in that area. The observation of a more uniform lipid coating in case of DPPC microbubbles was confirmed by the semi-automatic image analysis counting the percentage of parts being classified as an inhomogeneity (see Figure 2.4). A significant higher percentage of parts classified as an inhomogeneous were found for DSPC microbubbles than for DPPC microbubbles. No relation was found between the inhomogeneity and the microbubble diameters.

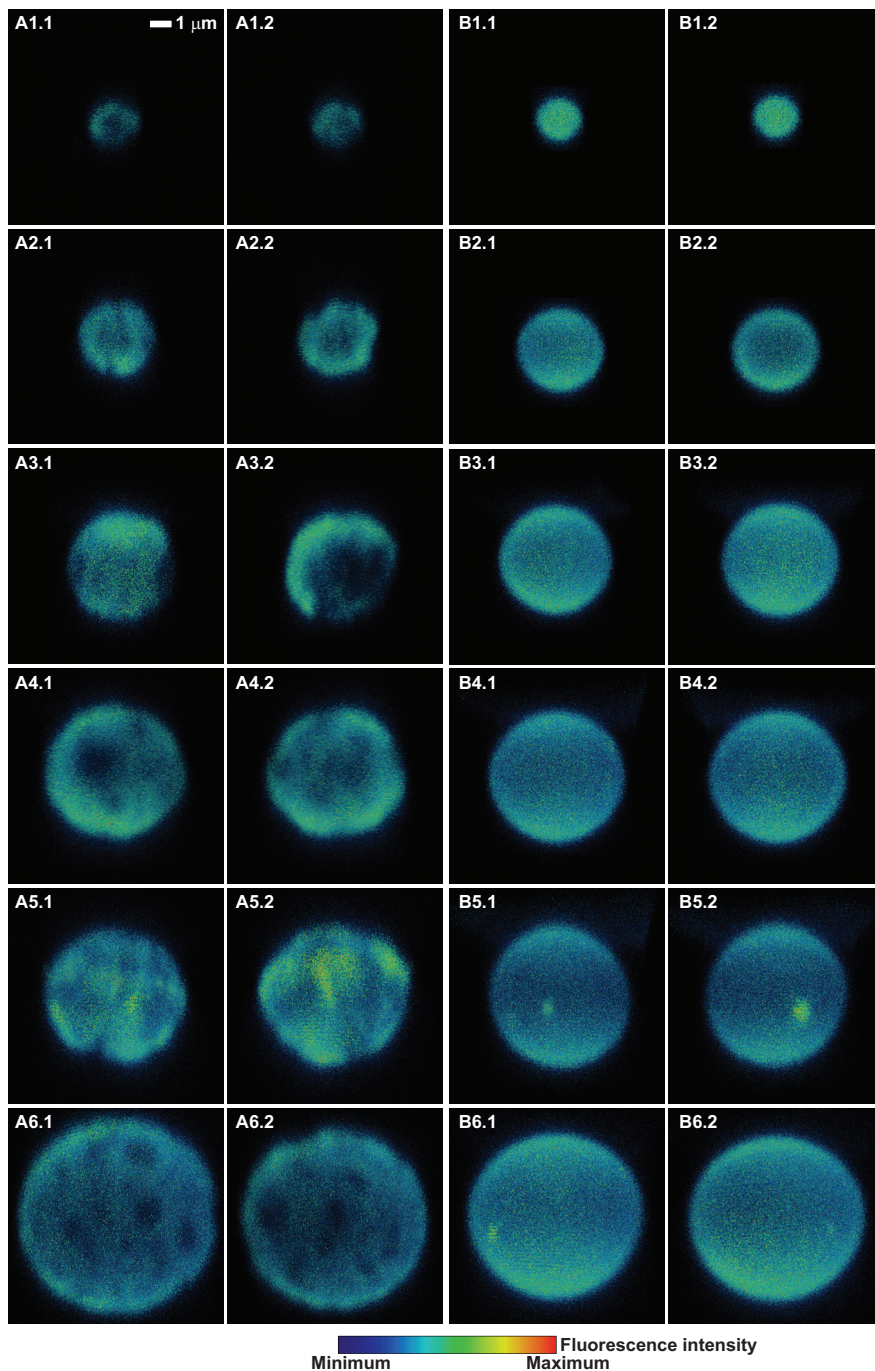


FIGURE 2.3: Ligand distribution on DSPC microbubbles (A1-6) and DPPC microbubbles (B1-6). Two views (.1 and .2) out of the 3D reconstructions are shown for each microbubble. Smallest shown microbubble is 1.7 μm in diameter, largest is 7.5 μm . The full 3D reconstructions of microbubbles A4, A5, B4, and B5 are given as Supporting information Video S1, S2, S3, and S4, respectively.

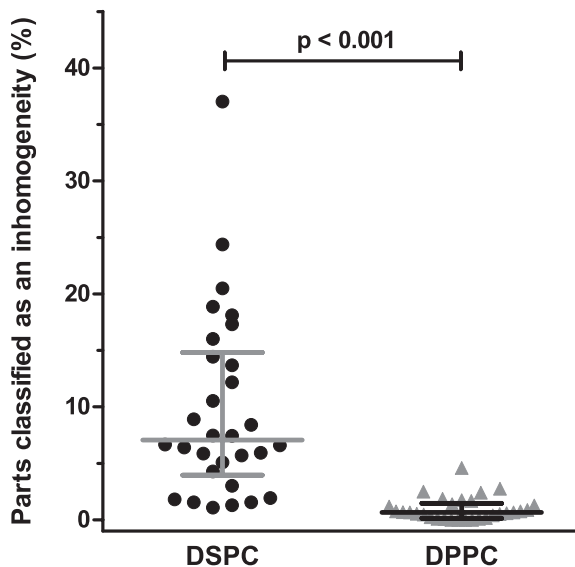


FIGURE 2.4: Homogeneity of ligand distribution for DSPC ($n=30$) and DPPC microbubbles ($n=30$). Shown are the medians with the interquartile range.

Binding area of targeted microbubbles

Figure 2.5A shows examples of targeted DSPC microbubbles (in red) bound to the streptavidin-coated surface (in green) and Figure 2.5B shows examples of targeted DPPC microbubbles. In these cases, the streptavidin was covalently linked to the hydrogel-coated quartz glass, and we observed no streptavidin fluorescence on the microbubble surface. This in contrast to when we coated an Opticell membrane with streptavidin by physisorption (as previously described [50]), when we also observed streptavidin on both the DSPC and DPPC microbubbles, most likely due to rolling of the microbubbles before binding.

When the binding area of the targeted microbubbles to the covalently linked streptavidin was calculated, we found a factor of ~ 2.3 smaller binding radii for DSPC microbubbles (factor ~ 5.3 for binding area) than for DPPC microbubbles, based on the slope of the fit as shown in Figure 2.6. For both microbubble types, the binding radii increased with the microbubble size, albeit that the increase was larger

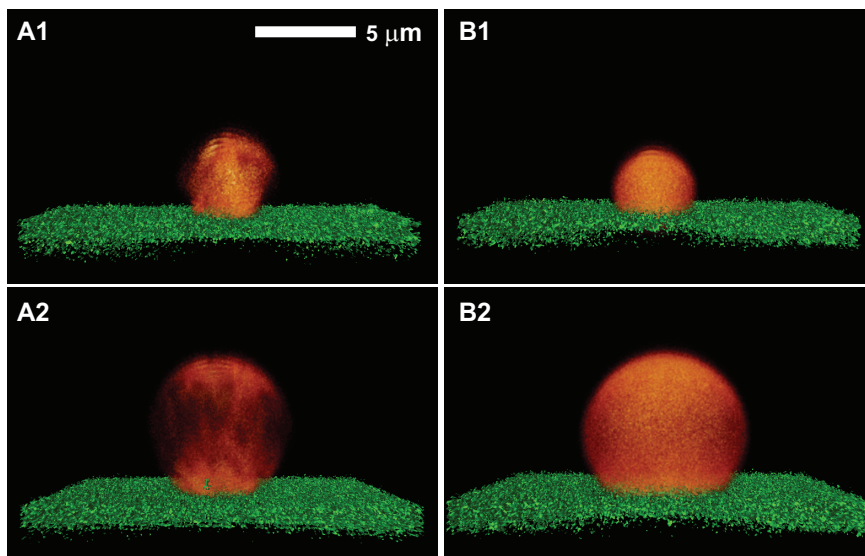


FIGURE 2.5: Targeted DSPC (A) and DPPC (B) microbubbles (red fluorescent) bound to streptavidin-coated surface (green fluorescent; covalently linked).

for the DPPC than for the DSPC microbubbles. To characterize the shape of the bound microbubbles, we derived the width to height ratio of the microbubbles, as illustrated in Figure 2.7. The width to height ratio was significantly smaller for the DSPC microbubbles than for the DPPC microbubbles, indicating the DSPC

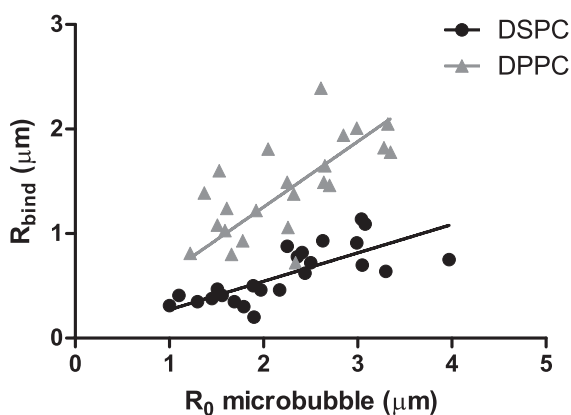


FIGURE 2.6: Binding area radius, R_{bind} , as function of radius for targeted microbubbles, R_0 . Trend line through DSPC data has slope of 0.3; slope is 0.6 for DPPC.

microbubbles were more spherical than the DPPC microbubbles, which resembled a dome-shape.

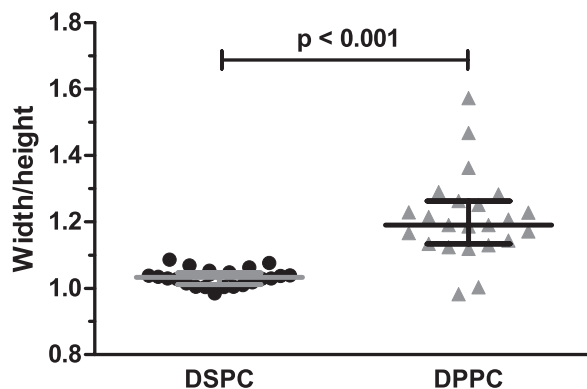


FIGURE 2.7: Width to height ratio for targeted microbubbles. Shown are the medians with the interquartile range.

2.4 Discussion

To the best of our knowledge, this is the first study that determined the binding area of targeted microbubbles and the dependence of that binding area on the lipid coating composition. The binding area was largest for the DPPC microbubbles which also had a significantly more homogeneous ligand distribution than the DSPC microbubbles. Whereas the bound targeted DSPC microbubbles remained spherical, the DPPC microbubbles were dome-shaped. We used fluorescence to study the ligand distribution and the binding area of the lipid-coated targeted microbubbles. Using streptavidin Oregon Green 488, we observed differences in ligand distribution between the two microbubble types. The patches with hardly any fluorescence observed on the DSPC microbubbles are likely due to the absence of the DSPE-PEG2000-biotin and unlikely due to quenching of the Oregon Green 488 dye as a result of a very high concentration of streptavidin in that area. In fact, for fluorescent avidins to which no biotin is bound, it is known that fluorophore quenching occurs because the dye interacts with amino acid residues in the

biotin-binding pocket. Upon biotin binding, this interaction is blocked, resulting in enhanced fluorescence [64, 65]. According to the manufacturer, the streptavidin molecule used in our study was labelled with 2-5 Oregon Green molecules, which is a fluorinated analogue of fluorescein. As streptavidin has four biotin binding pockets, multiple biotins could have bound per streptavidin if the biotinylated lipid concentration was high enough, resulting in an even higher, not a lower, fluorescence intensity in areas with a high concentration of the DSPE-PEG2000-biotin lipid. This may have caused the higher intensity patches observed in the shell of the DSPC microbubbles. Surface microstructures are common for lipid-coated microbubbles, and have also been reported for a mixture of two out of the three components of our DSPC microbubbles, namely a mixture of DSPC and DSPE-PEG2000 [45, 66], and a mixture of DSPC and PEG-40 stearate [67, 68]. As lipid coatings on microbubbles are monolayers, the results of microbubble studies can be compared to monolayer films formed at an air/water interface. The observed heterogeneous lipid distributions in the coating of our and previously reported microbubbles is in agreement with studies of lipid monolayer films as immiscibility has been reported for all different mixtures of DSPC and DSPE-PEG2000. PEG-40-stearate is reported to be in the expanded phase only and mixes with other expanded phase lipids, but is immiscible with lipids in the condensed phase [67]. Since DSPC is in the condensed phase only [69], PEG-40 stearate is immiscible with this lipid. DSPE-PEG2000 can be in the expanded or condensed phase [69]. When it is in the expanded phase it will be miscible with PEG-40 stearate, but when it is in the condensed phase it will be immiscible with PEG-40 stearate. Lozano and Longo [69] showed miscibility of DPPC and DSPE-PEG2000 in both the expanded and condensed phase, suggesting this mixture would result in a homogeneous lipid coating for microbubbles. When we replaced DSPC by DPPC, we indeed observed a homogeneous distribution of DSPE-PEG2000 within the coating of the microbubbles. This supports our assumption that in our experiments the lipids are immiscible (DSPC microbubbles) or miscible (DPPC microbubbles) which is the explanation for respectively the presence and absence of surface microstructures. The occasionally observed small higher intensity fluorescence spots

on the DPPC microbubbles could be explained by folds or buckles that form locally on the microbubble coating due to excess lipids [70]. In our study we observed different patterns for DSPC microbubbles of the same size, which is in contrast to what has previously been reported for microbubble coating mixtures of DSPC and PEG-40 stearate [68]. A different coating composition for our microbubbles could be the reason, as could be the variation in lipid concentrations per microbubble. Both could also be the explanation why we did not observe the DSPE-PEG2000 in fine lines between domains, as previously reported by others [45]. Surface microstructures resulting in inhomogeneous lipid distributions could be disadvantageous for microbubbles used as drug carrier system when drugs are conjugated to the lipids. One such drug carrier system is drug-filled liposomes conjugated to the coating via DSPE-PEG2000 [71]. A homogeneous DSPE-PEG2000 distribution would be optimal to avoid competition during the conjugation of the liposomes. A maximum amount of drug can therefore be loaded onto the microbubbles, which based on our current study favors DPPC over DSPC as main lipid for the coating. Several strategies have been reported to improve binding of targeted microbubbles [28, 41–44], but these have not included varying the lipid coating composition. In addition to differences in ligand distribution, we also found differences in binding area between both microbubble types. DSPE-PEG2000 is often used to conjugate ligands to the microbubble coating, either by coupling via streptavidin or by covalent coupling [72]. For the binding area experiment, we used the lipid dye DiD to fluorescently label the microbubbles. As this type of lipid dye co-localizes with the DSPE-PEG2000-biotin lipid [45], it is a good indicator for the binding area. We indeed observed a similar dye pattern as when streptavidin Oregon Green 488 was conjugated to the microbubbles, namely a heterogeneous distribution for the DSPC microbubbles and a homogeneous distribution for the DPPC microbubbles. It needs to be further investigated whether a heterogeneous or homogeneous ligand distribution or a smaller or larger binding area is best for binding probability, and binding strength of targeted microbubbles. Differences between small microvessels, where microbubbles will be in close proximity to the vessel wall on all sides, and larger vessels, where the blood flow is also significantly higher [46],

will have to be taken into account when investigating the binding probability. Although the binding area for the DSPC microbubbles was smaller, this does not imply that the binding force is weaker. As the ligand distribution is heterogeneous throughout the coating of DSPC microbubbles, we also frequently observed areas with high concentrations of the ligand. More ligand molecules within a small area could therefore have a binding force equal to a lower amount of ligand molecules distributed over a larger area. The shape of the bound microbubble could also be very important as the effect of blood shear forces is expected to be stronger on spherical than on domed-shape microbubbles. This again favors DPPC over DSPC for targeting microbubbles. The domed shape of the DPPC microbubbles suggests a more elastic coating, which is in line with DPPC having a lower elastic compressibility modulus than DSPC [73, 74]. A limitation of our study is that microbubbles bound under static conditions using biotin-streptavidin as artificial ligand-biomarker pair. Our future research will focus on binding targeted microbubbles to disease related biomarker under flow conditions. However, our findings can be used to improve the binding of targeted microbubbles and aid in the ongoing research to distinguish bound from unbound targeted microbubbles using ultrasound. Overvelde showed that the binding itself results in a resonance frequency shift and a 30% difference in vibration amplitude [47]. It is therefore expected that a difference in binding area will also change the acoustic behavior. Acoustic stability of the bound targeted microbubbles is also important, and will have to be further investigated for both microbubble types. The relation between the acoustic behavior of microbubbles and surface microstructures is unknown [70] and will be subject for our future studies. Nonetheless, heterogeneous lipid distributions could be contributing to differences in acoustical responses of similar sized bubbles [75]. In addition, our findings may be used for modeling, as modeling has greatly aided the understanding and prediction of non-targeted microbubble behavior in an acoustic field [39], but is still in its infancy for targeted microbubbles.

2.5 Conclusions

This study reveals that lipid-coated microbubbles differ in DSPE-PEG2000 lipid and ligand distribution, binding area, and bound microbubble shape solely on the basis of their main lipid component. A homogeneous ligand distribution, larger binding area and dome-shape upon binding could be advantageous for binding of targeted microbubbles, thereby favoring DPPC over DSPC as main lipid for UCA for ultrasound molecular imaging.

Acknowledgements

The authors are grateful to Prof. Dr. A.L. Klibanov from the University of Virginia, Cardiovascular Division, Charlottesville, Virginia, USA for discussions about the microbubble preparation. The authors thank the Erasmus Optical Imaging Centre of Erasmus MC for use of their facilities, and Michiel Manten from the Dept. of Biomedical Engineering, Erasmus MC for technical assistance. We also thank Prof. dr. A. Blume, Dept. Biophysical Chemistry, Martin Luther University Halle-Wittenberg, Germany, for discussions about the results, and Paul van den Berg from the Dept. of Clinical Genetics, Erasmus MC, for the spectrophotometer measurements, and Dr. E. Gedig from XanTec bioanalytics GmbH, Germany, for discussions about the covalent coating of streptavidin to the quartz glasses. This research is supported by the Center for Translational Molecular Medicine and the Dutch Heart Foundation (PARISk), the Dutch Technology Foundation STW, and NanoNextNL, a micro and nanotechnology consortium of the Government of the Netherlands and 130 partners.

Supporting information

Supplementary data related to this article can be found online at:

<http://dx.doi.org/10.1002/ejlt.201300434>

Secondary Bjerknes forces deform targeted microbubbles

Tom J.A. Kokhuis^{1,2}, Valeria Garbin³, Klazina Kooiman¹, Benno A. Naaijken^{2,4},
Lynda J.M. Juffermans^{2,5}, Otto Kamp^{2,6}, Antonius F.W. van der Steen^{1,2,7,8},
Michel Versluis⁹ and Nico de Jong^{1,2,7}

¹Biomedical Engineering, Thorax Center, Erasmus MC, Rotterdam, The Netherlands

²Interuniversity Cardiology Institute of the Netherlands, Utrecht, The Netherlands

³Department of Chemical Engineering, Imperial College London, UK

⁴Department of Pathology, VU University Medical Center, Amsterdam, The Netherlands

⁵Department of Physiology, VU University Medical Center, Amsterdam, The Netherlands

⁶Department of Cardiology, VU University Medical Center, Amsterdam, The Netherlands

⁷Acoustical Wavefield Imaging, Delft University of Technology, Delft, The Netherlands

⁸Shenzhen Institutes of Advanced Technology, Shenzhen, China

⁹Physics of Fluids Group and MIRA Institute of Biomedical Technology and Technical Medicine,
University of Twente, Enschede, The Netherlands

Ultrasound in Medicine and Biology, 39(3):490-506, 2013

Abstract

In this study we investigated the effect of secondary Bjerknes forces on targeted microbubbles using high-speed optical imaging. We observed that targeted microbubbles attached to an underlying surface and subject to secondary Bjerknes forces deform in the direction of their neighboring bubble, thereby tending towards a prolate shape. The deformation induces an elastic restoring force causing the bubbles to recoil back to their equilibrium position; typically within 100 μs after low intensity ultrasound application. The temporal dynamics of the recoil was modeled as a simple mass-spring system, from which a value for the effective spring constant k of the order 10^{-3} Nm^{-1} was obtained. Moreover, the translational dynamics of interacting targeted microbubbles was predicted by a hydrodynamic point particle model, including a value of the spring stiffness k of the very same order as derived experimentally from the recoiling curves. For higher acoustic pressures, secondary Bjerknes forces rupture the molecular adhesion of the bubbles to the surface. We used this mutual attraction to quantify the binding force between a single biotinylated microbubble and an avidin-coated surface, which was found to be between 0.9 - 2 nN. The observation of patches of lipids left at the initial binding site suggests that lipid anchors are pulled out of the microbubble shell, rather than biotin molecules unbinding from avidin. Understanding the effect of ultrasound application on targeted microbubbles is crucial for further advances in the realm of molecular imaging.

3.1 Introduction

Microbubbles are the most popular ultrasound contrast agent (UCA) used clinically for diagnostic ultrasound imaging. UCA microbubbles are typically $1 - 10 \mu\text{m}$ in size and consist of a gas core stabilized by a lipid, protein or polymer shell which prevents coalescence with other bubbles and reduces dissolution. The microbubbles are contained in the circulatory system following intravenous administration until they are cleared by the reticuloendothelial system (RES) [10]. Due to the compressibility of the gas core inside, the microbubbles undergo volumetric oscillations during ultrasound application giving them superior echogenicity compared to the surrounding tissue and fluid. The higher echogenicity results in a better contrast to tissue ratio (CTR) and is used in contrast enhanced ultrasound (CEUS) imaging for enhanced tissue delineation, for perfusion studies or for left ventricle opacification [22]. Moreover, microbubbles have been shown to behave as non-linear ultrasound scatterers, causing their backscattered echo to contain higher harmonics ([76],[77]) or even subharmonics [78, 79] of the driving frequency. The non-linear characteristics of microbubbles are exploited in various imaging modalities e.g. amplitude modulation [13] and pulse inversion [80] to improve the CTR.

In the mid 90's, fabrication of the first so-called targeted microbubbles was reported, where ligands to specific molecular markers were added to the shell [15, 16]. Ligands can be selected to make targeted microbubbles adhere to regions of the vascular endothelium expressing specific proteins, for instance inflammatory markers. Imaging methods involving high power destructive pulses can be used to discriminate between echoes originating from targeted and freely circulating bubbles [81]. More recently, it was shown that targeted microbubbles exhibit a pronounced shift (i.e. a 50 % decrease) in their frequency of maximum response compared to free bubbles [47]. Although these experiments were performed in well-controlled model systems, their outcome suggests that acoustical discrimination between targeted and freely flowing bubbles is feasible.

The selective imaging of targeted microbubbles in combination with their capability to recognize molecular events, facilitates targeted contrast enhancement during ultrasound application, also called molecular ultrasound [17]. Molecular ultrasound has great potential to diagnose diseases in an earlier stage, e.g. in asymptomatic patients, and to assess treatment efficacy of drugs even before morphological changes occur [82]. Recently, a new milestone was achieved when the first study of targeted microbubble imaging in humans was reported [18]. The Vascular Endothelial Growth Factor Receptor 2 (VEGF-R2) targeted microbubble BR55 (Bracco Research SA, Geneva, Switzerland) was shown to bind to VEGF-R2 receptors in the prostate of patients scheduled for prostatectomy, making molecular ultrasound potentially the first diagnostic imaging technique for prostate cancer detection and localization in the near future.

For molecular ultrasound to evolve to a robust diagnostic tool, more fundamental knowledge about the effects of ultrasound application on the behaviour of targeted microbubbles is needed. This is emphasized by the observations of Schmidt et al. (2008), who observed detachment and clustering of biotinylated microbubbles targeted to a NeutrAvidinTM coated surface during low intensity ultrasound application. Microbubble detachment reduces the amount of targeted microbubbles at the site of interest, decreasing the echo intensity and therefore complicating the interpretation of the signal. Clustering of microbubbles may change the echogenicity [83, 84]. A correct interpretation of the molecular ultrasound signal therefore demands a thorough understanding of the interaction between ultrasound and targeted microbubbles.

The effects observed by [85] were ascribed to a mutual interaction between the oscillating microbubbles known as secondary acoustic radiation force or secondary Bjerknes force¹. More recently, it was observed that targeted microbubbles, which

¹Because the direction of the pressure gradient (∇P) associated with a sound field emitted by a neighboring bubble oscillates in time, the secondary acoustic radiation force exerted on a bubble has alternating direction in time. However, as the volume (V) of the bubble also oscillates in time, the average of the instantaneous force over one period results in a net force exerted on a bubble, whose direction depends on the phase difference between the bubble oscillations and the oscillating pressure gradient [86]. This averaged net force is called secondary Bjerknes force [26].

had moved several hundreds of nanometer under the influence of attractive secondary Bjerknes forces, had moved back to their initial position by the start of a next experiment 80 ms after the ultrasound was turned off [87]. However, microbubbles that were in contact with (but not adherent to) the surface, were reported to equilibrate at a new position, closer to each other. It was therefore hypothesized that the presence of an elastic restoring force brings the targeted microbubbles back to their equilibrium position after the ultrasound is turned off. The physical mechanism of this restoring force remained elusive: the extension associated with the stretching of molecular bonds is a few orders of magnitude smaller than the observed bubble translations. Moreover, bubbles remained spherical throughout the experiments. However, the authors did not totally rule out that bubble deformation might be involved as the induced deformation could have been below the optical resolution in top view. Furthermore, the formation of elastic wrinkles and folds of excess lipid material [41], similar to what has been observed in neutrophil rolling in shear flow [88], was proposed as a second possible mechanism of the restoring force.

In this study we therefore investigated the phenomena associated with the translational dynamics of mutually interacting targeted microbubbles in more detail. We first repeated the experiments as performed by Garbin et al. (2011) for the different microbubbles and experimental configuration used in this study. Next, we investigated the time scale of the microbubble recoil after the ultrasound was turned off. To elucidate the mechanism of the elastic restoring force, simultaneous top and side view high-speed imaging [89] of interacting targeted microbubbles was performed. The paper concludes with a comparison between the experimental observations and theoretical predictions of the translational dynamics of interacting targeted bubbles using a simplified hydrodynamic model and shows that rupturing the adhesion of targeted microbubbles using secondary Bjerknes forces has potential to quantify the binding force of targeted microbubbles.

3.2 Theoretical framework and numerical modeling

Force balance during US application

We model the bubble translational dynamics during US application using a hydrodynamic model for two mutually interacting targeted microbubbles, pulsating in an ultrasound field [87]. We briefly review the model here. The model is based on the equations of motion for mutually interacting bubbles in an unbounded fluid, which were shown to be in good agreement with experimental observations [90]. Because the targeted bubbles are in contact with a wall, the pressure gradient experienced by a bubble (due to a pulsating neighboring bubble) is increased, due to reflections from the wall. To account for this effect, the so-called 'method of images' was applied in which the rigid wall is replaced by two so called "mirror bubbles", having the same size and oscillating with the same amplitude and phase as the original bubbles. This effectively results in an increase of the pressure gradient ∇P experienced by a bubble by a factor that equals the reflection coefficient of the material [91]. The corresponding force balance, including all relevant forces, is reviewed below (see also Table 1 for a definition of the symbols used).

Forces	
\vec{F}_R	Secondary acoustic radiation force
\vec{F}_{AM}	Added mass force
\vec{F}_{QS}	Quasi-steady viscous drag force
\vec{F}_H	History force
\vec{F}_K	Restoring force

Table 1: Notation force balance equation 1

The total force balance along the line of centers (here defined as the x -axis) for a pulsating targeted bubble i , interacting with a neighboring bubble j , is given by:

$$\vec{F}_R + \vec{F}_{AM} + \vec{F}_{QS} + \vec{F}_H + \vec{F}_K = 0 \quad (3.1)$$

\vec{F}_R is the secondary acoustic radiation force, which is driving the motion of bubble i . It arises due to the sound emitted by the neighboring microbubble j , when both bubbles are pulsating in an incident sound field (i.e. the primary field). The instantaneous secondary acoustic radiation force acting on a microbubble can be calculated by using the general expression for radiation forces experienced by a body [86]:

$$F = -V\nabla P \quad (3.2)$$

with V the volume and ∇P the pressure gradient over the body.

By substituting V with the expression for the volume of bubble i , and ∇P with the pressure gradient generated by the pulsating neighboring microbubble j , with radius R_j , an expression for the instantaneous secondary acoustic radiation force on a targeted bubble i , with radius R_i can be derived

$$\vec{F}_R = -(1 + \beta)\rho_L \frac{4}{3}\pi R_i^3 \frac{\ddot{R}_j R_j^2 + 2R_j \dot{R}_j^2}{d^2} \quad (3.3)$$

with ρ_L the liquid density, d the distance in between the two bubbles, R_i the radius of bubble i , R_j the radius of bubble j , \dot{R}_j its first and \ddot{R}_j its second time derivative. β is the reflection coefficient of the wall and accounts for the increase of the pressure gradient experienced by the bubble due to wall reflections.

\vec{F}_{AM} is the added mass force, which is due to the inertia of the liquid set into motion by an accelerating body. In the case of a bubble, the added mass force is much larger than the inertia of the gas/vapour core of the bubble itself. For a bubble with time-dependent radius, the added-mass force is given by [92]:

$$\vec{F}_{AM} = -\frac{1}{2}\rho_L (V_i \frac{\partial \vec{U}_i}{\partial t} + \vec{U}_i \frac{\partial V_i}{\partial t}) \quad (3.4)$$

with V_i the volume of bubble i and $\vec{U}_i = \vec{x}_i - \vec{u}$ the velocity of the bubble relative to the fluid velocity \vec{u} .

\vec{F}_{QS} is the quasi-steady viscous drag force. Because the coating of the microbubble enforces a no-slip boundary condition at the surface, the bubble experiences an increased drag compared to an uncoated bubble as a result of the generation of vorticity at the surface of the bubble. The quasi-steady drag is given, for small Reynolds numbers, by the Stokes drag [93]:

$$\vec{F}_{QS} = -6\pi\mu R_i \vec{U}_i \quad (3.5)$$

with μ the dynamic fluid viscosity.

Moreover, because the motion of a bubble moving under the influence of acoustic radiation force includes a high frequency component, the viscous drag experienced by the bubbles has an unsteady component in addition to the quasi-steady component [90]. The effect of the unsteady (high frequency) oscillatory translational motion can be understood by realizing that, for sufficiently high frequency of the oscillation, the bubble is continuously affected by the vorticity generated before by its own motion. This results in an increased drag experienced by that bubble. This effect is accounted for by the history force (\vec{F}_H), which for a no-slip bubble with time-dependent radius is given by [94]:

$$\vec{F}_H = -6\pi\rho_L \sqrt{\frac{\nu}{\pi}} \int_0^t \frac{d\tau}{\sqrt{\int_\tau^t R_i(s)^{-2} ds}} \frac{d(R_i \vec{U}_i)}{dt} \quad (3.6)$$

with ν the kinematic viscosity of the fluid.

Finally, to account for the observed recoil of targeted microbubbles after ultrasound insonification, we include a Hookean restoring force:

$$\vec{F}_K = -k\vec{x}_i \quad (3.7)$$

with k the effective spring stiffness of the targeted bubble and x_i the bubbles displacement from its equilibrium position. The theoretical justification for this linear relationship between \vec{F}_K and \vec{x}_i will be given in the Appendix.

When the bubble is bound to the functionalized surface, the sum of all the hydrodynamic forces acting on the bubble (defined as \vec{F}_{Pull}) should be opposed by the restoring force \vec{F}_K :

$$\vec{F}_R + \vec{F}_{AM} + \vec{F}_{QS} + \vec{F}_H = \vec{F}_{Pull} = -\vec{F}_K \quad (3.8)$$

Formulating equation 3.1 for both bubbles gives two coupled second order differential equations which were solved numerically to obtain the position of both bubbles x_i and x_j and the center-to-center distance d . The experimental radius-time curves ($R_i(t)$ and $R_j(t)$), their first derivatives ($\dot{R}_i(t)$ and $\dot{R}_j(t)$) and second derivatives ($\ddot{R}_i(t)$ and $\ddot{R}_j(t)$) were used as input parameters for the force balance².

Force balance after US application

After the ultrasound is turned off, both the radial bubble oscillations and the oscillatory translations cease and the secondary acoustic radiation force (\vec{F}_R) and history force (\vec{F}_H) are set to zero in the force balance of equation (3.1). Moreover, because the bubbles stop oscillating, the added mass force of equation (3.4) reduces to:

$$\vec{F}_{AM} = -\frac{1}{2}\rho_L V_i \frac{\partial \vec{U}_i}{\partial t} \quad (3.9)$$

The resulting force balance for each bubble after US application (i.e. the recoil measurements) is therefore given by:

²Buoyancy is not taken into account in the analysis as it acts in a direction orthogonal to the line of centers. Moreover, the mean terminal velocity of a buoyant bubble is a few orders of magnitude smaller than the motion driven by secondary acoustic radiation force and therefore not relevant for the phenomena investigated in this study.

$$\vec{F}_{AM} + \vec{F}_{QS} + \vec{F}_K = 0 \quad (3.10)$$

The two resulting (now uncoupled) second order differential equations were again solved numerically to obtain x_i , x_j and the distance between the bubbles $d = |x_i - x_j|$.

Theoretical predictions during and after US application

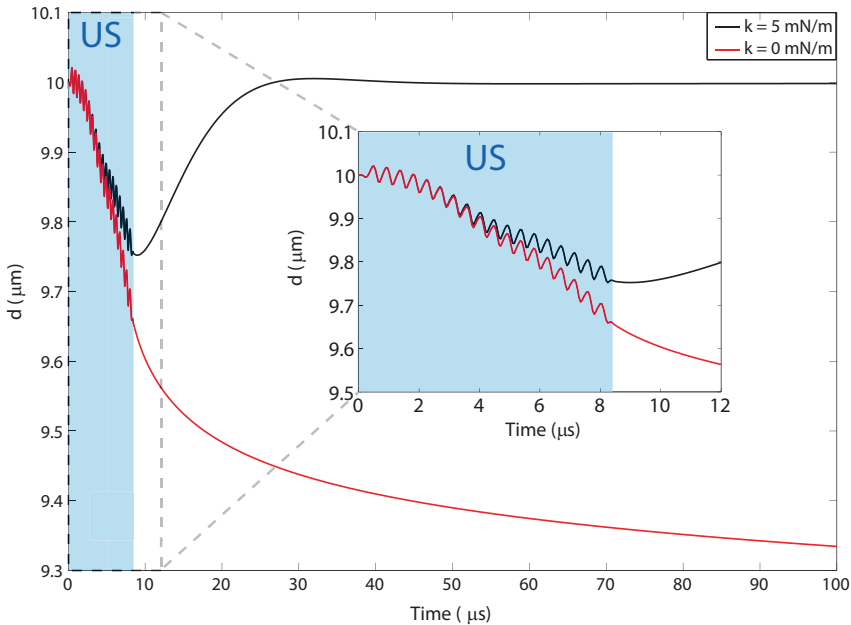


FIGURE 3.1: Simulated distance between two microbubbles during and after insonification with an ultrasound wave of 20 cycles at a frequency of 2.25 MHz ($P_- = 75$ kPa). The time span of ultrasound application is indicated by the marked area. The black curve corresponds to targeted microbubbles (both with an effective spring constant k of 5 mN/m). The red curve corresponds to two bubbles in contact with (but not adherent to) a rigid wall (i.e. $k = 0$ mN/m). The inset shows a close-up of the first 12 μ s. In contrast to the non-targeted bubbles, the start of recoil is already visible for the targeted bubble pair. The resting radius of both bubbles was 2 μ m.

To obtain an estimate of the timescale of the recoil after US application, we solved the equation of motion (equation (3.1)) with the radial dynamics predicted by the Marmottant model [95] as an input. The value for the shell viscosity (κ_s) was

set to 5×10^{-8} kg/s, the value for the shell elasticity (χ) at 1 N/m and the initial surface tension ($\sigma(R_0)$) at 63 mN/m. All bubbles had a resting radius (R_0) of 2 μm . The theoretically predicted evolution of the separation distance between two bubbles (initially 10 μm apart) in response to 20 cycles at a frequency of 2.25 MHz at $P_- = 75$ kPa is shown in Figure 3.1. When the effective spring constant k is set to 0 (red curve), the bubbles approach each other during US application but no recoil afterwards can be observed. This situation represents the dynamics of two interacting non-targeted microbubbles. When a restoring term is included in the equation of motion (black curve, $k=5$ mN/m), the bubbles approach each other during US application (although significantly less than in the non-targeted case), but the separation distance is restored to the initial value of 10 μm within 20 μs after the ultrasound is turned off. The inset shows a close-up of the dynamics during the first 12 μs , including a few μs after US application. The start of the recoil is already visible for the targeted case (black curve). From these simulations we can conclude that the recoil after US application is likely to cover several tens of μs , dependent on the stiffness of the effective spring constant k . To capture the recoil, we therefore imaged the interacting bubbles at relatively low frame rates (~ 1 million frames per second (Mfps)). In this way, we covered a time window lasting over 100 μs . Experimentally it was observed that a higher pressure was needed to translate the bubbles. Both the vicinity of a wall and neighboring bubbles are known to suppress the oscillation amplitude [96], which will also influence the observed translation of the bubbles. This motivated us to use the experimentally obtained radius-time curves (and its derivatives) as input parameters for the hydrodynamic model in order to compare simulations and experiment.

3.3 Materials and Methods

Preparation of microbubbles

Biotinylated microbubbles with a perfluorobutane (C_4F_{10}) gas core were made by sonication [57]. The mean diameter of the microbubble distribution was 3.5 - 4 μm . The coating was composed of 1,2-distearoyol-*sn*-glycero-3-phosphocholine (DSPC, 59.4 mol % ; P 6517; Sigma-Aldrich, Zwijndrecht, the Netherlands), polyoxyethylene-40 stearate (PEG-40 stearate, 35.7 mol %; P 3440; Sigma-Aldrich), 1,2-distearoyol-*sn*-glycero-3-phosphoethanolamine-N-[methoxy(polyethylene glycol) 2000] (DSPE-PEG(2000), 4.1 mol %; 880125 P; Avanti Polar Lipids, Alabaster, AL, USA) and DSPE-PEG(2000)-biotin (0.8 mol %; 880129 C; Avanti Polar Lipids). For fluorescence microscopy, a very small amount of the lipophilic dye octadecyl-indocarbocyanine (DiI, Molecular Probes, Eugene, OR, USA) was dissolved in ethanol and added to the solution just before sonication.

OptiCell coating

For top view experiments, the topside of an OptiCell (Thermo Fisher Scientific, Waltham, MA, USA), consisting of two 75 μm thick polystyrene membranes separated by 2 mm, served as target surface and was coated with NeutrAvidinTM (Invitrogen). A 100 μL droplet of 1 $\mu\text{g}/\text{mL}$ solution of NeutrAvidinTM in PBS (Invitrogen) was deposited on an OptiCell membrane and incubated overnight at room temperature in a humidity chamber. As a negative control a 100 μL droplet of PBS was used. After 24 hours, the surface was rinsed with PBS to remove all the unbound protein and incubated for 1h with 1% Bovine Serum Albumin (BSA, Sigma-Aldrich) to prevent unspecific binding. Afterwards, the surface was rinsed again with PBS and mounted with the coated side down in a tank filled with PBS. Biotinylated microbubbles were injected in the tank and allowed to interact with the coated surface by flotation for 10 minutes. After that, the surface was again rinsed with PBS to remove all unbounded microbubbles and the bottom

(non-coated) membrane was cut from the OptiCell. Following these preparation steps, the OptiCell with the targeted bubbles was mounted on top of a tank filled with gas-saturated water with the targeted microbubbles on top. The targeted microbubbles, separated by the thin remaining polystyrene surface of the OptiCell from the water below, were submersed in PBS.

Capillary coating

For simultaneous top and side view imaging of targeted microbubbles, a polystyrene capillary (Paradigm Optics Inc., Vancouver, WA, USA), with inner and outer diameters of 15 μm and 80 μm respectively, was used as target surface. The capillary was submersed in a 1 $\mu\text{g}/\text{ml}$ solution of NeutrAvidinTM and incubated overnight at room temperature. The surface was then rinsed with PBS and incubated for 1h with 1% Bovine Serum Albumin (BSA). After rinsing with PBS, the capillary was mounted in a tank. The tank was filled with PBS and the bubbles were injected. Next, the fluid level was decreased so that the bubbles were in contact with the top side of the capillary. After 10 minutes, the fluid level was again increased and the chamber was rinsed several times with PBS to remove unbound bubbles from the solution.

Experimental setup

Figure 3.2 shows a schematic representation of the experimental setups used for top view and orthogonal view (i.e. simultaneous top and side view) high-speed imaging. For top view imaging, the OptiCell was mounted on a water tank that also held an illumination fiber and a 2.25 MHz single element PZT transducer (Panametrics Inc., Waltham, MA, USA) with a focal distance of 75 mm. A semi-transparent mirror (STM) was used to split the transmitted light into a part towards the Brandaris 128 camera [97] and a part to a high sensitivity video camera (Watec LCL 902K, Watec Inc., Middletown, NY, USA). Microbubbles were

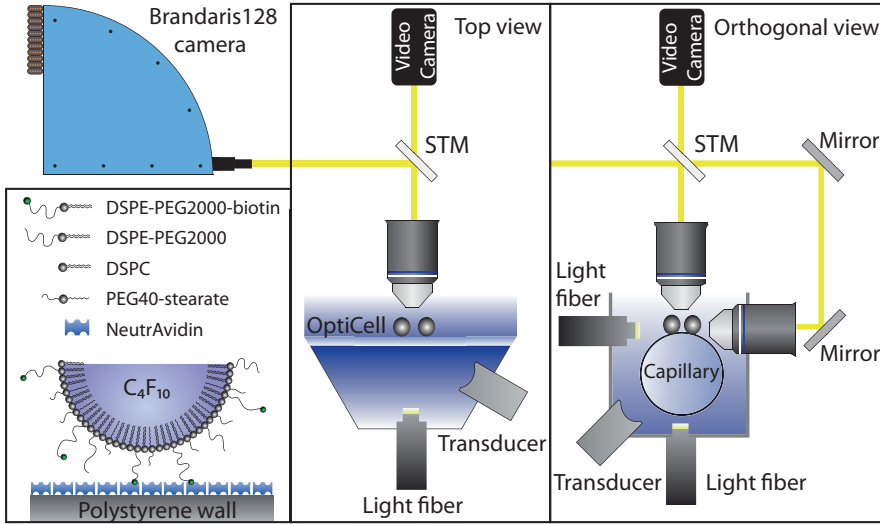


FIGURE 3.2: Schematic drawing of the experimental setup used for top view and orthogonal view high-speed imaging. In the orthogonal configuration, the optical pathways of top and side view are merged after passing the semi-transparent mirror (STM). The bottom left panel shows a schematic representation of the bubble shell and the target surface.

imaged with a customized BXFM microscope (Olympus Nederland B.V., Zoeterwoude, The Netherlands) equipped with a $2\times$ magnification ring in combination with a $60\times$ water-immersion objective lens (LUMPLFL, NA=0.9, Olympus) or a $100\times$ water-immersion objective lens (LUMPLFL, NA=1.0, Olympus). Fluorescence (DiI) was visualized using a fluorescence illuminator, containing a 100 W mercury lamp (U-LH100HG) in combination with a fluorescence cube (U-MWG2, excitation 510-550 nm, emission 590 nm, dichroic filter 570 nm, Olympus). Fluorescence images were captured before and after ultrasound application.

The setup used for orthogonal imaging allows for the placement of an additional objective lens orthogonal to the top view lens [89]. Due to the restrictions in space when using two objective lenses positioned orthogonally, the imaging was performed with two $40\times$ water-immersion objective lenses (LUMPLFL, NA=0.8, Olympus). Collimated light beams from the side view objective were redirected by two mirrors and merged with the beams originating from the top view objective using a semi-transparent mirror (STM). Part of the combined image was directed

to the Brandaris 128 camera and part was directed to the high sensitivity CCD camera. The water tank was holding two light fibres and a focused PVDF transducer (PA076, Precision Acoustics, Dorchester, UK) with a focal distance of 25 mm.

Microbubbles were insonified at varying pressures ($P_{-}=0-330$ kPa) with 20-30 cycles with a Gaussian tapered window at a frequency of 2.25 MHz, generated by an arbitrary waveform generator (Tabor Electronics Ltd., Model 8026, Tel Hanan, Israel) and amplified by a 60 dB RF linear amplifier (ENI, Model A-500, Rochester, NY, USA). The optical and acoustical focus were aligned prior to each experiment. The transducers were calibrated using a 0.2 mm PVDF probe hydrophone (Precision Acoustics) in combination with a motorized xyz-stage controlled by Matlab[®] (The Mathworks, Natick, MA, USA). The bottom left panel of Figure 3.2 shows the position of the targeted bubbles with respect to the functionalized substrate. In both the top view and the orthogonal view experiments, targeted microbubbles were positioned on top of the polystyrene membrane. In this configuration, microbubbles that were not bound to the surface would float out of the optical focus due to buoyancy.

High-speed imaging protocol

For high-speed imaging purposes, images were relayed to the ultrafast-framing Brandaris 128 camera. Because of the differences in time scale of the dynamics during and after ultrasound application (see Figure 3.1), different imaging protocols were used to capture the translation dynamics during and after US application. To capture the translational dynamics after US insonification, frame rates near 1 Mfps were used. This resulted in a time window of the order of 100 μ s for each individual movie consisting of 128 frames, sufficient to capture the entire recoiling phase. The first 10 μ s of these movies captured the oscillatory attraction (but undersampled) and the remaining part captured the recoil of the microbubbles. In order to study the translation dynamics during US application higher frame

rates were used (typically around 11 Mfps), resulting in this case in a time window of about 12 μ s for each individual movie of 128 frames. The time between consecutive movies was 80 ms. The movies were transferred to a computer and analyzed offline.

Data analysis

The radius and center of mass of the microbubbles in each frame was determined by using semi-automatic custom software written in Matlab[®][98]. The determination of the absolute position of the bubbles is affected by microscopic misalignments of the individual sensors of the Brandaris 128 camera with respect to the optical axis. We compensated for this effect using calibration grids. After compensation, the maximum variation in the absolute bubble position was typically between 80-130 nm. The center-center distance is not affected by this effect and was therefore considered to be the most reliable measure of displacement. The maximum variation in the center-to-center distance observed before ultrasound application was typically 60-90 nm. For the radius of the bubbles, this variation was typically 30-50 nm. The radius-time curves and the distance-time curves obtained experimentally were resampled using a cubic interpolation. The semi-automatic contour-tracking software failed to track the contour of the bubbles in side view due to the lack of contrast close to the capillary. We therefore tracked the contour of the bubbles in these images manually (both in top and side view). The semi-major (a) and semi-minor (b) axes were determined using the Matlab-routine "regionprops".

3.4 Results

Translational dynamics during ultrasound application

Targeted microbubbles of similar size were observed to be mutually attracted towards each other during ultrasound application. Figure 3.3 shows the evolution

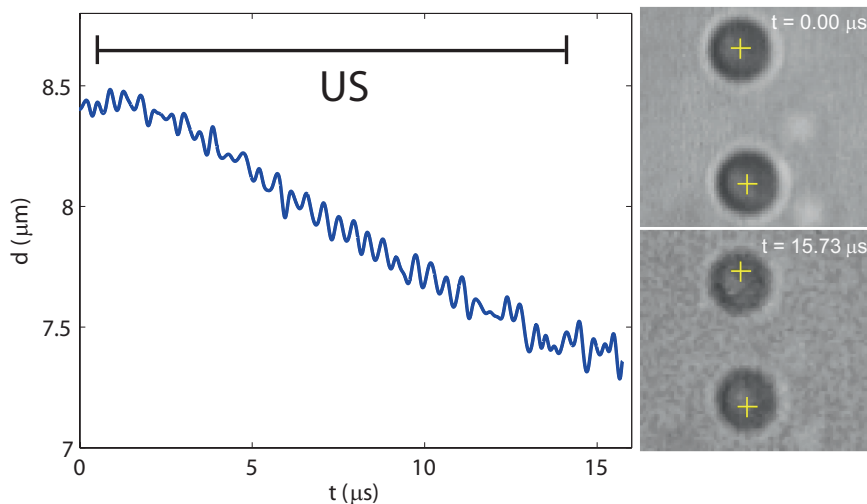


FIGURE 3.3: The distance between two targeted microbubbles during insonification with 30 cycles at a frequency of 2.25 MHz ($P_- = 250$ kPa). The black bar corresponds to the time window of ultrasound application. The ring-down of the transducer and transient behavior of the microbubbles causes the oscillations to continue for a few more cycles after the driving pulse ends. The two snapshots on the right correspond to the configuration before ($t=0 \mu\text{s}$) and right after application of ultrasound ($t=15.73 \mu\text{s}$). The yellow crosshairs indicate the position of the centers of mass of the bubbles at $t=0 \mu\text{s}$. The resting radius of both bubbles was $2 \mu\text{m}$. See also video 1 online (Supplemental Materials: <http://dx.doi.org/10.1016/j.ultrasmedbio.2012.09.025>)

of the center-to-center distance between two targeted bubbles insonified with 30 cycles at a frequency of 2.25 MHz and $P_- = 250$ kPa. The typical high frequency oscillation (at the applied ultrasound frequency) due to the alternating attractive and repulsive character of the secondary acoustic radiation force superimposed to a slow drift towards each other can be observed.

Although the center-to-center distance decreased by $1 \mu\text{m}$ during US application, no apparent bubble deformation was visible in top view. The two snapshots on the right side of Figure 3.3 correspond to the configuration before ($t=0 \mu\text{s}$) and right after ultrasound application ($t=15.73 \mu\text{s}$). The yellow crosshairs correspond to the positions of the centers of the bubbles at $t=0 \mu\text{s}$, just before ultrasound application. Right after ultrasound application, the center of each bubble is shifted along the line of centers in the direction of the other bubble.

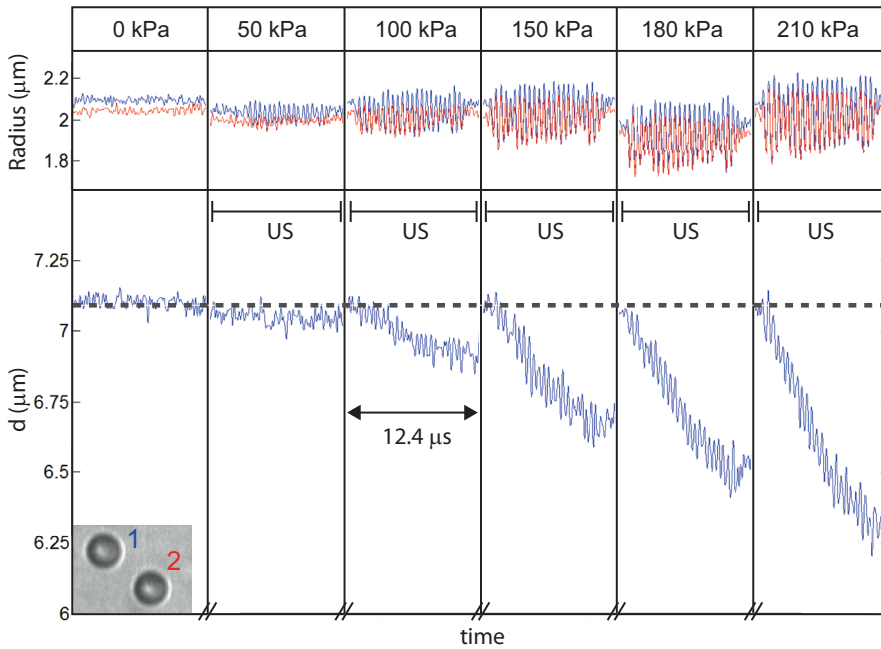


FIGURE 3.4: Top panel: Radius-time curve of the two bubbles shown in the inset, blue for bubble 1, red for bubble 2, during 6 successive experiments (20 cycles at a frequency of 2.25 MHz, $P_{-} = 0 - 210$ kPa). No ultrasound was applied in the first experiment. Bottom panel: Center-to-center distance during the 6 successive experiments. The time span of one individual experiment was 12.4 μs . The vertical lines indicate the time gap of 80 ms between the successive experiments. The black bars correspond to the time windows of US application. The resting radius of both bubbles was approximately 2 μm (see also the R-t curves in the top panel).

At relatively low acoustic pressures, targeted microbubbles exhibit spring-like behaviour. Microbubbles moved towards each other during ultrasound application but recoiled back to their initial position afterwards. Figure 3.4 shows six successive experiments in which two targeted microbubbles (see inset) were insonified with 20 cycles at a frequency of 2.25 MHz at various acoustic pressures up to $P_{-}=210$ kPa. For each individual experiment, with a time span of 12.4 μs , the top panel shows the radial excursions of the two microbubbles (blue for bubble 1, red for bubble 2) and the bottom panel shows the evolution of the center-to-center distance. The vertical lines indicate the position of the time gap between consecutive experiments, which was set at 80 ms. In the first movie no ultrasound

was applied. The center-to-center distance was observed to decrease during ultrasound application as observed before due to an attractive secondary Bjerknes force. However, by the start of a successive experiment (i.e. 80 ms after the ultrasound was turned off) the distance had again recovered to the initial value of $7.1\ \mu\text{m}$, implying the presence of a restoring force, causing each bubble to move back to its original position. These jumps in the center-to-center distance between successive experiments were not observed during control experiments with biotinylated microbubbles in contact with an uncoated OptiCell membrane. In that case, the distance in between two microbubbles did not recover to the initial value after US application.

To investigate the possibility to detach the targeted microbubbles using this attractive secondary Bjerknes force, the very same bubbles were insonified at higher pressure in the range $P_{-}=0\text{-}330\ \text{kPa}$. The radius time curves (top panel) and center-center distance-time curves (bottom panel) are shown in Figure 3.5. Following insonification until a pressure of $210\ \text{kPa}$ (i.e. distance decrease of $700\ \text{nm}$), the bubbles were still observed to move back to their initial position afterwards. However, after insonifying the microbubbles with $270\ \text{kPa}$ (i.e. distance decrease of $1.3\ \mu\text{m}$), the distance restored only partially to the new value of $6.5\ \mu\text{m}$, suggesting the adhesion of at least one bubble to the substrate was broken. At the end of the fifth experiment ($P_{-}=330\ \text{kPa}$) the microbubbles were in contact with each other and the center-to-center distance had reduced to a value equal to the sum of both radii. Remarkably, bubble 2 exhibited a sudden decrease in pulsation amplitude during the $270\ \text{kPa}$ experiment. This phenomenon was observed before with two interacting bubbles positioned away from a wall [96] and is expected to result from complex bubble-bubble interactions in close proximity. The initial and final positions of the two bubbles are shown in the left and right inset, respectively. After the experiment, both bubbles were observed to be smaller in size. The loss of shell material as a result of lipid pullout due to microbubble detachment (which will be discussed later) might have accelerated the shrinkage of the bubbles due to the increased Laplace pressure.

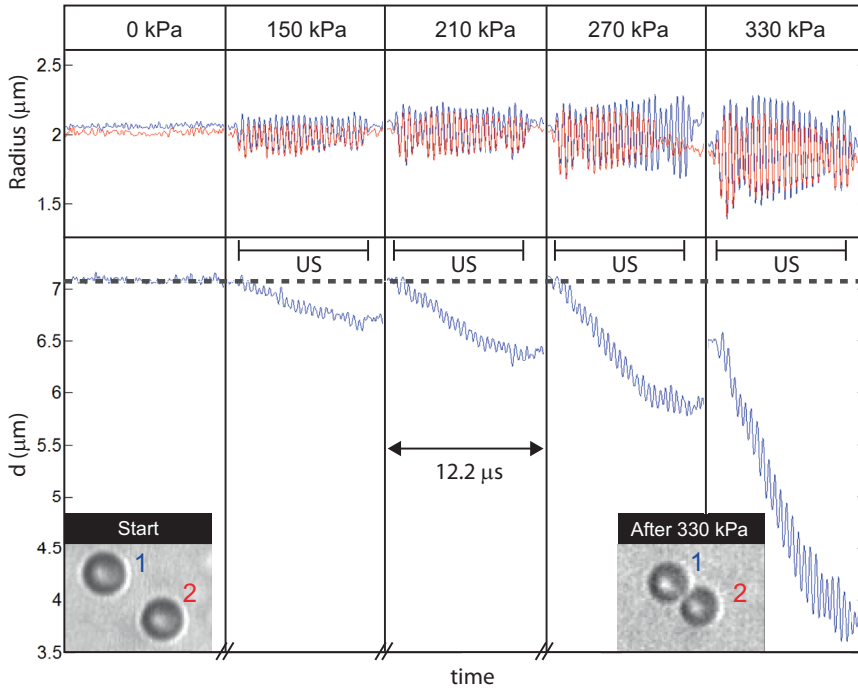


FIGURE 3.5: Microbubbles of Figure 3.4 insonified in a second experiment at higher pressures up to $P_{-}=330$ kPa. Top panel: Radius time curve (blue for bubble 1, red for bubble 2) during successive experiments. Bottom panel: Evolution of the center-to-center distance during the 5 experiments. The time span of one individual experiment was $12.2 \mu\text{s}$. The left and right insets represent the initial and final bubble positions, respectively.

Translational dynamics after ultrasound application

Between successive insonifications at relatively low pressures (see Figure 3.4) it was observed that microbubbles had moved back to their initial position. To capture the entire translation after ultrasound application (i.e. when radial pulsations had ceased), microbubbles were insonified with 20 cycles at 2.25 MHz and imaged at a relatively low frame rate (1.15 Mfps). The results of six successive experiments at various acoustic pressures are shown in Figure 3.6. Each individual experiment covered a time window of $110 \mu\text{s}$. Microbubbles were insonified during the first part of each movie with 20 cycles at a frequency of 2.25 MHz, indicated by the blue transparent windows in Figure 3.6. The remaining part of the movies

captured the relaxation of the microbubbles afterwards. As observed before, the center-to-center distance decreased during ultrasound application, clearly visible for the 180 kPa, 240 kPa and 300 kPa experiments shown in Figure 3.6. At the moment the ultrasound was turned off, the distance reached a minimum value (10.3 μm , 10.1 μm and 9.2 μm for the 180 kPa, 240 kPa and 300 kPa experiment respectively). After insonification with 180 kPa and 240 kPa, the distance was observed to recover to the initial value of 10.8 μm within 100 μs . A small overshoot during the last part of the 240 kPa movie was also observed. Insonification with a pressure of 300 kPa, resulted in only a partial recovery of the center-to-center distance and equilibrated around a new value of 10.2 μm instead. Again, no bubble deformation could be observed in top view. A closer inspection revealed that only bubble 1 had detached from its initial binding position after insonification with 300 kPa; bubble 2 on the other hand had moved back to its initial position. The 1.6 μm decrease in center-to-center distance during insonification with 300 kPa is therefore the sum of a reversible component and irreversible component (see arrows in Figure 3.6). The irreversible component (0.6 μm) is due to unbinding of bubble 1 from the functionalized substrate. The reversible component (1 μm) is equal to the sum of the backward translation of both bubbles afterwards (i.e. bubble 1 was not completely detached), driven by the restoring force \vec{F}_K .

Mechanism of the restoring force

To elucidate the mechanism of the restoring force causing the targeted microbubbles to recoil to their initial position after the ultrasound is turned off, the dynamics of the bubbles were imaged simultaneously in top and side view. The bubbles were positioned on top of a polystyrene capillary coated with NeutrAvidin and were insonified with 20 cycles at a frequency of 2.25 MHz. The results are shown in Figure 3.7. Panel A shows the effect of the attractive secondary Bjerknes force on the position of two neighboring bubbles seen in top view. The resting radii of bubble 1 and 2 was 2.5 μm and 2.2 μm respectively. The initial position of bubble 1 was set to the initial separation distance of 7.6 μm ; the initial position of bubble 2 was

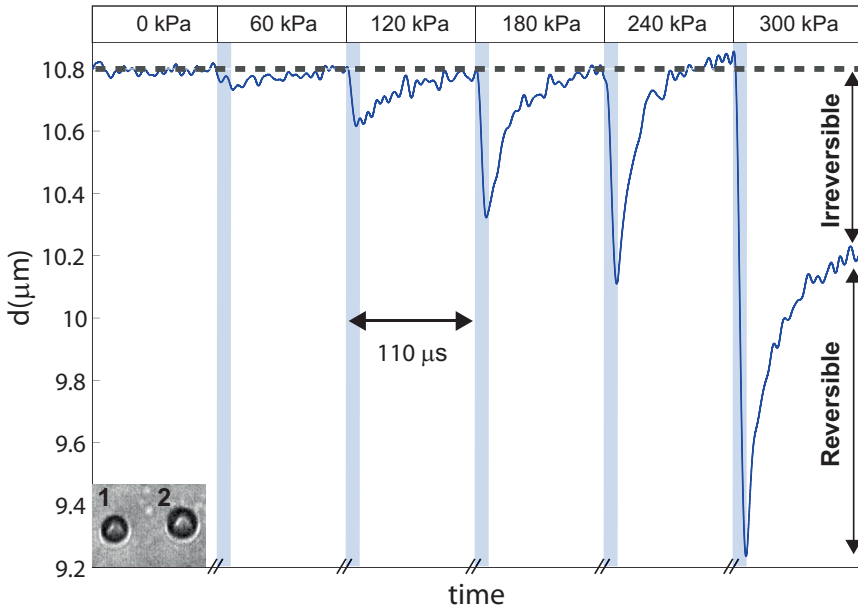


FIGURE 3.6: Distance between two targeted microbubbles (displayed in the inset) versus time during and after ultrasound insonification. The pressure was increased in subsequent experiments ($P_{-} = 0 - 300$ kPa). The time gap between the experiments was 80 ms. Bubbles were insonified at the start of each experiment with 20 cycles at a frequency of 2.25 MHz (indicated by the light blue blocks), lasting for about $9 \mu\text{s}$. The total time covered by each movie was $110 \mu\text{s}$. The resting radii of bubble 1 and bubble 2 were $2.2 \mu\text{m}$ and $2.4 \mu\text{m}$, respectively.

set to $0 \mu\text{m}$. Attractive secondary Bjerknes forces cause both bubbles to move by about 600 nm along the line of centers towards the other bubble. No apparent deformation was visible in top view, confirming earlier observations. However, side view imaging revealed that a microbubble elongates in the direction of the other bubble, thereby tending towards a prolate shape. This effect is illustrated for the in-focus bubble 2 in panel B³. The aspect ratio of the bubble in top view (red dots) is approximately constant and near unity throughout the experiment. However, the aspect ratio in side view (blue dots) increases by about 20%, from 1.1 before to 1.3 right after ultrasound application. Panel C and D show, respectively, the top view and side view images of the same bubbles, before (at $t = 0 \mu\text{s}$) and right after US application (at $t = 11.26 \mu\text{s}$). The deformation of bubble 2 is clearly

³Because the line of centers was not completely parallel to the object plane of the side view objective, only bubble 2 appears to be in focus in side view; bubble 1 appears to be slightly out of focus. We therefore directed further analysis on bubble 2 only.

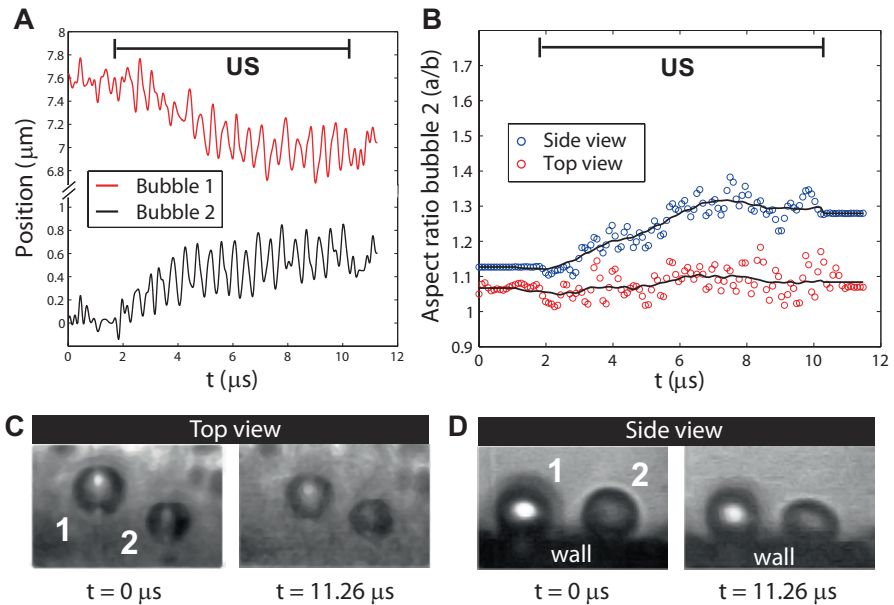


FIGURE 3.7: (A) The effect of the secondary Bjerknes force on the individual position of two neighboring targeted bubbles seen in top view. The bubbles were insonified with 20 cycles ($P_- = 153$ kPa) at a frequency of 2.25 MHz. The resting radii of bubble 1 and bubble 2 were $2.5 \mu\text{m}$ and $2.2 \mu\text{m}$, respectively. (B) The aspect ratio (a/b , with a the semi-major and b the semi-minor axis) of bubble 2 in top view (red dots) and in side view (blue dots) during the very same experiment. (C) Top view images of both bubbles before ($t = 0 \mu\text{s}$) and right after US application ($t = 11.26 \mu\text{s}$). (D) Side view images of the same bubbles before ($t = 0 \mu\text{s}$) and right after US application ($t = 11.26 \mu\text{s}$).

visible. The black area at the bottom of the side view images represents the wall of the top side of the capillary.

These results show that microbubbles subjected to an attractive secondary Bjerknes force tend to deform towards a prolate spheroid in the direction of the other bubble. This deformation induces a restoring force \vec{F}_K that opposes the net pulling force \vec{F}_{Pull} , up to a point where it overcomes the adhesion force of the microbubble to the substrate and the bubble detaches.

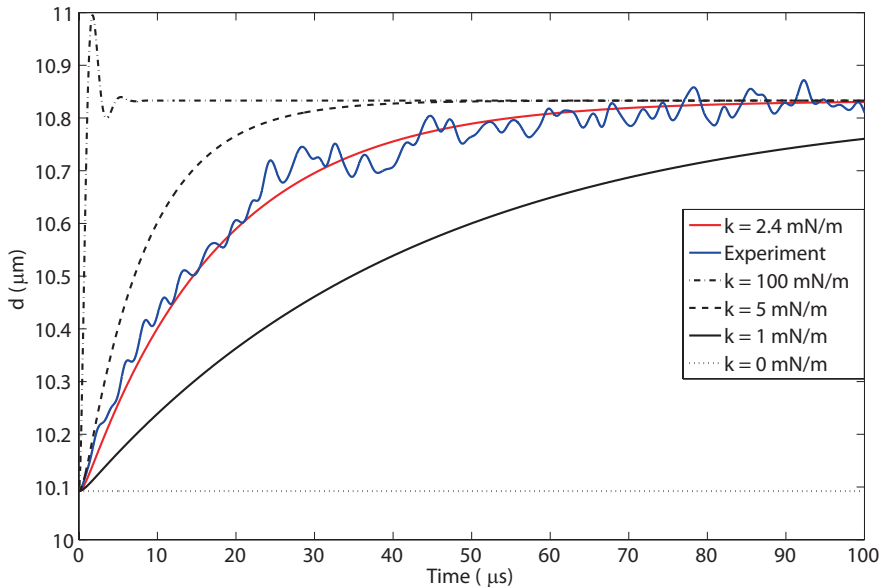


FIGURE 3.8: Center-to-center distance between two targeted microbubbles versus time after insonication with 20 cycles at a pressure of 240 kPa. Here $t=0 \mu\text{s}$ corresponds to the time the ultrasound was turned off. Shown here are the experimental data (blue curve) and simulated curves for different values of k . A value of $k=2.4 \text{ mN/m}$ (red curve) gave the best fit between theory and experiment ($r^2=0.98$). The simulated curves for $k=100 \text{ mN/m}$ (dash-dotted black line), $k=5 \text{ mN/m}$ (dashed black line), $k=1 \text{ mN/m}$ (solid black line) and $k=0 \text{ mN/m}$ (dotted black line) are also shown for comparison.

Effective spring constant k

For small displacements (typically less than $\sim 500 \text{ nm}$ for the microbubble sizes studied here ($R_0=2 - 2.5 \mu\text{m}$)), the restoring force causes the microbubbles to move back to their initial positions within $100 \mu\text{s}$ after the ultrasound is turned off. To quantify the value of the effective spring stiffness k , the theoretical prediction of the center-to-center distance obtained by solving the equation of motion after ultrasound application (see equation (3.10)) was fitted to the experimental data. The experimental result of the 240 kPa experiment of Figure 3.6 is shown again in Figure 3.8 (blue curve). Only the relaxation part is shown here and the curve starts when the center-to-center distance was at the minimum value of $10.1 \mu\text{m}$, i.e. $t=0 \mu\text{s}$ corresponds to the time the ultrasound was turned off. Using a least-squares fitting, a value of $k=2.4 \text{ mN/m}$ was obtained for the spring stiffness (red

curve, $r^2=0.98$). Theoretical predictions for $k=100$ mN/m (dash-dotted black line), $k=5$ mN/m (dashed black line), $k=1$ mN/m (solid black line) and $k=0$ mN/m (dotted black line) are also plotted. The solution for $k=100$ mN/m gives a clear overshoot and subsequent ringing, characteristic for the relaxation of an underdamped harmonic oscillator. The experimental observation clearly resembles an overdamped situation. As expected, when $k=0$ mN/m (i.e. no restoring force present), there is no recovery of the initial distance after the ultrasound is turned off.

Modeling translational dynamics during ultrasound application

Garbin et al. (2011) showed that the translational dynamics of mutually interacting microbubbles, in contact with, but not adherent to a polystyrene wall, can be predicted by a hydrodynamic point particle model. We modify the model by the addition of a restoring term \vec{F}_K and extract a value of the effective spring constant by fitting the experimental data during US application.

The results are shown in Figure 3.9. The blue curve shows the experimentally obtained distance-time curve between two targeted microbubbles during insonification with 20 cycles at 2.25 MHz and $P_- = 210$ kPa. Not including a restoring term (i.e. $k=0$) in the force balance leads to an overestimation of the decrease in the separation distance by about 600 nm (see red curve). On the other hand, including a restoring term in the force balance, with a value of k of 6 mN/m gives a good prediction of the final separation distance (see black curve). Moreover, the agreement during the high frequency oscillatory part is also very satisfactory. Furthermore, the beginning of the recoil (after ultrasound) is also predicted by the model. The value of $k = 6$ mN/m is of the same order as derived independently from the recoiling curves for a different set of bubbles, and which amounted to 2.4 mN/m, see previous section.

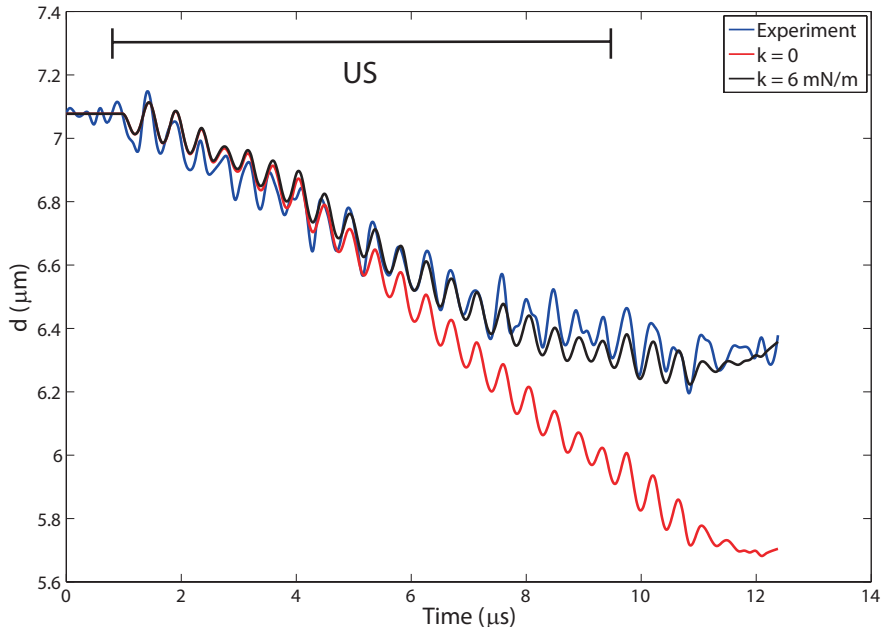


FIGURE 3.9: Blue curve: the distance in between two targeted microbubbles during insonification with 20 cycles at a frequency of 2.25 MHz and $P_- = 210$ kPa. Red curve: the predicted curve by the hydrodynamic model with $k = 0$ mN/m. Black curve: the prediction by the model with $k = 6$ mN/m. The time span of ultrasound application is indicated by the black bar.

Quantification of the microbubble binding force

In the previous sections we have shown that above a certain threshold of the displacement, microbubbles did not move back anymore to their initial position, suggesting that the bubbles had (partially) detached from their initial position at the functionalized substrate. We hypothesize that a microbubble detaches from the substrate when the restoring force \vec{F}_k , opposing the net pulling force, exceeds the cumulative force that the adhesive belt of the microbubble can resist. To estimate this force, the value of the effective spring constant (k) and the distance translated by the center of mass of the bubbles (\vec{x}) needs to be known. The value of the effective spring constant k can be deduced from the recoiling curves like the ones shown in Figure 3.6. For the bubble pair of Figure 3.6 a value for the effective spring constant k of 2.4 mN/m was obtained (see Figure 3.8). From Figure 3.6

we can also conclude that the bubbles still moved back to their initial position after a decrease in distance of $0.7\ \mu\text{m}$ (i.e. $0.35\ \mu\text{m}$ translation per bubble), due to insonification with 20 cycles at 2.25 MHz and $P_- = 240\ \text{kPa}$. However, after a decrease of $1.6\ \mu\text{m}$ (i.e. $0.80\ \mu\text{m}$ of translation per bubble) the center-to-center distance only recovered partially and was observed to equilibrate at the new value of $10.2\ \mu\text{m}$. Although both bubbles were observed to translate equally during ultrasound application, only bubble 1 (i.e. the smaller bubble) had detached from the substrate during the $P_- = 300\ \text{kPa}$ experiment. Presumably, because of its smaller contact area, the smaller bubble 1 has less molecular interactions with the target surface, making it the weakest link of this bubble pair. By multiplying the value of k with the experimentally observed translation of the bubble during the 240 kPa experiment and 300 kPa experiment we can estimate the lower and upper limit of the force the adhesive belt of the bubble can resist. For bubble 1 this threshold force was calculated to be between 0.9 nN - 2 nN. As bubble 2 still moved back to its initial position after insonification with 300 kPa, we can conclude that the threshold force to initiate detachment for this particular bubble was not exceeded at this pressure level.

3.5 Discussion

We studied the translational dynamics of mutually interacting targeted microbubbles during and after ultrasound application in detail using high-speed optical imaging. Targeted microbubbles of similar size were observed to attract each other during ultrasound application. Typically, this movement consists of a high frequency component equal to the frequency of the applied sound superimposed onto a slow drift towards each other (see Figure 3.3 and 3.9). In contrast to non-targeted microbubbles in contact with a wall, targeted microbubbles were observed to have moved back to their initial starting position by the start of a next experiment 80 ms later (see Garbin et al. (2011)). The presence of a restoring force (\vec{F}_k) was therefore already hypothesized by the previous authors. In this study we imaged the recoil of targeted microbubbles under the influence of this

restoring force after the ultrasound was turned off. Simultaneous top and side view high-speed imaging revealed that during ultrasound application, a targeted microbubble deforms in the direction of its neighboring bubble, tending towards a prolate shape (see side view image at $t = 11.26 \mu\text{s}$, Figure 3.7). The simultaneously obtained top view recordings did not, however, exhibit bubble deformation, confirming earlier observations.

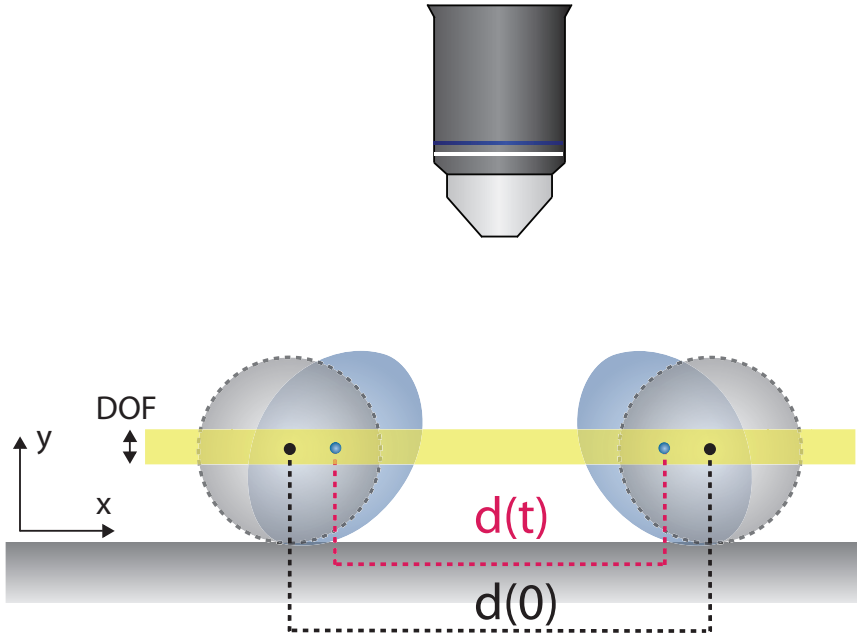


FIGURE 3.10: Artist's impression of the deformation of two targeted microbubbles during ultrasound application. The reader is looking through the side view objective. The initial position of the center of mass of both bubbles (grey circles) is indicated by the black dots. The position of the center of mass of the two deformed bubbles (blue spheroids) during ultrasound application at time point t is indicated by the blue dots. The depth of field (DOF) of the top view objective lens is indicated by the yellow bar ($\sim 800 - 1000 \text{ nm}$ for the imaging system used in this study).

The apparent contradiction between top and side view observations (deformation versus no deformation) can be explained by the orientation of the corresponding object planes of the top and side view objectives. Figure 3.10 shows an artist's impression (not to scale) of the deformation of interacting targeted microbubbles during ultrasound application. The reader is looking through the side view objective. The grey circles represent the initial configuration. When the ultrasound

is turned on, mutual attractive interactions cause the bubbles to bend over into the direction of the neighboring bubble, inducing a prolate shape deformation, represented by the blue spheroids. The deformation causes the distance between the center of mass of the two bubbles to change from $d(0)$ to $d(t)$. In side view the elongation is clearly visible because the direction of the induced deformation is parallel to the object plane of the side view objective (i.e. the x,y-plane). However, the top view objective only reveals a x,z-plane projection of the deformation induced within a thin optical slice (see yellow bar). When the deviation from sphericity of this projection is below the resolution limit of the system, the bubble will still have a spherical appearance in top view. This explains why no deformation was observed in top view, even when bubbles were observed to move several hundreds of nanometer, see video stills of Figure 3.3.

In this study, a hydrodynamic point particle model including a restoring term \vec{F}_k was used in a first attempt to capture the dynamics of interacting targeted microbubbles in response to ultrasound insonification. Although the predictive value of the model during and after ultrasound application (Figure 3.8 and 3.9) seemed to be quite satisfactory, several factors complicating the interpretation should be addressed. First, the bubbles are modeled as rigid spheres, moving parallel to the wall when subjected to secondary Bjerknes forces. Although this representation is what one may expect based on the top view observations (see Figure 3.3), in fact, bubbles are attached to the coated surface by means of a finite contact area, inducing a mechanical constraint, up to a point where the binding is ruptured. This configuration causes the bubbles to deform in the direction of the other bubble during ultrasound application, as revealed by side view imaging, instead of translating as a sphere. The effect of the deformation on the magnitude of the hydrodynamic forces acting on the bubbles is not straightforward to quantify, which motivated us to use the approximate situation of translating spheres. In addition, the hydrodynamic model does not capture dissipative effects in the viscous boundary layer near the wall. The presence of a wall is known to influence the viscous dissipation experienced by a moving object [99, 100]. Neglecting these boundary effects is based on previous results on the translational dynamics of interacting

bubbles in contact with, but not adherent to, a wall [87]. In that study, it was shown that the translational dynamics of these bubbles in response to ultrasound bursts could be predicted with good accuracy by a similar hydrodynamic model (but without the restoring term \vec{F}_k), also neglecting these boundary effects. We therefore assume that for our case, neglecting these effects in a first approximation is justified. Nevertheless, inclusion of the dissipative effects due to the presence of the wall would probably improve the accuracy of the model and is currently under investigation.

The model can be further improved by the inclusion of force-dependent binding kinetics [101]. A computational method combining large scale hydrodynamics with stochastic molecular binding kinetics, known as adhesive dynamics, was shown to successfully predict experimentally observed phenomena associated with leukocyte adhesion, including rolling, transient attachment and firm adhesion [102]. It also recreated the dynamics of leukocyte rolling over a functionalized surface under simple shear flow conditions successfully [103]. Recently, the adhesive dynamics model was applied to simulate the binding characteristics of single and dual-targeted microbubbles [53]. However, these simulations were performed for bubbles subjected to simple steady shear flow, a situation quite different from a targeted microbubble subjected to an oscillatory acoustic attraction by a pulsating neighboring bubble.

We have presented a new method to determine the microbubble binding force using the mutual attraction between similarly sized targeted microbubbles. The net attractive force imposed on the bubble due to the presence of the pulsating neighboring bubble induces a deformation of the bubble and the action of a restoring force \vec{F}_k , driving the recoil after the US is turned off. We hypothesize that the adhesion of a targeted microbubble to the functionalized substrate is ruptured when the restoring force \vec{F}_k overcomes a certain threshold, which is the cumulative adhesive strength of the molecular interactions between bubble and substrate (i.e. $\vec{F}_k > \sum \vec{F}_b$). By fitting the relaxation measurements with the hydrodynamic model after ultrasound application a value for the effective spring constant k could be obtained (see Figure 3.8). For a bubble with $R_0 = 2.1 \mu\text{m}$ (left bubble in the inset

of Figure 3.6), the binding force with the surface was calculated to be between 0.9 - 2 nN. From this binding force \vec{F}_b , an estimate of the number of molecular interactions between bubble and substrate can be derived, using the equation:

$$\vec{F}_b = \vec{f}_{int} N_{int} \quad (3.11)$$

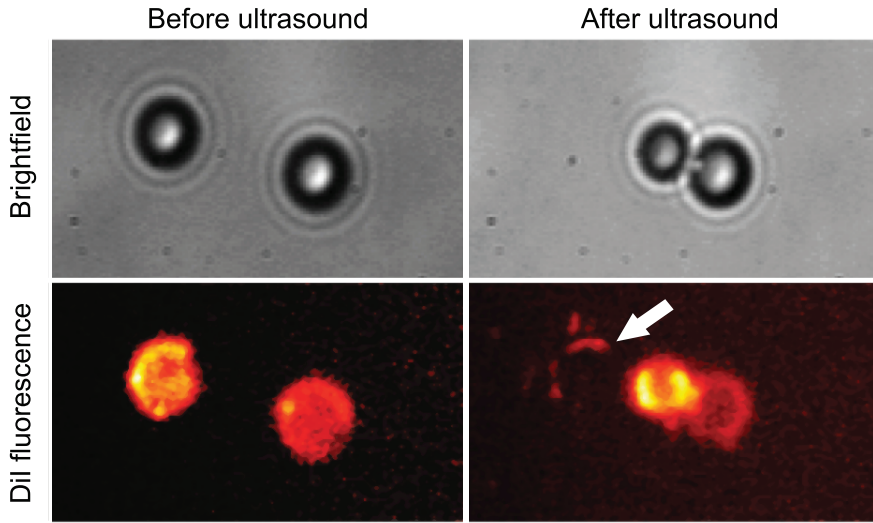


FIGURE 3.11: Top row: Brightfield images before (left) and after (right) ultrasound application. Bottom row: Corresponding DiI fluorescent images before (left) and after (right) ultrasound application. A semi-circular fluorescent patch (white arrow, indicative of lipids) is left at the initial binding site of the left bubble after detachment. The resting radii of the left and right bubble are 2.1 μm and 2.0 μm respectively.

with \vec{f}_{int} the strength of a single molecular interaction and N_{int} the total number of bonds involved. The strength of a molecular bond (\vec{f}_{int}) is known to be highly dependent on the applied loading rate (dF/dt) [104, 105]. The loading rate exerted on the bubbles (i.e. multiple bonds) due to the slow drift towards each other is in the order of 10^8 pN/s. Dependent on the number of bonds that are stressed just before detachment, the loading rate per molecular bond is expected to be in the range of 10^6 - 10^8 pN/s (i.e. between 10^2 bonds - 1 bond involved). Although no experimental data on molecular bond strength is available in literature for the

relatively high loading rates associated with the work presented here⁴, we can make an order of magnitude estimate of the number of bonds involved.

The value of \vec{f}_{int} in equation (3.11) depends on the locus of bond failure. The observation of patches of the fluorescent lipophilic dye DiI left at the initial binding site after microbubble detachment (see Figure 3.11) suggests that lipid anchors are pulled out of the microbubble shell instead of biotin molecules unbinding from avidin. At a loading rate of 10^4 pN/s, the force needed to pull the lipid anchor of the DSPE-PEG2000-biotin molecule out of a microbubble shell was measured to be ~ 35 - 45 pN, depending on the shell composition [106]. For comparison, the rupture force of the biotin-avidin interaction at similar loading rates was reported to be ~ 100 pN [105]. Lipid pullout therefore seems to be the weakest link and the most plausible locus of bond failure. As the strength of the lipid anchorage in the monolayer is expected to increase further with an increase in loading rate, dividing the measured binding force with $\vec{f}_{int} \sim 35 - 45$ pN gives an upper limit of the number of bonds involved. Using equation (3.11), we get $N_{int} \sim 20$ - 60 bonds. Most likely, molecular bonds throughout the contact zone between bubble and substrate will not be stressed uniformly during the unbinding process. Presumably, the molecular bonds at the distal margins of the adhesion zone will be stressed more and rupture first. When a certain threshold force is exceeded, the microbubble starts to detach from the functionalized substrate. The process then accelerates due to the ever-decreasing perimeter of the contact zone, a process best pictured as unzipping. Similarly, the threshold force for inducing cell mobility using shear flow has been ascribed to the properties of the molecular interactions at the trailing edge of the cell only [107].

The pressure threshold, above which the adhesion of the microbubbles is ruptured, depends on several factors. Shortening the pulse length will decrease the time during which the secondary Bjerknes force acts and it is expected to increase the threshold. Insonifying the bubbles at higher frequencies away from resonance will also increase the threshold. The pressure threshold is also affected by the adhesion

⁴Traditional force probes like the biomembrane force probe (BFP) and atomic force microscope (AFM) typically probe molecular bond strengths at significantly lower loading rates (10^{-1} - 10^5 pN/s for BFP and 10^4 - 10^5 pN/s for AFM)

strength between bubble and target surface. The biotin-avidin interaction used in this study is among the strongest non-covalent interactions in nature. Switching to a clinical relevant and biocompatible system (e.g. ICAM-1 or VEGFR-2) makes the bonds much weaker, ultimately leading to a lower pressure threshold for microbubble detachment. Moreover, repetitive insonation of the targeted microbubbles with low intensity ultrasound might induce bond fatigue, causing the bubbles to detach at lower pressures compared to bubbles insonified only once. In this study, the acoustical pressure was gradually increased until microbubble detachment was observed. Higher thresholds of detachment may be found when the bubbles are exposed to a single ultrasound burst only.

3.6 Conclusions

Targeted microbubbles subjected to secondary Bjerknes forces were observed to deform in the direction of their neighboring bubble, tending towards prolate spheroids. This deformation induces a restoring force driving the recoil observed after the ultrasound is turned off, typically occurring over $\sim 100 \mu\text{s}$. At higher acoustic pressures, microbubbles were observed to detach from the functionalized substrate, a process in which the pullout of lipid anchors from the microbubble shell is likely involved. The dynamics of mutually interacting targeted microbubbles during and after ultrasound application were captured with reasonable accuracy by a simplified hydrodynamic point particle model. Based on this mutual attraction, we have proposed a new method to measure the microbubble binding force. For bubbles studied here, a binding force of 1 - 2 nN was found.

Acknowledgements

This work was financially supported by the Dutch Technology Foundation STW (project 10507). The authors would like to thank F. Mastik for assistance with the Brandaris recordings and R. Beurskens, J. Honkoop, G. Springeling and M.

Manten for their technical assistance. Furthermore, we would like to thank Prof. Dr. Ir. L. van Wijngaarden from the University of Twente for the fruitful discussions about bubble deformation and A.R. van der Wal for the valuable remarks on the manuscript. The authors are grateful to Prof. Dr. A.L. Klibanov from the University of Virginia, Charlottesville, Virginia (USA), for providing information about microbubble fabrication.

3.7 Appendix

In this paper we presented the force balance for a targeted bubble translating in the x-direction due to an attractive secondary acoustic radiation force. In this force balance, a restoring force \vec{F}_k was included to account for the recoiling observed after the ultrasound was turned off. The magnitude of this restoring force was assumed to be proportional to the position of the center of mass (\vec{x}_i) of the bubbles. In this section we will show that this assumption is indeed justified.

Simultaneous top and side view high-speed imaging revealed that a targeted bubble, subjected to an attractive secondary acoustic radiation force, deforms in the direction of the neighboring bubble, tending towards a prolate shape (see side view images Figure 3.7). The cartoon in Figure 3.12 shows a schematic representation of this situation. The volume of a prolate ellipsoid is given by:

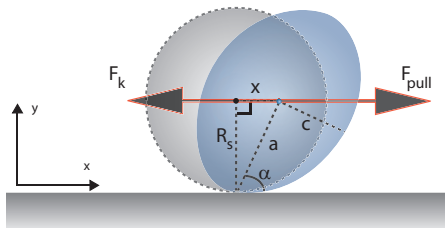


FIGURE 3.12: Cartoon of a targeted bubble (grey circle) deforming towards a prolate spheroid (in blue) when subjected to an external pulling force (F_{pull}). F_{pull} is opposed by a restoring force F_k . R_s is the radius of the bubble, x the translation of the center of mass, a and c the semi-major and semi-minor axis of the spheroid respectively and α the angle between a and the x-axis.

$$V = \frac{4}{3}\pi abc \quad (3.12)$$

with a, b , and c the semi-axes. If we assume the bubble obtains a prolate spheroid shape (i.e. $b=c$) and the deformation is volume conserving, we can state that:

$$V = \frac{4}{3}\pi ac^2 = \frac{4}{3}\pi R_s^3 \quad (3.13)$$

resulting in:

$$ac^2 = R_s^3 \quad (3.14)$$

with R_s the radius of a sphere with equivalent volume. In case of a volume conserving deformation, $R_s=R_0$. The surface area of a prolate spheroid is given by:

$$S = 2\pi c^2 \left\{ 1 + \frac{c}{ae} \arcsin e \right\} \quad (3.15)$$

with c the semi-minor axis, a the semi-major axis and:

$$e^2 = 1 - \frac{c^2}{a^2} = 1 - \frac{R_s^3}{a^3} \quad (3.16)$$

Using equation (3.14) in combination with some simple algebra, equation (3.15) can be recast into:

$$S = 2\pi R_s^2 \left\{ \frac{R_s}{a} + \sqrt{\frac{a}{R_s}} \frac{\arcsin e}{e} \right\} \quad (3.17)$$

If e is small ($R_s \sim a$), we can write:

$$\frac{a}{R_s} = 1 + \epsilon \quad (3.18)$$

and:

$$S = 2\pi R_s^2 \left\{ (1 - \epsilon) + \left(1 + \frac{1}{2}\epsilon\right)^2 \right\} \quad (3.19)$$

which can be reduced to

$$S = 2\pi R_s^2 \left\{ 2 + \frac{1}{4}\epsilon^2 \right\} \quad (3.20)$$

The work δW associated with a change δS in the surface area of a bubble is given by:

$$\delta W = \sigma \delta S \quad (3.21)$$

with σ the effective surface tension of the microbubble. Differentiating equation (3.20) with respect to ϵ gives:

$$\frac{\delta S}{\delta \epsilon} = \pi R_s^2 \epsilon \quad (3.22)$$

Using equation (3.18) we can rewrite equation (3.22) as a function of a :

$$\frac{\delta S}{\delta a} = \pi(a - R_s) \quad (3.23)$$

Substituting equation (3.23) into equation (3.21) yields:

$$\delta W = \sigma \pi (a - R_s) \delta a \quad (3.24)$$

The amount of work δW needed to elongate the bubble by δa should result from the work of the external pulling force. The external pulling force can be decomposed in two components, one component parallel to a and one component orthogonal to a . The work needed to elongate the spheroid by δa is then provided by the parallel component only and can be calculated by:

$$\delta W = F_{pull} \delta a \cos \alpha \quad (3.25)$$

with α the angle between a and the x-axis, see Figure 3.12. When the adhesion with the substrate is not disrupted, the pulling force (i.e. the sum of all the relevant hydrodynamic forces) is opposed by the restoring force, i.e. $F_{pull} = -F_k$.

Combining equation (3.24) and equation (3.25) and substituting F_{pull} by $-F_k$ gives:

$$F_k = -\frac{\sigma\pi(a - R_s)}{\cos \alpha} \quad (3.26)$$

Substituting $\cos \alpha = x/a$, $a = \sqrt{x^2 + R_s^2}$ and some rearranging yields:

$$F_k = -\sigma\pi x - \sigma\pi \frac{R_s(R_s - \sqrt{x^2 + R_s^2})}{x} \quad (3.27)$$

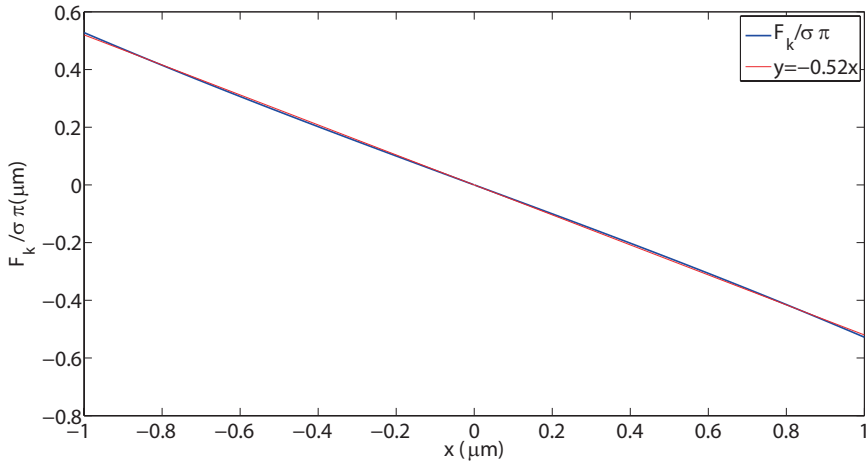


FIGURE 3.13: Plot of the variation of the term $F_k/\sigma\pi$ with the displacement of the center of mass in the x -direction (blue curve). The best linear fit ($y = -0.52x$) is also plotted (red curve).

In Figure 3.13 the variation of the term $F_k/\sigma\pi$ with x is plotted for the interval $-1 \mu\text{m} \leq x \leq 1 \mu\text{m}$. The linear relation $y = -0.52x$ gives a good overlap with the full equation on the interval relevant for the experiments described in this study, in which x typically varied from 0 to $\pm 0.5 \mu\text{m}$. This shows that for the experiments presented here, the assumption of a linear relationship between the restoring force \vec{F}_k and the position of the center of mass \vec{x}_i is justified.

Intravital microscopy of localized stem cell delivery using microbubbles and acoustic radiation force

Tom J.A. Kokhuis^{1,2}, Ilya Skachkov¹, Benno A. Naaijkens^{2,3}, Lynda J.M. Juffermans^{2,4}, Otto Kamp^{2,5}, Klazina Kooiman¹, Antonius F.W. van der Steen^{1,2,6,7}, Michel Versluis⁸ and Nico de Jong^{1,2,6}

¹Biomedical Engineering, Thorax Center, Erasmus MC, Rotterdam, The Netherlands

²Interuniversity Cardiology Institute of the Netherlands, Utrecht, The Netherlands

³Department of Pathology, VU University Medical Center, Amsterdam, The Netherlands

⁴Department of Physiology, VU University Medical Center, Amsterdam, The Netherlands

⁵Department of Cardiology, VU University Medical Center, Amsterdam, The Netherlands

⁶Acoustical Wavefield Imaging, Delft University of Technology, Delft, The Netherlands

⁷Shenzhen Institutes of Advanced Technology, Shenzhen, China

⁸Physics of Fluids Group and MIRA Institute of Biomedical Technology and Technical Medicine, University of Twente, Enschede, The Netherlands

Biotechnology and Bioengineering, in press, 2014

Abstract

The use of stem cells for the repair of damaged cardiac tissue after a myocardial infarction holds great promise. However, a common finding in experimental studies is the low number of cells delivered at the area at risk. To improve the delivery, we are currently investigating a novel delivery platform in which stem cells are conjugated with targeted microbubbles, creating echogenic complexes dubbed StemBells. These StemBells vibrate in response to incoming ultrasound waves making them susceptible to acoustic radiation force. The acoustic force can then be employed to propel circulating StemBells from the centerline of the vessel to the wall, facilitating localized stem cell delivery. In this study we investigate the feasibility of manipulating StemBells acoustically *in vivo* after injection using a chicken embryo model. Bare stem cells or unsaturated stem cells (< 5 bubbles/cell) do not respond to ultrasound application (1 MHz, peak negative acoustical pressure $P_- = 200$ kPa, 10% duty cycle). However, stem cells which are fully saturated with targeted microbubbles (> 30 bubbles/cell) can be propelled toward and arrested at the vessel wall. The mean translational velocities measured are $61 \mu\text{m/s}$ and $177 \mu\text{m/s}$ for $P_- = 200$ kPa and $P_- = 450$ kPa respectively. This technique therefore offers potential for enhanced and well-controlled stem cell delivery for improved cardiac repair after a myocardial infarction.

4.1 Introduction

Myocardial infarctions are a major burden on society and its public health systems, especially in the Western world. Continuous developments in the treatment of myocardial infarctions, have led to a growing number of patients that survive a myocardial infarction. Nevertheless, the loss of cardiac muscle cells and the formation of inflexible scar tissue makes this group of patients prone to develop congestive heart failure [108]. Restoration and repair of damaged cardiac tissue is therefore crucial for this group of patients.

Regeneration of the heart has been debated as early as the 19th century [109]. Zebrafish, for example, have the ability to fully regenerate their heart after a substantial loss of ventricular myocardial tissue [110]. Although there is evidence that the human heart is also capable of self-renewal [111], its regenerative capabilities as such are not sufficient to restore the contractile functioning of the heart after a myocardial infarction. Therefore, cardiologists started to investigate more interventional approaches like stem cell therapy, creating the field of cardiac repair. The use of mesenchymal stem cells to regenerate and repair damaged cardiac tissue seems appealing. Besides their capacity for cardiomyogenesis [112], stem cells have the potential to differentiate into smooth muscle cells and endothelial cells, therefore stimulating neovascularization [113]. Furthermore, stem cells secrete a protein cocktail which has salutary effects on the microenvironment, promoting tissue protection, repair and regeneration [114, 115].

Despite the potential of stem cell therapy for cardiac regeneration, the technique is currently hampered by the lack of persistence of a high number of stem cells at the area at risk. Typically, only a small fraction of the transplanted cells engraft within the diseased myocardium following injection, regardless of the route of administration [116–118]. However, the reduction in infarct-size and long-term improvement in cardiac functioning have been shown to correlate with the amount of cells grafted within the infarct zone [112]. Low stem cell engraftment rates therefore limit the regenerative potential of stem cell therapy.

The cardiac microvascular endothelium (CMVE) plays an important role in the homing and migration of circulating stem cells to the myocardium [119]. In a first step, circulating stem cells need to adhere to the target proteins at the endothelial cells for which direct contact with the microvascular endothelium is necessary. Several methods have been proposed to augment stem cell homing. One approach used is priming of the target tissue, which includes vibrating microbubbles [120], shock waves [121] or cytokines [122]. Other methods focus on the active targeting of the stem cells harnessing bispecific antibodies [123], bioactive molecules [124] or mRNA-transfection of the stem cells to express homing ligands [125]. All these techniques rely on the ability of stem cells to make contact with the target endothelium. However, circulating cells will predominantly be localized around the centerline of the vessel [25], an effect known as 'axial drift' [126]. This effect will therefore limit the number of stem cells that are able to adhere to the target endothelium, especially in the larger vessels of the microcirculation. A method to force the stem cells into direct and continuous contact with the vessel wall is therefore needed in order to enhance binding, retention and engraftment of stem cells in the infarcted area. Ideally, the delivery technique should be minimally invasive to avoid increased risks for morbidity and mortality.

In the field of molecular ultrasound imaging, targeted microbubble contrast agents are currently under investigation [17, 127]. Typically, these microbubbles are 1 – 10 μm in size and consist of a gas core stabilized by a thin lipid, polymer or protein shell equipped with ligands against specific molecular markers. Microbubbles scatter ultrasound very effectively giving them a superior echogenicity compared with the surrounding tissue. Moreover, in contrast to tissue, the acoustic response of microbubbles can be very non-linear, which can be exploited to discriminate between echoes originating from microbubbles and tissue [12, 80]. To improve the delivery of functionalized microbubbles to target sites on the vascular endothelium, the use of low-intensity ultrasound application has been proven advantageous [28, 29, 128]. This increased delivery of microbubbles can be ascribed to the effect of acoustic radiation force [86], propelling microbubbles away from the

transducer towards the vessel wall, bringing them into contact with the vascular endothelium [27].

Inspired by these findings, we have proposed a new technique to direct stem cells after injection by decorating the stem cells with functionalized microbubbles [129, 130]. We hypothesized that the conjugation with the microbubbles creates echogenic complexes, named StemBells, which are susceptible to acoustic radiation force. This force could then be employed to push the StemBells locally toward the vessel wall, arrest them in the damaged area of the heart and increase stem cell delivery.

The scope of this study is to investigate the feasibility of the ultrasonic manipulation of the position of StemBells within blood vessels in the presence of blood particles and pulsatile flow. We use intravital microscopy in a chicken embryo, which allows the direct optical observation of the effects of the acoustic radiation force *in vivo*. Translational dynamics were measured for different saturation grades (bare stem cells, unsaturated StemBells and saturated StemBells) and acoustic pressures.

4.2 Materials and methods

Stem cell culture

Cells from the stromal vascular fraction of human subcutaneous adipose tissue were cultured in low glucose Dulbecco's modified Eagle's medium (DMEM; Gibco, Life Technologies Europe, Bleiswijk, the Netherlands) containing 5 U/mL heparin (Leo Pharma, Amsterdam, The Netherlands), 100 U/mL penicillin (Gibco), 100 $\mu\text{g}/\text{mL}$ streptomycin (Gibco), 2 mM L-Glutamine (Gibco) and 5% human platelet lysate in a humidity incubator with 5% CO_2 as described previously [131]. Cells from passage 2-5 were used for the experiments. Figure 1.1A shows the size distribution of the stem cells (passage 5). The median diameter was 18 μm .

Fabrication of targeted microbubbles

Biotinylated microbubbles with a perfluorobutane (C_4F_{10}) gas core were made by sonication [50, 57]. The coating was composed of DSPC (59.4 mol %; Sigma-Aldrich, Zwijndrecht, the Netherlands), PEG-40 stearate (35.7 mol %; Sigma-Aldrich), DSPE-PEG(2000) (4.1 mol %; Avanti Polar Lipids, Alabaster, AL, USA) and DSPE-PEG(2000)-biotin (0.8 mol %; Avanti Polar Lipids). Antibodies against the surface protein CD90, constitutively expressed by the stem cells, were conjugated to the microbubbles using biotin-avidin bridging, as described by Lindner et al. (2001). Biotinylated microbubbles were washed three times at 400g for 1 min (Heraeus Biofuge, Thermo Scientific, Etten Leur, the Netherlands). After these three washing steps, the concentration of the microbubble solution was $\sim 1 \times 10^9$ microbubbles/ml; 0.5 mL of this microbubble solution was incubated with 20 μ g of streptavidin (S4762; Sigma-Aldrich) for 30 minutes on ice, after which the bubbles were washed twice and incubated with 5 μ g of the biotinylated monoclonal mouse anti-human CD90 antibody (BD Biosciences, Breda, the Netherlands) on ice for another 30 minutes. Afterwards, bubbles were washed once again and the concentration and size distribution was measured using a Multisizer 3 Coulter Counter (Beckman Coulter, Woerden, the Netherlands). The range of microbubble sizes within the solution varied between 1-8 μ m, with a median diameter of 3.0 μ m (see Figure 1.1B).

Construction of StemBells

The stem cells were fluorescently labeled with the nucleic acid stain Hoechst 33342 (Life Technologies Europe, Bleiswijk, the Netherlands). Subsequently, cells were trypsinized, washed and mixed with the CD90-targeted microbubbles by continuous rotation at 2 rpm for 30 min at room temperature (Rotator PTR-35, Grant-bio, Shepreth, UK). The mixing ratios (stem cell : microbubble) to get unsaturated (< 5 microbubbles/cell) and saturated StemBells (> 30 microbubbles/cell) were

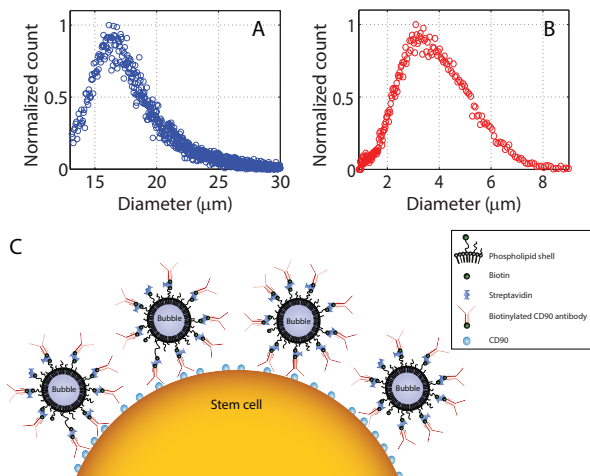


FIGURE 4.1: (A) Size distribution of adipose derived stem cells (passage 5); the median diameter was $18 \mu\text{m}$. (B) Size distribution of CD90-targeted microbubbles; the median diameter was $3.0 \mu\text{m}$. Both distributions were obtained using the Coulter principle. (C) Molecular architecture of a StemBell: a stem cell decorated with targeted microbubbles. Targeted microbubbles are linked to the stem cell via antibodies against the cell surface protein CD90.

1:10 and 1:200 respectively. Figure 1C shows the molecular architecture of the StemBells used in this study.

Chicken embryo model

Fertilized White Leghorn chicken eggs (*Gallus gallus domesticus*) were purchased from Drost BV (Loosdrecht, the Netherlands). After 5 days of incubation in a humidified incubator at 37°C (Heraeus, Thermo Scientific, Erembodegem-Aalst, Belgium), corresponding to stage HH27-27⁺ according to the Hamburger-Hamilton criteria [132], the embryo and containing egg yolk was taken out of the eggshell and transferred to the experimental setup. The cup holding the chicken embryo was embedded in a water bath kept at 37°C throughout the experiment using a heating element equipped with a thermostat. For the infusion of the samples, a custom-made catheter was used. The tip of the catheter, with an inner and outer diameter near $40 \mu\text{m}$ and $60 \mu\text{m}$ respectively, was pulled from a 1.2 mm glass capillary (World Precision Instruments, Berlin, Germany). The tip was glued

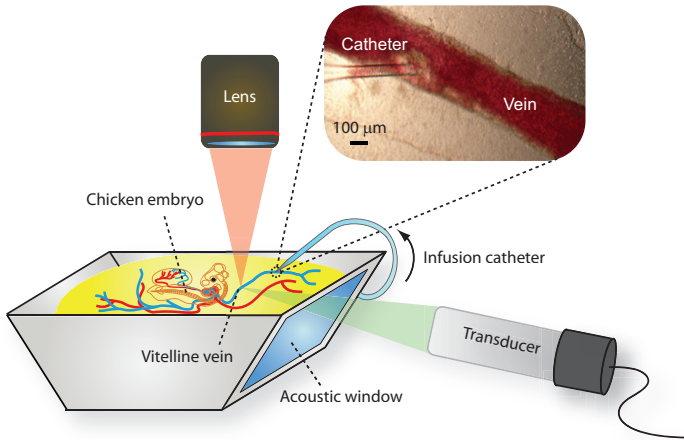


FIGURE 4.2: Experimental setup used for intravital microscopy. A 5-day-old chicken embryo was placed in a cup equipped with an acoustic window for the application of the acoustic radiation force. The transducer was mounted at a 20° angle with the horizontal axis and was acoustically coupled to the cup via a heated water bath. The optical focus of the objective lens was confocal with the acoustical focus of the ultrasound transducer. Samples were injected with a custom-made catheter in a vein upstream of the treated area (see inset).

into an infusion line and connected to a 1 mL syringe. A metal wire, partly wrapped around the tubing, facilitated easy handling of the catheter. After filling the catheter with the sample (500.000 cells/mL), it was placed into one of the vitelline veins after which the position was fixed using multi-silicone grease (OKS Spezialschmierstoffe, Maisach, Germany). Injections were done manually using a micromanipulator. Typically, a few μL of sample was infused per single injection. Due to the use of a catheter, multiple infusions and experiments could be conducted in a single vessel.

Optical and acoustic setup

The setup was positioned under a microscope (Olympus, Zoeterwoude, the Netherlands), equipped with a 5X objective (LMPlanFL, NA 0.13, Olympus) and an AxioCam MRc color camera (Carl Zeiss B.V., Sliedrecht, the Netherlands). The water tank was also holding a calibrated single element piston transducer (V303,

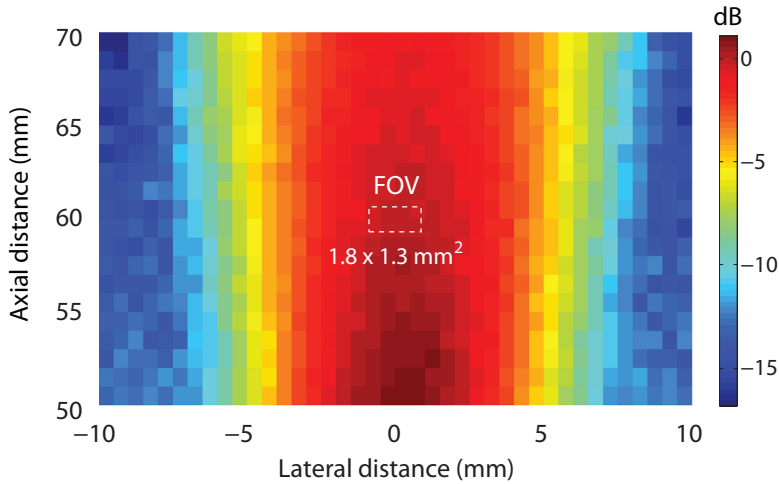


FIGURE 4.3: Acoustic intensity field map of the unfocused 1 MHz piston transducer. Radiation force experiments were performed in the far field at 60 mm from the transducer surface in the area indicated by the dashed box (FOV = field of view). The maximum variation in the acoustic intensity within the FOV was 0.4 dB, corresponding to less than 5 % variation in acoustical pressure.

Panametrics Inc., Waltham, MA, USA) used for the application of acoustic radiation force (1 MHz, 10% duty cycle, 10 seconds, peak negative acoustical pressure $P_- = 200$ kPa or 450 kPa). The optical and acoustical foci were aligned prior to each experiment. A schematic representation of the experimental setup is shown in Figure 4.2. Experiments were performed in the far-field (Fraunhofer zone) at 60 mm from the surface of the transducer to assure a uniform acoustical intensity field within the optical field of view (FOV), see Figure 4.3. The maximum FOV used in this study was 1.8×1.3 mm², in which the maximum variation in the acoustical intensity was measured to be 0.4 dB, corresponding to less than 5% variation in acoustical pressure.

Imaging protocol

The optical field of view during the experiment was located downstream with respect to the position of the catheter. Shortly after the start of the infusion, as

soon as the first fluorescently labeled cells passed by, image acquisition was initiated; ultrasound application was then automatically triggered with a time-delay of 5 seconds. The embryo could be maneuvered independently from the ultrasound transducer and microscope objective in the xyz -direction, allowing change of the region of interest during the experiment. All experiments were performed in vessels with a diameter between 150 – 400 μm .

4.3 Results

Response rate for different saturation grades

The radial displacement of the fluorescently labeled stem cells following acoustic forcing (1 MHz, $P_- = 200$ kPa, 10 seconds, 10% duty cycle) as a function of the saturation grade was studied using intravital time-lapse fluorescence microscopy. A total of 44 cells were analyzed. Figure 4.4A shows representative brightfield images of the three grades studied: a bare stem cell ($n=21$), an unsaturated StemBell ($n=11$) and a saturated StemBell ($n=12$) fully decorated with microbubbles. Single cells that were propelled away from the transducer toward the vessel wall after onset of the ultrasound were classified as 'responders'; cells that did not respond were classified as 'non-responders'. Figure 4.4B shows typical radial displacement-time curves obtained for responders (black curve) and non-responders (red curve). The purple bar indicates the time-window of ultrasound application. Both the bare stem cell and unsaturated StemBell population were not responsive to ultrasound application. However, 67% of the saturated StemBells responded and were propelled toward the vessel wall after onset of the ultrasound. The results are summarized in the table in Figure 4.4A.

After onset of the ultrasound, responding saturated StemBells exhibited a linear increase in traveled distance with time, until being immobilized at the vessel wall opposite to the location of the transducer. Figure 4.5 shows an example of the immobilization of three individual saturated StemBells following ultrasound

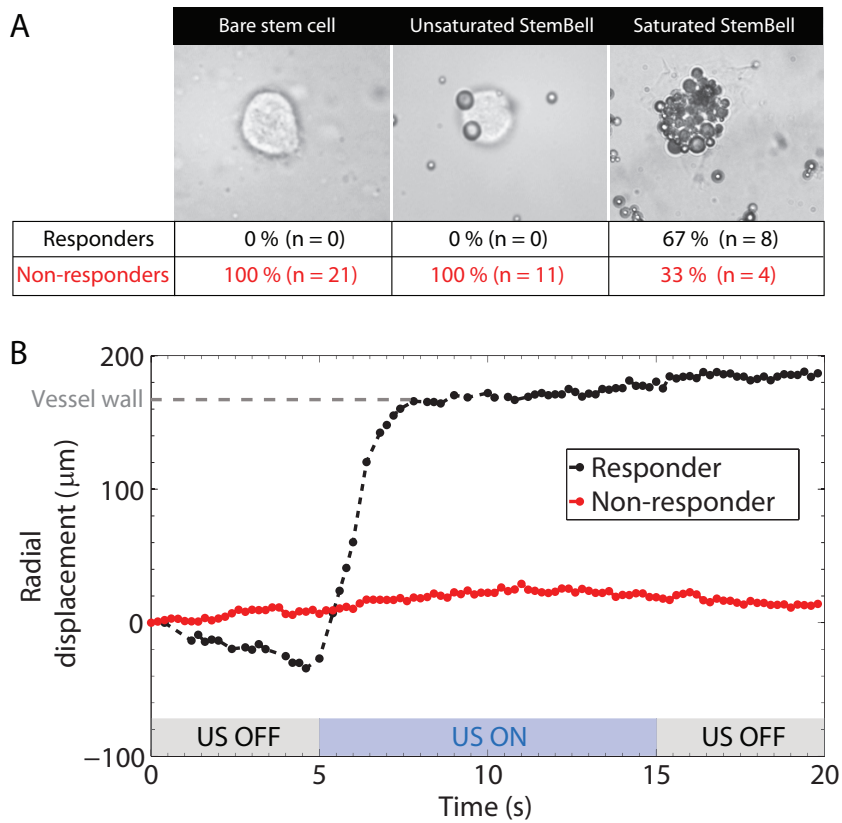


FIGURE 4.4: (A) Brightfield images of a bare stem cell, unsaturated StemBell and saturated StemBell. The response rate in each group are summarized in the table below. (B) Typical radial displacement-time curves obtained for responders (black) and non-responders (red), both obtained using $P_- = 200$ kPa. The blue bar indicates the time window of ultrasound (US) application.

application; Figure 4.5B shows the position of individual StemBells just before ultrasound application. The direction of the ultrasound and blood flow are shown in the schematic of Figure 4.5A. Application of ultrasound ($P_- = 200$ kPa) propels the StemBells across the $240 \mu\text{m}$ sized vessel, bringing them into contact with the distal vessel wall. Figure 4.5C shows the position of the StemBells after the ultrasound is turned off.

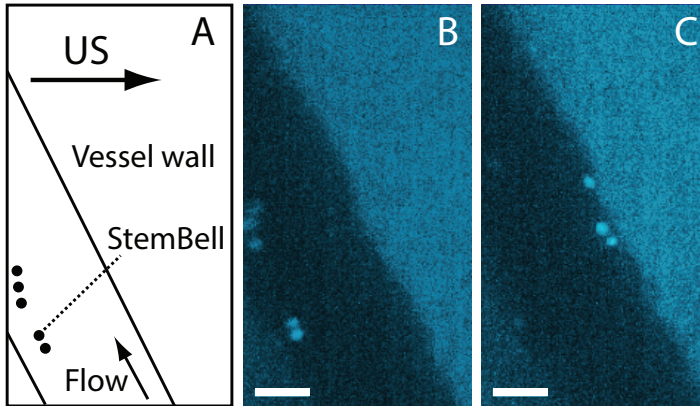


FIGURE 4.5: (A) Schematic of the situation before ultrasound application. (B) Snapshot showing the fluorescently labeled saturated StemBells before ultrasound application. (C) Snapshot showing the StemBells in contact with the vessel wall right after low intensity ultrasound application (10 seconds, $P_- = 200$ kPa, 10 % duty cycle). The scale bar corresponds to $100 \mu\text{m}$. See also video 1 online: <http://onlinelibrary.wiley.com/doi/10.1002/bit.25337/supinfo>.

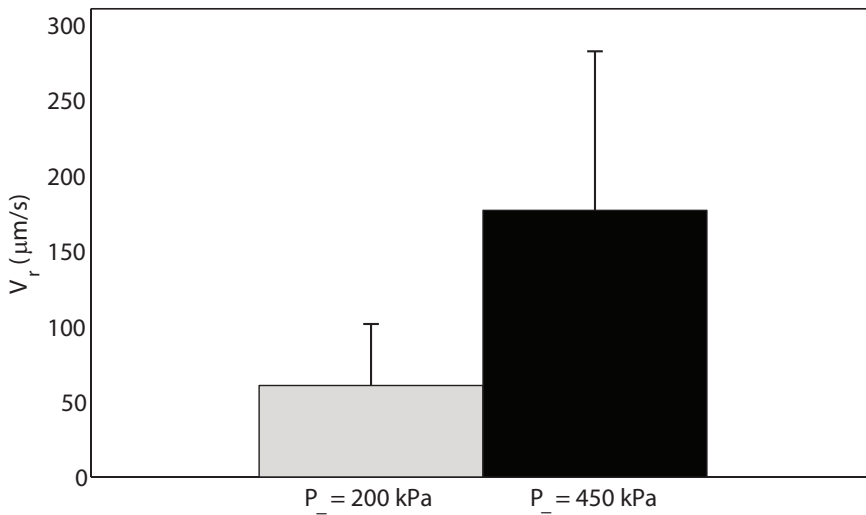


FIGURE 4.6: Mean radial velocity of saturated StemBells propelled by the acoustic radiation force for $P_- = 200$ kPa and $P_- = 450$ kPa.

Radial velocities of saturated StemBells

For each of the responding saturated StemBells, the radial velocity V_r was determined by differentiating the displacement curve with respect to time. Velocities

were measured for $P_- = 200$ kPa ($n=8$) and $P_- = 450$ kPa ($n=4$). Because the imaging by the CCD camera is not time-resolved, this velocity reflects the time-averaged non-instantaneous velocity of the complexes. At $P_- = 200$ kPa the StemBells were propelled with a mean velocity of 61 ± 41 $\mu\text{m/s}$. Increasing the pressure to $P_- = 450$ kPa increased the radial velocity of the StemBells by a factor of three up to 177 ± 105 $\mu\text{m/s}$ (see Figure 4.6).

4.4 Discussion

Stem cell therapy holds the potential to transform the treatment of heart failure. Current therapies for treating heart failure only delay the progression of the disease [133]. The possibility to repair damaged myocardium using stem cells would change the course of the disease. However, so far clinical trials on stem cell therapy have shown disappointing and contradicting results, complicating the assessment of the effectiveness of the therapy in general. A major issue of stem cell therapy is the lack of an effective delivery of stem cells at the site of interest. Because functional recovery of the heart correlates with stem cell engraftment [112], a reliable and controlled method to increase the homing of stem cells to the target tissue is needed.

By using intravital microscopy we have shown that stem cells saturated with microbubbles (i.e. saturated StemBells) can be pushed in a highly localized position to the wall of small microvessels using acoustic radiation force. Evidently, in case of unsaturated StemBells, the sum of the radiation forces acting on the few microbubbles attached to the cells is insufficient to propel the entire complex. Increasing the acoustical pressure will most likely at some point also induce displacement of the unsaturated StemBell population. However, increased acoustical pressure also increases the likelihood of microbubble destruction [134], which may counteract the effect of the increased radiation force on the bubbles [128]. Moreover, a low acoustical pressure also minimizes the occurrence of any negative bioeffects. Based on our present findings, we therefore argue that saturated StemBells require the

lowest pressure for acoustic forcing *in vivo*, and are therefore most favorable for ultrasound-mediated localized stem cell delivery.

Although the majority of the cells within the saturated StemBell-group responded to the acoustic radiation force, about 33% was found to be unresponsive at $P_- = 200$ kPa (see table in Figure 4.4A). By increasing the pressure to $P_- = 450$ kPa, the percentage of non-responders in the same group decreased to 20%. The fact that not all cells within the saturated StemBell-group were propelled by the acoustic radiation force can be explained by some degree of sample heterogeneity, with a small portion of the cells having no or only a few microbubbles attached. This effect can also be seen in the supplementary video, showing the presence of both acoustical responders and non-responders within the same sample.

Implications for cardiac application

Following a myocardial infarction, reperfusion therapy of the coronary artery restores the blood flow and oxygen supply to the infarct area of the cardiac muscle. Stem cell based therapies aim to promote cardiac repair of the injured and damaged area by the delivery of stem cells to the microvessels in the infarct area. The size of these microvessels varies between 10 – 500 μm [135]. The effect of the acoustic radiation force on the delivery of StemBells will be most beneficial in the larger vessels of the coronary circulation, in which the distance between the StemBells and the injured endothelial lining can be several hundreds of micron.

In this study we have shown that, by using 1 MHz ultrasound bursts, saturated StemBells can be propelled to the wall of tiny vessels with radial velocities of ~ 61 $\mu\text{m/s}$ ($P_- = 200$ kPa) and 177 $\mu\text{m/s}$ ($P_- = 450$ kPa). Similar to other particulate flows, e.g. red blood cells and microbubbles, the majority of the StemBells can be expected to be distributed around the centerline of the cardiac microvessels [25]. Based on the radial velocities measured here, the StemBells need to be in the volume of the interrogating ultrasound beam for several seconds to facilitate optimal stem cell delivery in all the microvessels. This is feasible considering

the rather low physiological blood flow velocities in the cardiac microcirculation, which are on the order of 1 mm/s [136]. It is important to emphasize that the time-averaged translational velocities measured in this study were obtained by using a ultrasound duty cycle of only 10 %. In fact, the velocities can be further boosted by increasing the pulse length of each ultrasound burst, up to a factor 10 when using continuous irradiation. This would then reduce the insonification time needed for effective stem cell delivery with the same factor.

The size of a myocardial infarct typically covers ~ 30 % of the left ventricle [137]. Therefore, to optimize stem cell delivery in the entire infarcted area, the ultrasound beam has to be scanned across the infarcted volume during the inflow of the StemBells. This can be easily overcome by the use of a 2D-matrix of transducers, facilitating simultaneous and continuous treatment of the infarcted area.

Future directions

The main goal of the present work was a proof of the working principle of a novel stem cell delivery technique *in vivo* and to study the translational dynamics of the stem cells as a function of the saturation grade (Figure 4.4) and acoustic pressure (Figure 4.6). The initial results look highly promising, however several aspects need further detailed studies in order to translate this technique into clinical practice.

One aspect is the long-term attachment efficiency of the StemBells which are continuously exposed to the shear forces of the blood flow. Long-term attachment is important for providing a time window for extravasation of the stem cells. Coating the stem cells with dual-targeted microbubbles, which besides the CD90 antibody, are also equipped with an antibody against a specific protein expressed on the injured endothelium, might be beneficial to further improve the delivery efficiency [130].

Another aspect is the migrational capacity of the StemBells, which is crucial for delivery and engraftment of the stem cells in the infarcted area. After being arrested at the vessel wall, StemBells have to cross the endothelial lining. Like leukocytes, bare stem cells have been shown to transmigrate over an endothelial barrier [138]. The extravasation of leukocytes is regulated via a process known as diapedesis, in which the cells squeeze through the endothelial border in a very active multi-step process [139], involving among others remodeling of the cytoskeleton. Although a similar mechanism has been proposed for the transmigration of stem cells [140], there is recent evidence that stem cells cross the endothelium via a process involving endothelial pocketing and vascular expulsion [141]. During this process, the extravasating cells themselves are rather passive and the entire process lasts up to 72 hours. However, the question remains whether the stem cells can already extravasate while still being surrounded by a layer of microbubbles. If not, there will be an idle period up to a few hours, dependent on the microbubble lifetime *in vivo* [142, 143], causing a delay in the onset of the transmigration. In that case, a microbubble destruction pulse at a high mechanical index (MI) to destroy the bubbles after the delivery of the StemBells might be beneficial to speed up the extravasation. Interestingly, microbubble destruction has been shown to improve transendothelial migration of stem cells in the myocardium [120]. Destruction of the microbubbles around the stem cell might therefore not only be a requisite, but even promote stem cell migration across the endothelium afterwards. However in all the scenarios, the presence of the microbubbles around the cell will be temporary. The lifetime of the microbubbles is relatively short compared to the extravasation time reported for stem cells. Therefore, we do not anticipate any microbubbles present around the cell after the transendothelial passage or any interference with the engraftment at a later stage.

Finally, the effects of acoustic radiation force are known to be optimal at the resonance frequency of the microbubbles [144, 145]. Although the resonance frequency of a single lipid shelled microbubble can be expected between 1-4 MHz [98], the close proximity of neighboring microbubbles is known to affect the bubble dynamics and resonance frequency [96]. We therefore studied the vibrational response

of StemBells as a function of the ultrasound driving frequency to further optimize our cell delivery technique. The exact details of the vibrational dynamics, both experimental and theoretical, will be presented in Chapter 5.

4.5 Conclusions

We have developed a new method for localized stem cell delivery using ultrasound radiation force and StemBells: stem cells decorated with targeted microbubbles. As proof of concept, StemBells were successfully delivered at the endothelium of microvessels in a chicken embryo. This ultrasound-mediated stem cell delivery technique therefore offers potential to increase the homing of stem cells to their target tissue in a minimally invasive manner.

Acknowledgments

This work was financially supported by the Dutch Technology Foundation (STW). The authors would like to thank Robert Beurskens (Biomedical Engineering), Geert Springeling and Michiel Manten (Experimental Medical Instrumentation) of the Erasmus Medical Center for their technical assistance. The valuable remarks of Anke van der Wal are also gratefully appreciated.

On the dynamics of StemBells:
microbubble-conjugated stem cells for
ultrasound-controlled delivery

Tom J.A. Kokhuis^{1,2}, Benno A. Naaijkens^{2,3}, Lynda J.M. Juffermans^{2,4}, Otto Kamp^{2,5}, Antonius .F.W. van der Steen^{1,2,6,7}, Michel Versluis⁸ and Nico de Jong^{1,2,6}

¹Biomedical Engineering, Thorax Center, Erasmus MC, Rotterdam, The Netherlands

²Interuniversity Cardiology Institute of the Netherlands, Utrecht, The Netherlands

³Department of Pathology, VU University Medical Center, Amsterdam, The Netherlands

⁴Department of Physiology, VU University Medical Center, Amsterdam, The Netherlands

⁵Department of Cardiology, VU University Medical Center, Amsterdam, The Netherlands

⁶Acoustical Wavefield Imaging, Delft University of Technology, Delft, The Netherlands

⁷Shenzhen Institutes of Advanced Technology, Shenzhen, China

⁸Physics of Fluids Group and MIRA Institute of Biomedical Technology and Technical Medicine, University of Twente, Enschede, The Netherlands

Manuscript in preparation for submission

Abstract

The use of stem cells for regenerative tissue repair is promising but hampered by the low number of cells delivered to the site of injury. To increase the delivery, we propose a new technique in which stem cells are linked to functionalized microbubbles, creating echogenic complexes dubbed *StemBells*. StemBells are highly susceptible to acoustic radiation force which can be employed after injection to push the StemBells locally to the treatment site. To optimally benefit from the delivery technique, a thorough characterization of the dynamics of StemBells during ultrasound exposure is needed. Using high-speed optical imaging, we study the dynamics of StemBells as a function of the applied frequency from which resonance curves were constructed. A theoretical model, based on a modified Rayleigh-Plesset type equation, captured the experimental resonance characteristics and radial dynamics in detail.

5.1 Introduction

Stem cell therapy holds the potential to regenerate damaged cardiac tissue after a myocardial infarction [146]. However, the low retention and engraftment rate of transplanted cells within the infarcted area is currently hampering successful myocardial regeneration [147]. Typically, only a few percent of the transplanted cells are retained in the infarcted area, even following intracoronary administration, with the majority of the cells ending up in the spleen and liver [117]. The reduction in infarct size and long-term improvement in cardiac functioning have been shown to correlate with the amount of engrafted cells [112], thus an efficient method facilitating enhanced and localized stem cell delivery is needed.

We propose a new technique for localized stem cell delivery using targeted microbubble ultrasound contrast agents and acoustic radiation force. Application of acoustic radiation force can be used to promote the delivery and adherence of targeted microbubbles *in vivo* [27, 28, 128]. By decorating stem cells with targeted microbubbles, acoustically active complexes named *StemBells* are created, which can be propelled locally toward and arrested at the vessel wall using acoustic radiation forces.

The effects of radiation force are maximum at the resonance frequency, where the volumetric oscillations are maximum [145, 148]. In order to optimize the propulsion, an acoustical characterization of the *StemBells* is needed. The aim of this study was therefore to characterize the *StemBell* dynamics in response to ultrasound waves using high-speed optical imaging.

5.2 Materials and Methods

Cells from the stromal vascular fraction of human adipose tissue were cultured in platelet lysate-supplemented medium [131]. Cells from passage 2-5 were used for the experiments; the median diameter of the cells was 18 μm . Biotinylated

lipid-coated microbubbles with a perfluorobutane (C_4F_{10}) gas core were made by sonication as described before [50, 57]. The median diameter of the microbubbles was 3 μm . Microbubbles were labeled with the lipophilic fluorescent dye octadecylindocarbocyanine (DiI, Molecular Probes, Life Technologies Europe, Bleiswijk, the Netherlands). Monoclonal antibodies against CD90 (BD Biosciences, Breda, the Netherlands), a cell surface protein constitutionally expressed by the stem cells, were conjugated to the microbubbles using biotin-avidin bridging, as described by Lindner et al. (2001). Cells were labeled with CellTracker Green CMFDA (Molecular Probes), trypsinized, washed and mixed with CD90-functionalized microbubbles (1:200 mixing ratio) by continuous rotation at 2 rpm (Rotator PTR-35, Grant-bio, Shepreth, UK) for 30 min at room temperature to create stem cells saturated with microbubbles. Here we mainly focused on the dynamics of saturated StemBells (i.e. > 30 bubbles/cell) as those were found to be most susceptible to acoustic forcing *in vivo*, which was presented in Chapter 4. StemBells were insonified at different pressures ($P_{-} = 50\text{-}200$ kPa) with a Gaussian tapered ultrasound pulse (4 - 8 cycles) at driving frequencies between 0.4 and 3 MHz. The pulse were generated with an arbitrary waveform generator (Tabor Electronics Ltd., Model 8026, Tel Hanan, Israel) and amplified by a 60 dB RF linear amplifier (ENI, Model A-500, Rochester, NY, USA). A broadband polyvinylidene fluoride (PVDF) transducer (PA275, Precision Acoustics, Dorchester, UK) was used between 1 and 3 MHz; a ceramic transducer (V318, Panametrics Inc., Waltham, MA, USA) with a center frequency of 500 kHz was used for frequencies below 1 MHz. All experiments were performed at 37°C. The dynamics of isolated StemBells was imaged with a customized BXFM microscope (Olympus Nederland B.V., Zoeterwoude, the Netherlands) using a 40X water-immersion objective lens (LUMPLFL, Olympus, numerical aperture 0.8) in combination with a 2X magnification ring. The optical and acoustical focus were co-aligned prior to each experiment. Images were relayed to the ultra-fast Brandaris128 camera [97, 149].

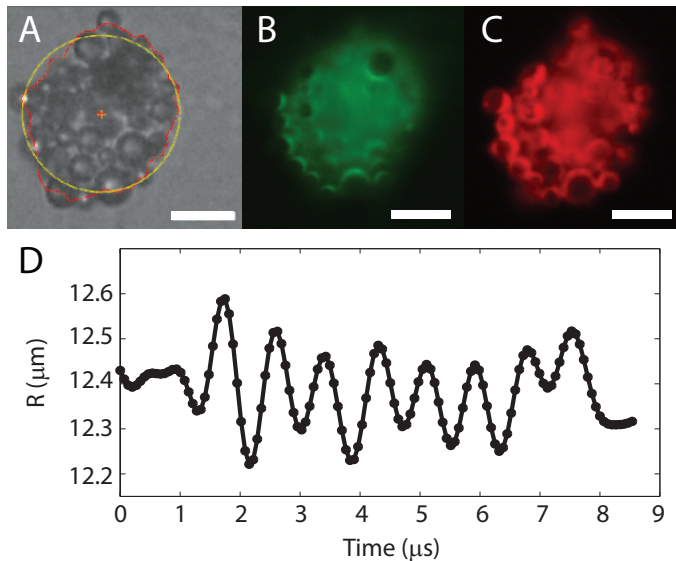


FIGURE 5.1: (A) Brightfield (B) green fluorescent (indicating the stem cell) and (C) red fluorescent (indicating surrounding microbubbles) images of a saturated StemBell. The radius of a StemBell was defined as the radius of the circle (yellow line panel A) with area equivalent to the area enclosed by the contour of the StemBells (red line panel A). The scalebar corresponds to $10\ \mu\text{m}$ (D) Radius-time curve of the StemBell in response to an 8 cycle ultrasound burst at 1.2 MHz and $P_- = 200\ \text{kPa}$.

5.3 Results and Discussion

Figure 5.1 shows brightfield (A), green fluorescent (B, showing the cell) and red fluorescent (C, showing the surrounding microbubbles) images of a StemBell saturated with targeted microbubbles; the resting radius of the StemBell is $12.4\ \mu\text{m}$. Saturated StemBells were observed to vibrate as a single entity. To quantify the response to an ultrasound burst, the StemBell contour was determined using custom software based on a minimum cost algorithm (see red line Figure 5.1A). The radius of a StemBell was defined as the radius of the circle with an area equivalent to the area enclosed by this contour (see yellow line Figure 5.1A). Using this contour detection technique, the experimental radius-time curve, $R(t)$, was determined. Figure 5.1D shows the $R(t)$ -curve of the StemBell in response to an 8-cycle ultrasound burst at a frequency of 1.2 MHz and driving pressure $P_- =$

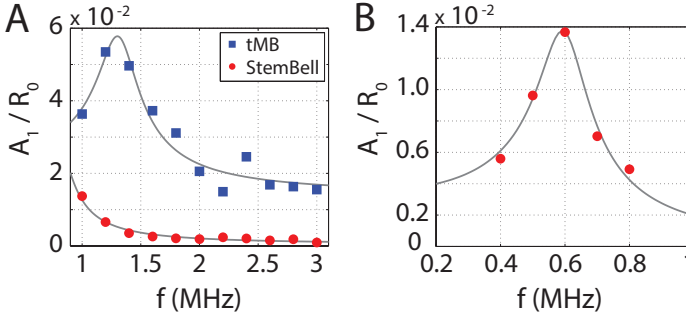


FIGURE 5.2: (A) Normalized fundamental vibration amplitude as a function of driving frequency for an adherent microbubble with resting radius $R_0 = 2.8 \mu\text{m}$ (blue squares) and a saturated StemBell with resting radius $R_0 = 12.6 \mu\text{m}$ (red dots). The amplitude of the driving pressure was 200 kPa. (B) Normalized fundamental vibration amplitude showing the relative fundamental amplitude response of a StemBell with an equivalent radius of $10 \mu\text{m}$ to driving frequencies from 0.4-0.8 MHz at $P_- = 50$ kPa.

200 kPa. The discrete Fourier transform of each $R(t)$ -curve was then calculated to determine the fundamental vibration amplitude (A_1) of the StemBell for each driving frequency, from which its resonance curve was constructed.

Figure 5.2A shows the relative fundamental vibration amplitude, A_1/R_0 , as a function of the driving frequency between 1 and 3 MHz for an isolated adherent microbubble attached to a stem cell (blue squares) and for a saturated StemBell (red dots). The resting radius of the adherent bubble is $2.8 \mu\text{m}$, which is equal to the mean volume-weighted radius of the microbubbles surrounding the saturated StemBell. The vibrational amplitude of the single bubble is maximal at a frequency of 1.3 MHz. However, in case of the StemBell only the falling edge of the resonance curve is captured, implying a resonance frequency < 1 MHz. Figure 5.2B shows the response of a saturated StemBell ($R_0 = 10 \mu\text{m}$) between 0.4 and 0.8 MHz (limited by the bandwidth of the transducer). The StemBell is resonantly excited at a driving frequency of 0.6 MHz, much lower than what might be expected based on the individual resonance behavior of the bubbles around the cell.

For bubble clouds it has been shown that the total gas volume or void fraction, and not the size of the individual bubbles within the cloud, dictates the resonance frequency [150]. Therefore, to corroborate our experimental findings, numerical

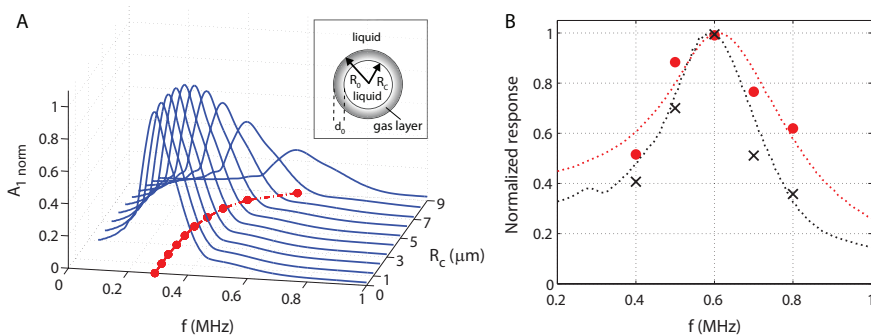


FIGURE 5.3: (a) Simulated resonance curves of the uncoated model system (i.e. $\chi = 0$, $\kappa_s = 0$ and $\sigma = 72 \text{ mN/m}$) as a function of R_c , while the total radius R_0 (see inset) was set at $10 \mu\text{m}$. The red curve shows resonance frequency versus R_c . (b) Comparison between experimental and simulated (dashed) resonance curves for two $10 \mu\text{m}$ radius StemBells at $P_- = 50 \text{ kPa}$. Good agreement with the experimental data was obtained for $\chi = 1.5 \text{ N/m}$ and $\kappa_s = 1 \times 10^{-7} \text{ kg/s}$ (black) $\chi = 2.8 \text{ N/m}$ and $\kappa_s = 3 \times 10^{-7} \text{ kg/s}$ (red). The values of R_c used in the simulations were set equal to the actual cell radii as determined by fluorescence microscopy: $6.7 \mu\text{m}$ (red) and $8.1 \mu\text{m}$ (black). The initial surface tension $\sigma(R_0)$ was set to 50 mN/m . The curves are normalized to the maximum value of A_1 .

simulations were performed using a modified Rayleigh-Plesset equation incorporating the total gas volume of the microbubble layer. The StemBell was modeled as a liquid globule (with radius R_c), surrounded by a thin gas layer of thickness d_0 . The central liquid core can be regarded incompressible compared to the compressibility of the surrounding gas layer. It was therefore assumed that, in response to an external pressure variation $P(t)$, only the radius R of the external gas/fluid interface will change, varying the volume V of the surrounding gas layer. The radius of the liquid core R_c was considered to be constant. Furthermore, similar to coated microbubbles [151], the gas layer was assumed to be coated with a viscoelastic lipid shell, with an effective shell elasticity χ and an effective shell viscosity κ_s . For such a system, a modified Rayleigh-Plesset equation can be defined, which reads:

TABLE 5.1: Notation

Symbol	Description
ρ_l	Liquid density
R	Outer radius
R_0	Resting radius outer wall
\dot{R}	Radial velocity outer wall
\ddot{R}	Radial acceleration outer wall
R_c	Radius liquid globule
d_0	Resting thickness gas layer
P_0	Ambient pressure
$P(t)$	Acoustic driving pressure
σ	Surface tension outer interface
γ	Polytropic gas exponent
μ	Dynamic liquid viscosity surrounding liquid
κ_s	Effective shell viscosity
χ	Effective shell elasticity

$$\rho_l(R\ddot{R} + \frac{3}{2}\dot{R}^2) = (P_0 + \frac{2\sigma(R_0)}{R_0})\left(\frac{R_0^3 - R_c^3}{R^3 - R_c^3}\right)^\gamma - \frac{2\sigma(R)}{R} - \frac{4\mu\dot{R}}{R} - 4\kappa_s\frac{\dot{R}}{R^2} - P_0 - P(t) \quad (5.1)$$

The shell elasticity was modeled through a radius-dependent surface tension, which for the small oscillation amplitudes can be approximated by its first order Taylor expansion [95]:

$$\sigma(R) = \sigma(R_0) + 2\chi\left(\frac{R}{R_0} - 1\right) \quad (5.2)$$

See Table 5.1 for a definition of the symbols used. Note that for $R_c = 0$, equation 5.1 reduces to the classical Rayleigh-Plesset equation of a coated gas bubble.

To investigate the resonance behavior of the model system described by equation 5.1, numerical simulations were performed. Initially, χ and κ_s were set to 0 (i.e. representing an uncoated gas layer) and the surface tension σ was set to 72 mN/m, corresponding to the surface tension of a clean gas-water interface. The resting radius of the complex R_0 (with $R_0 = R_c + d_0$, see inset) was kept constant at

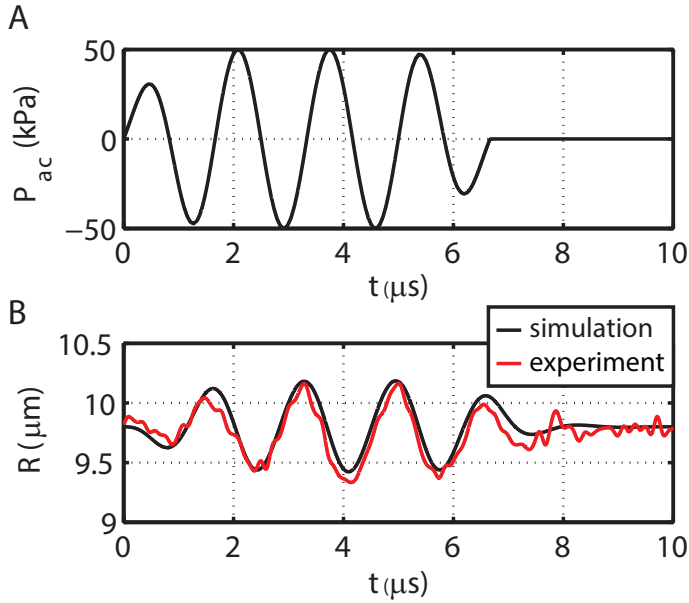


FIGURE 5.4: (A) Acoustical pressure wave of $P_{ac}=50$ kPa and $f = 0.6$ MHz. (B) Comparison of an experimental $R(t)$ -curve (red) and simulated $R(t)$ -curve (black). The simulation parameters were $\kappa_s = 8 \times 10^{-7}$ kg/s, $\chi = 2.8$ N/m, $\sigma(R_0) = 50$ mN/m and $R_c = 6.6$ μm . The resting radius of the StemBell was 9.8 μm .

10 μm ; the radius of the liquid core was varied between $R_c = 0$ μm , corresponding to a gas bubble, and $R_c = 9$ μm with 1 μm increments. The simulated resonance curves, normalized to the maximum response of the pure gas bubble, are shown in Figure 5.3A. It can be seen that increasing R_c (and therefore decreasing the total gas volume) shifts the resonance peak to higher frequencies, as indicated by the red curve. The experimentally obtained resonance frequency of a StemBell of 10 μm in radius was found to be around 0.6 MHz (see Figure 5.2B), which is about twice the predicted resonance frequency of a similar sized pure gas bubble (see Figure 5.3A, for $R_c = 0$). Part of this 0.3 MHz frequency shift can be explained by the lower amount of gas contained by a StemBell compared to a gas bubble. For example, in case of the StemBell of Figure 5.2B, with $R_c \sim 8$ μm as determined by fluorescence microscopy, the modified equation (assuming an uncoated gas layer) predicts the resonance frequency to be at 0.42 MHz. The remaining part of the shift can be

explained by the fact that the microbubbles surrounding the cell are coated with a lipid shell, introducing some degree of elasticity, thereby increasing the resonance frequency of the complex. In addition we find friction within system. We account for these effects via an effective shell elasticity χ and effective shell viscosity κ_s . By then optimizing the fits between the experimental and simulated resonance curves, unique values for χ (affecting the resonance frequency) and κ_s (affecting the width of the resonance curve) can be obtained. For values of $\chi = 1.5 - 3.0$ N/m and κ_s of the order of 10^{-7} kg/s, the model predicts the resonance frequency of the StemBells with good overlap with the experimental resonance curves. A comparison between the experimental and simulated (dashed) resonance curves of two StemBells (with $R_0 = 10 \mu\text{m}$) is shown in Figure 5.3B.

Moreover, the model also gives a rather good estimate of the amplitude of oscillations of the StemBells for similar values of χ and κ_s . This is illustrated in Figure 5.4B, showing the experimental (red) and simulated (black) $R(t)$ -curve of a $9.8 \mu\text{m}$ radius StemBell in response to the four-cycle ultrasound burst shown in Figure 5.4A ($f = 0.6$ MHz and $P_- = 50$ kPa). The parameter R_c was set to $6.6 \mu\text{m}$, which was obtained from the experimentally determined radius of the stem cell inside the StemBell.

5.4 Conclusions

In this paper we have investigated the vibrational dynamics of StemBells during ultrasound exposure. We found that the relatively low resonance frequency of saturated StemBells (~ 0.6 MHz) is governed by the collective oscillations of the surrounding microbubbles. A modified Rayleigh-Plesset equation, considering the total gas volume of the surrounding layer of microbubbles, captured the resonance behavior and vibrational dynamics of the StemBells in detail. The results of this study will help to further optimize this novel radiation force-assisted stem cell delivery technique.

Acknowledgments

This work was financially supported by the Dutch Technology Foundation (STW). The authors would like to thank Frits Mastik, Robert Beurskens, Geert Springeling and Michiel Manten for their technical assistance. The help of Dr. Klazina Kooiman is also appreciated. We also would like to thank Professor Andrea Prosperetti (Physics of Fluids Group, University of Twente) for the fruitful discussions related to the modeling of the StemBells.

Directing stem cells to the infarcted area using targeted microbubbles: StemBells.

Benno A. Naaijens^{1,2,3}, Tom J.A. Kokhuis^{3,4}, Paul A.J. Krijnen^{1,2}, Sylvia J.P. Bogaards^{2,5}, Elisa Meinster¹, Ilse A.E. Bollen¹, Hans Baltzer¹, Marco N. Helder⁶, Victor W.M. van Hinsbergh^{2,5}, Rene J.P. Musters^{2,5}, Nico de Jong^{3,4,7}, Otto Kamp^{2,3,8}, Hans W.M. Niessen^{1,2,9}, Annemieke van Dijk^{1,2} and Lynda J.M. Juffermans^{2,3,5}

¹Department of Pathology, VU University Medical Center, Amsterdam, The Netherlands

²Institute of Cardiovascular Research, VU University Medical Center, Amsterdam, The Netherlands

³Interuniversity Cardiology Institute of the Netherlands, Utrecht, The Netherlands

⁴Biomedical Engineering, Thorax Center, Erasmus MC, Rotterdam, The Netherlands

⁵Department of Physiology, VU University Medical Center, Amsterdam, The Netherlands

⁶Department of Orthopedics, VU University Medical Center, Amsterdam, The Netherlands

⁷Acoustical Wavefield Imaging, Delft University of Technology, Delft, The Netherlands

⁸Department of Cardiology, VU University Medical Center, Amsterdam, The Netherlands

⁹Department of Cardiac Surgery, VU University Medical Center, Amsterdam, The Netherlands

Manuscript in preparation for submission

Abstract

Stem cell therapy in acute myocardial infarction (AMI) is hindered by lack of engraftment of sufficient stem cells at the site of injury. We designed a novel technique to overcome this problem by assembling stem cell-microbubble complexes, named *StemBells*, through binding of microbubbles to stem cells via a CD90 antibody. StemBells were targeted to the infarcted area via an ICAM-1 antibody on the microbubbles. We showed that *in vitro* assembly of StemBells and exposure to ultrasound did not affect cell viability, and that StemBells are susceptible to acoustic radiation force. In an *in vivo* rat AMI model, StemBells significantly decreased infarct size 42 days post-AMI by 60%. This study therefore demonstrates the potential of this novel stem cell delivery technique for improved cardiac repair.

6.1 Introduction

Adult mesenchymal stem cell therapy has been proposed as a promising therapy for regenerative tissue repair, for example to prevent heart failure development after an acute myocardial infarction (AMI) [152, 153]. Adult mesenchymal stem cells can be harvested from for instance bone marrow or adipose tissue [154–156]. Both bone marrow derived mesenchymal stem cells (BM-MSC) and adipose tissue derived mesenchymal stem cells (ASC) have been shown to have a beneficial effect on cardiac function post-AMI in pre-clinical studies [157–159]. Unfortunately, clinical trials using BM-MSC or ASC therapy post-AMI showed no or only minor improvement in cardiac function [160–162]. One of the major problems is a lack of engraftment of sufficient stem cells at site of injury [163]. We hypothesized that when retention and engraftment of stem cells is increased, the therapeutic effect of stem cells will improve. Therefore, we designed a novel technique to direct stem cells specifically to injured endothelium of the blood vessels within the infarcted heart by coating them with dual-targeted microbubbles. These microbubbles are small ($1 - 10 \mu\text{m}$) gas-filled bubbles originally developed as contrast agents for echocardiography [22]. Nowadays, microbubbles can also be designed as targeting agents by conjugating antibodies, ligands or peptides to the microbubble shell [57, 58]. We have constructed stem cell-microbubble complexes, named *StemBells*, by coating ASC with microbubbles using a CD90 antibody via biotin-streptavidin bridging (see Figure 6.1). Additionally, a second antibody against ICAM-1, an adhesion molecule expressed on injured endothelium of blood vessels within the infarcted area [164], was simultaneously conjugated to the microbubble shell to improve attachment of the *StemBells* specifically in the infarcted area. We anticipated that application of the microbubbles has several beneficial effects. First, it allows coupling of a targeting antibody to the ASC without modifying the stem cell itself. Second, the addition of the microbubbles creates echogenic complexes which are susceptible to acoustic radiation force. This implies that *StemBells* can be pushed from the center of the blood stream to the vessel wall by ultrasound, further enhancing the effect of targeting. Here, we describe the development and

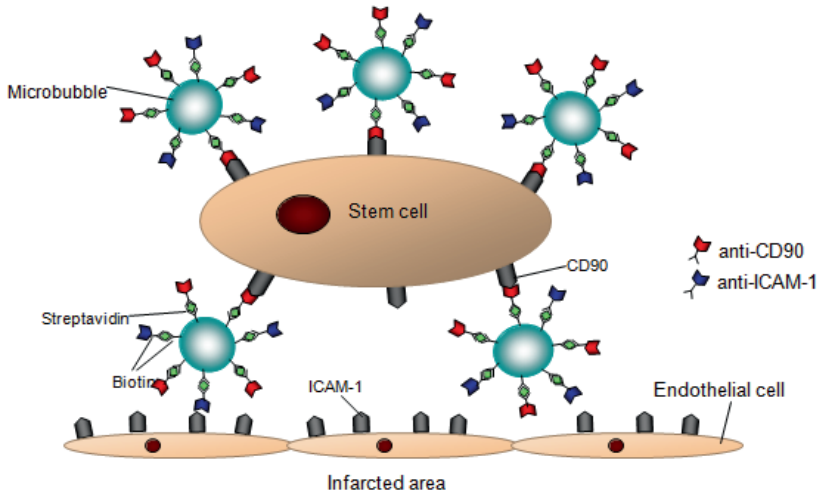


FIGURE 6.1: Schematic drawing of the novel cellular targeting technique using dual-targeted microbubbles. The stem cell-microbubble complex was named *StemBell*. StemBells were targeted to the injured endothelium via anti-ICAM-1.

validation of this novel StemBell technique divided in two steps: 1) *in vitro* assembly and characterization of the StemBells, and 2) an *in vivo* long-term functional rat AMI study to demonstrate their therapeutic effect on cardiac outcome.

6.2 Materials and methods

Isolation of the stromal vascular fraction from rat adipose tissue

Animals were treated according to national guidelines and with permission of the Institutional Animal Care and local Animal Ethical Committee of the VU University Medical Center (Amsterdam, The Netherlands), which conforms with the National Institutes of Health Guide for the Care and Use of Laboratory Animals (NIH Pub. No. 85-23, Revised 1996). Adipose tissue from the inguinal fat pad of 30 male Wistar rats (Harlan Laboratories, Horst, The Netherlands; 300-400g) was resected, pooled per 5 rats, collected in sterile phosphate-buffered

saline (PBS) and processed immediately after surgery [158]. Fat tissue was minced and washed with PBS. The extracellular matrix was enzymatically digested with 0.0125% Liberase TM Research Grade medium Thermolysin (Roche Diagnostics, Indianapolis, USA) under intermittent shaking for 25 min at 37°C. The mixture was filtered (100 µm; Codan, Germany) and centrifuged (5 min, 600g). The supernatant was discarded and the ASC containing pellet was resuspended in PBS and washed by centrifugation (5 min, 600g). Finally, the cell pellet (stromal vascular fraction; SVF) was harvested, the number of cells was counted where after they were frozen in RecoveryTM cell culture freezing medium (Gibco, Invitrogen, CA, USA), and subsequently stored in liquid nitrogen. To determine the percentage of ASC within the SVF a colony forming unit assay was performed by seeding SVF cells in 6-wells culture dishes (Greiner Bio one, USA) at a density of 10 and 100 cells/cm² (in triplicate) in ASC growth medium which consisted of low glucose Dulbecco's modified Eagle's medium (DMEM) containing 100 U/ml penicillin, 100 µg/mL streptomycin (all Gibco) and 10% fetal bovine serum (FBS; Hyclone, South Logan, USA), and culturing in a humidified atmosphere of 5% CO₂ at 37°C. Media were changed twice a week. After 14 days, cells were washed with PBS, fixed with 4% formalin for 10 minutes, and subsequently stained in a 1% toluidine blue solution in borax buffer for 1 minute and washed twice with H₂O. Colonies containing at least 50 cells were scored using a stereomicroscope (Zeiss, Germany). Prior to *in vitro* experiments or *in vivo* injection SVF from liquid nitrogen storage was thawed and seeded at 100,000 cells/cm² in ASC growth medium. When ASC reached 90% confluency, cells were detached with 0.5 mM EDTA/0.05% trypsin (Gibco). Cell size was determined using a ScepterTM handheld automatic cell counter (Millipore, Billerica, MA, USA). For *in vitro* experiments ASC in passage 1 or 2 were used, for *in vivo* experiments ASC was used in passage 1, cultured for six days.

StemBell assembly

Biotinylated microbubbles with a perfluorobutane (C_4F_{10}) gas core were made by sonification, as described before [50]. The shell was composed of DSPC (59.4 mol %; Sigma-Aldrich, the Netherlands); PEG-stearate (35.7 mol %; Sigma-Aldrich); DSPE-PEG (2000) (4.1 mol %; Avanti Polar Lipids) and DSPE-PEG (2000)-biotin (0.8 mol %; Avanti Polar Lipids). Microbubbles ($\sim 10^9$ /ml) had a mean diameter of (3.5 μm and were stored in sealed glass vials with a C_4F_{10} gas head-space to prevent deflation. Microbubbles remained stable when stored at 4°C for several weeks. To make dual-targeted microbubbles, 100 μL biotinylated microbubbles were first washed by centrifugation (1500 rpm, 1 min) to remove superfluous biotin. Next, streptavidin (1 mg/ml; Sigma) was added and the mixture was incubated for 30 minutes on ice. Microbubbles were again washed to remove superfluous streptavidin. Next, biotinylated mouse-anti-rat-CD90 (1 μg ; BD Bioscience) and biotinylated mouse-anti-rat-ICAM-1 (1 μg ; ACRIS) were added and the mixture was incubated for 30 minutes on ice. These dual-targeted microbubbles were again washed and resuspended in DMEM. Final concentration of the microbubbles was determined using a Multisizer 3 Coulter Counter (Beckman Coulter, Fullerton, CA, USA). The presence of both antibodies was verified using a Cy3-labeled anti-IgG1-mouse (Invitrogen) and a FITC-labeled anti-IgG2a-mouse (Invitrogen) by fluorescence microscopy (Marianas, I.I.I., Denver, CO, USA) with a 40x objective (Zeiss, Germany). Next, to assemble the StemBells, Hoechst-labeled ASC (10 $\mu\text{g}/\text{mL}$; Invitrogen) were incubated with dual-targeted microbubbles in a 100:1 ratio under continuous rotation at room temperature for 30 min. The number of microbubbles per StemBell was determined in 3D stacks obtained using differential interference contrast microscopy (Marianas) with a 40x objective. A minimum of 10 StemBells per experiment was analyzed.

Ultrasound application protocol

Ultrasound was applied using an unfocused 1 MHz piezoceramic transducer (V303-SU, Panametrics Inc, Waltham, MA, USA) or an unfocused 500 kHz piezoceramic transducer (V318, Panametrics Inc) coupled to an arbitrary waveform generator (33220A, Agilent, Palo Alto, CA, USA) and a linear 60 dB power amplifier (150A100B, Amplifier Research, Bothell, WA, USA). The ultrasound signal was monitored by a synchronized digital oscilloscope (Gould DSO 465, Valley View, OH, USA). Peak negative acoustic pressure was 100 kPa as verified with a calibrated hydrophone (PA076; Precision Acoustics, Dorchester, UK). ASC or StemBells in suspension were exposed to sine-wave ultrasound bursts with a 10% duty cycle and 1 kHz pulse repetition frequency for one minute. Rats were exposed to same ultrasound protocol by positioning the transducer parasternal at the anterior wall and location of the infarcted area.

Cell viability assay

Cell viability was analyzed by flow cytometry using an Annexin-V-FITC and Propidium Iodide (PI) Apoptosis Detection Kit (eBioscience, San Diego, USA), as described by the manufacturer, to test whether the assembly of StemBells, as well as application of ultrasound affected cell viability. In short, following StemBell formation with or without ultrasound treatment, cells were labeled with Annexin-V in the dark for 30 minutes. Prior to analysis, PI was added for at least 30 seconds. Expression of both Annexin-V and PI was measured with a FACS Calibur flow cytometer (BD Biosciences). Stem cells negative for both Annexin-V and PI were scored as viable. Data was analyzed with CellQuest-Pro software (BD Biosciences).

In vitro flow system to assess acoustic radiation force

A VI-slide flow chamber (Ibidi, Martinsried, Germany) was mounted on the Marianas microscope allowing real-time visualization of acoustic radiation force acting on flowing StemBells. Shear stress on the StemBells (1×10^6 cells/50 mL) was 0.2 dyn/cm^2 . Sequel bright field images were made at 20 Hz. Two seconds after onset of the video capture, the ultrasound was switched on until the end (total capture time 20 seconds).

Rat model of acute myocardial infarction

Eight week old male Wistar rats (300-400 grams, Harlan, the Netherlands) were housed under constant temperature ($21\text{-}22^\circ\text{C}$), humidity (60-65%) and light-dark periodicity (L:D 12:12). Experimental procedures started after two weeks of acclimatization. Rats were anaesthetized using subcutaneous hypnorm/dormicum (fentanyl and fluanison 0.5 ml/kg , midazolam 5mg/kg) injection, and were ventilated at 75 breaths/min, 10-0.4 mbar (Zoovent ventilator, Netherlands). Heart rate was monitored using Einthoven I ECG. A left thoracotomy in the fourth intercostal space was made, and the left anterior descending coronary artery was ligated using a 6.0 prolene suture (Ethicon, Germany). Ischemia was maintained for 40 minutes, followed by reperfusion and chest closure. This procedure results in relatively small non-aneurysmatic infarcts, comparable to what occurs in the majority of patients suffering from AMI [165].

In vivo long-term functional study

To show putative effects of StemBell technique cardiac function, a long-term study was performed in which AMI was induced in 52 rats. In this experiment 12 rats died during AMI induction and in five rats it was histologically determined after the experiment that AMI induction had failed. These 17 rats were excluded from further analysis. Seven days post-AMI rats received either 1×10^6 ASC in

600 μL DMEM (ASC group, $n=11$), 1×10^6 StB in 600 μL DMEM (StB group, $n=9$), 600 μL dual-targeted MB only (MB group, $n=8$) or Vehicle which consisted of 600 μL DMEM (Control group, $n=7$) in the tail vein under 3% isoflurane anesthesia. In this functional study all groups received ultrasound exposure following injection. For analysis of cardiac function, 2D-echocardiography was performed prior to AMI (day 0), prior to injection (day 7) and prior to sacrifice (day 42), using a 13 MHz linear-array transducer (ProSound SSD-4000 PureHD, Aloka, Tokyo, Japan). Analysis of the fractional shortening (FS) was determined by calculating the degree of shortening of left ventricular diameter between end-systole and end-diastole. Figure 6.2 shows the M-mode imaging results of the left ventricle (short axis) of the same rat before AMI induction at day 0 (A) and 7 days after AMI induction at day 7 (B). The red arrows indicate the left ventricular end diastolic diameter (LVEDd); the yellow arrows indicate left ventricular end systolic diameter (LVESd). Note that the left ventricle 7 days after AMI is somewhat enlarged compared to day 0 (before AMI), an effect known as ventricular dilatation [166, 167]. The lack of motion of the anterior wall after AMI induction (B) is clearly visible in the M-mode. The echogenic peaks along the posterior wall present during systole represent the papillary muscle entering the field of view.

Rats were sacrificed 42 days post-AMI, where after hearts were isolated and cut into five equal slices. Two slices were snap frozen in liquid nitrogen and three slices were embedded in paraffin. In addition, lungs were obtained and frozen in liquid nitrogen.

Histological staining to determine infarct size

To determine the infarct size a phosphotungstic acid haematoxylin (PTAH) staining was performed on three heart slides per rat distal from the suture. Slides were fixed for 10 minutes in 100% acetone and washed five times with PBS. The slides were then incubated in Bouin at 60°C for 30 minutes. After a cooling down period of 15 minutes and a wash step in water of 10 minutes, slides were incubated in PTAH at 60°C for 30 minutes. After cooling down, they were dehydrated, washed

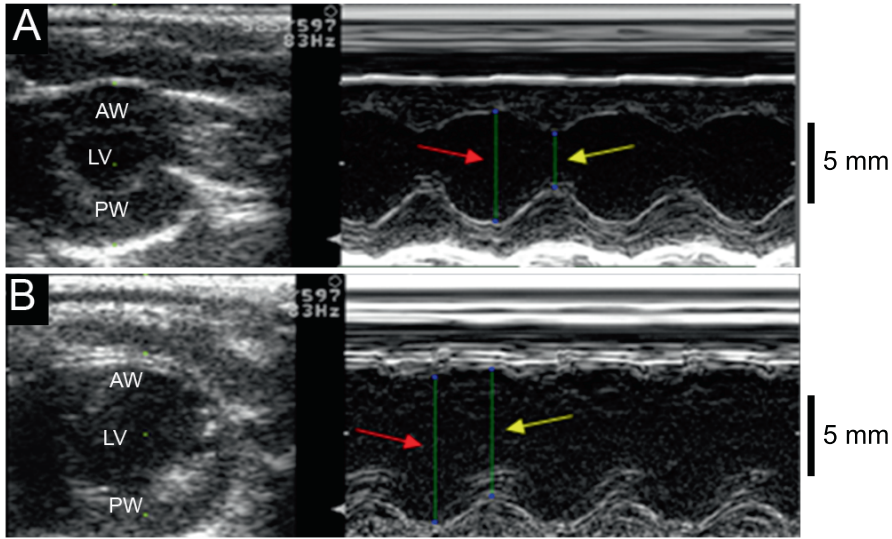


FIGURE 6.2: B-mode and M-mode imaging of the left ventricle (short axis) of a rat (A) prior to AMI induction (day 0) and (B) 7 days after AMI induction. AW: anterior wall; LV: left ventricle; PW: posterior wall. Please note the lack of motion of the anterior wall after AMI induction in panel B. The red arrows indicate the left ventricular end diastolic diameter (LVEDd); the yellow arrows indicate the left ventricular end systolic diameter (LVESd). The echogenic peaks along the posterior wall during the systole represent the papillary muscle entering the field of view.

in xylene and covered. PTAH stains viable cardiomyocytes purple and infarcted cardiomyocytes pink, allowing infarct size measurements using ImageJ software.

Fluorescence microscopy

To retrieve Hoechst-positive stem cell and determine putative differentiation in the long-term study four frozen heart slides per rat were counterstained with mouse monoclonal antibodies against troponin T (1:25, RT, overnight; AbD Serotec, UK) or connexin 43 (1:1000, RT, overnight; Abcam, Cambridge, UK), both followed by incubation with a goat-anti-mouse-FITC secondary antibody. Fluorescence microscopy (Marianas, Intelligent Imaging Innovations, Göttingen, Germany) was performed with a 10x and a 40x objective (Zeiss). Fluorescent images were analyzed using SlideBook software (Intelligent Imaging Innovations, Inc.).

Immunohistochemical staining of macrophages

To determine the inflammatory healing process post-AMI, the number and subtype of macrophages was determined by immunohistochemistry on serial paraffin slides using a mouse-anti-rat CD68 antibody for total numbers of macrophages (1:100, RT, 60 min; Serotec) after antigen retrieval with 0.1% pepsin (in 0.02M HCl, 37°, 30 min) or using a mouse-anti-rat ED2 antibody for the anti-inflammatory subtype of macrophages (1:200, RT, 60 min; a gift from prof. C.D. Dijkstra, VUmc, Amsterdam, the Netherlands) after antigen retrieval with 10mM sodium citrate buffer, pH 6.0, by boiling the slides in this buffer for 10 min. As secondary antibody Envision-HRP (1:200, 30 min, DakoCytomation, USA) was used. Staining was visualized using Envision-diaminobenzidin (DakoCytomation). Control slides incubated with PBS instead of primary antibody yielded no staining (not shown). CD68 and ED2 positive cells in the infarcted area were scored microscopically using a 20x objective (Zeiss, Germany).

Statistical analysis

All *in vitro* experiments were performed at least 6 times, unless described otherwise. The *in vitro* data, as well as the *in vivo* data of the infarct size and the number and subtype of macrophages were tested for normal distribution with one-sample Kolmogorov-Smirnov test. A student's t-test or ANOVA with Bonferroni post-hoc test was used, since all values were distributed normally. For the echocardiography data, non-parametric Kruskal-Wallis rank sum test was used, followed by ANOVA and Tukey multiple comparison of the means. A p-value smaller than 0.05 was considered to represent a statistically significant difference. Data is described as mean \pm standard deviation.

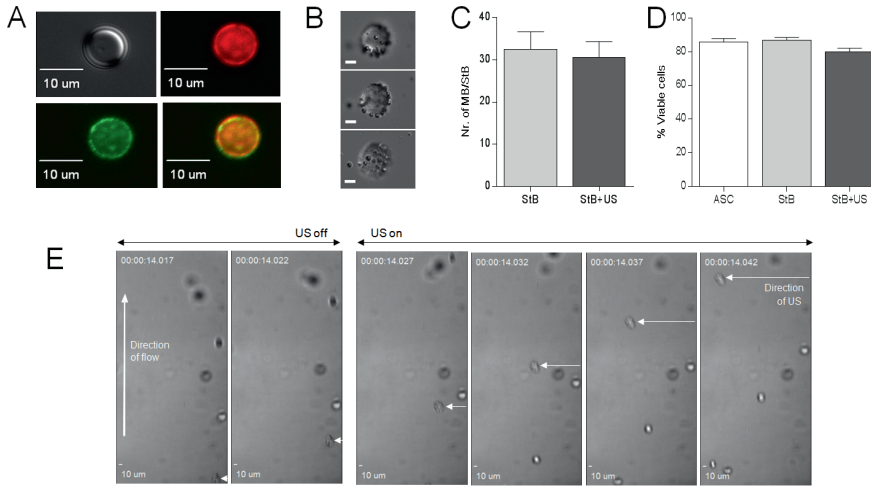


FIGURE 6.3: A) Microscopic images demonstrating presence of two antibodies on one microbubble. Upper left panel: bright field image; upper right panel: anti-CD90 in red; lower left panel: anti-ICAM-1 in green, and lower right panel is an overlay. B) Microscopic brightfield images showing three planes of a 3D stack of a StemBell. Scalebar represents 10 μm . C) Quantification of the number of microbubbles per stem cell, with an average of 32.5 ± 17.2 microbubbles per cell. Exposure to ultrasound (US) did not affect the number of microbubbles per cell. D) Quantification of cell viability assay using flow cytometry with Annexin V and PI. Cell viability in the ASC population was $85.7 \pm 5.6\%$. StemBell assembly, as well as exposing StemBells to ultrasound did not significantly decrease cell viability (StemBells: $87.1 \pm 3.3\%$ viable cells; StemBells + ultrasound: $79.9 \pm 5.5\%$ viable cells). E) Microscopic bright-field images demonstrating susceptibility of a StemBell in a flow system. Direction of flow is from bottom to top. Ultrasound exerts acoustic radiation force from right to left. Arrow indicates a StemBell in focus showing a 4 μm displacement in the direction of acoustic radiation force for every 10 μm in the direction of flow. Data is shown as mean \pm SD

6.3 Results

In vitro characterization of StemBells

Rat stromal vascular fraction cells were isolated from inguinal fat and pooled per five rats. The percentage colony forming cells indicating the number of stem cells in the stromal vascular fraction was $11.1 \pm 1.8\%$ ($n=7$, not shown). After a culture period of six days, ASC showed stem cell morphology with an average cell

size of $14.3 \pm 0.3 \mu\text{m}$ (not shown) in accordance to our previous studies [131, 158]. Dual-targeted microbubbles were successfully assembled showing presence of both anti-CD90 and anti-ICAM-1 antibodies on the microbubble shell (Figure 6.3A). Next, these dual-targeted microbubbles were added to ASC in a 100:1 ratio to form stem cell-microbubble complexes, named *StemBells* (Figure 6.3B). All ASC were coated with on average 32.5 ± 17.2 microbubbles per cell (Figure 6.3C). This number was not affected by ultrasound exposure (31.6 ± 15.4 microbubbles per cell). The procedure to assemble StemBells did not significantly affect cell viability (ASC: 85.7 ± 5.6 % viable cells; StB: 87.1 ± 3.3 % viable cells). Although exposure to ultrasound slightly decreased cell viability this was not statistically significant (StB+US: 79.9 ± 5.5 % viable cells), as shown in Figure 6.3D. Next, it was studied whether StemBells were susceptible to acoustic radiation force in an *in vitro* flow assay. Ultrasound displaced StemBells to the side of the flow channel in the direction of the ultrasonic wave propagation and perpendicular to the direction of flow (Figure 6.3E). It was found that for every $10 \mu\text{m}$ in the direction of the flow, a StemBell could be displaced $4 \mu\text{m}$ in the direction of the ultrasound wave propagation. ASC alone were not susceptible to ultrasound (not shown). These *in vitro* results made application of the StemBell technique possible for *in vivo* usage.

In vivo long-term functional study

In a following functional study we determined whether StemBell therapy improved cardiac outcome 42 days post-AMI. For this, 1×10^6 ASC (ASC, n=11) or StemBells (StB, n=9) were intravenously injected in rats seven days post-AMI. Two groups served as controls: 1) Vehicle group, injected with only non-supplemented DMEM (n=7) and 2) MB group, injected with dual-targeted microbubbles alone (n=8), to account for a potential effect of ultrasound-exposed microbubbles on cardiac outcome. All groups received ultrasound application for one minute post-injection. At day 42 post-AMI rats were sacrificed and the hearts were isolated. Infarct size per slide, determined by PTAH staining, was 13.6 ± 4.3 % in the Vehicle group

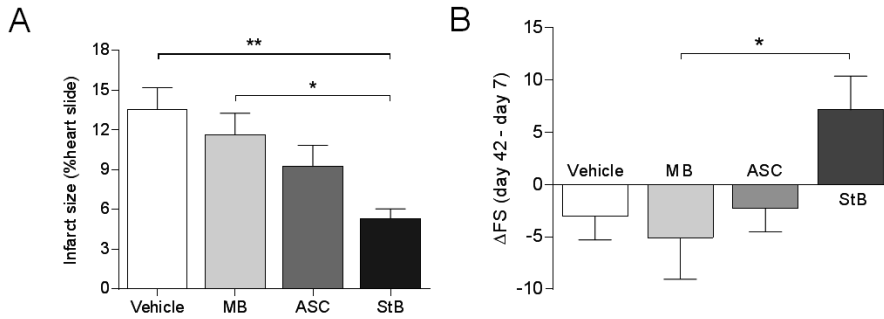


FIGURE 6.4: A) Quantification of PTAH staining of heart slides showing a significant decrease in infarct size in the StB group ($5.3 \pm 2.2\%$ of a heart slide) compared with Vehicle ($13.6 \pm 4.3\%$, $p < 0.01$) and MB ($11.6 \pm 4.6\%$, $p < 0.05$). B) Analysis of echocardiographic fractional shortening shown as change between day 42 and day 7 post-AMI (Δ FS) showing a trend towards improved cardiac function only in the StB group ($p = 0.11$ vs. Vehicle, $p < 0.05$ vs. MB, $p = 0.09$ vs. ASC). Data is shown as mean \pm SD

(Figure 6.4A). In the MB group infarct size was slightly but non-significantly decreased to $11.6 \pm 4.6\%$. ASC administration decreased the infarcted area to $9.2 \pm 5.3\%$. However, only in the StB group the infarct size was significantly reduced to $5.3 \pm 2.2\%$ compared with Vehicle ($p < 0.01$) and MB ($p < 0.05$). Next, echocardiographic images were analyzed to determine putative effects on cardiac function post-therapy. Analysis of the fractional shortening (FS), a measurement reflecting left ventricular contractile capacity is shown in Figure 6.4B as a change in FS between day 42 and 7 (Δ FS). Noticeable is that in the Vehicle, MB and ASC groups cardiac function deteriorated post-therapy, as shown by decreases in Δ FS (Vehicle: $-3.0 \pm 5.9\%$, MB: $-5.1 \pm 11.5\%$, ASC $-2.3 \pm 7.3\%$; Figure 6.4). Strikingly, only the StB group showed improvement in cardiac function post-therapy (Δ FS $+7.2 \pm 9.5\%$; $p < 0.05$ vs. MB group).

In this long-term study Hoechst-labeled stem cells were successfully retrieved. The majority was found as solitary cells within the infarct area, illustrated in the microscopic fluorescence image shown in Figure 6.5, obtained from a rat from the StemBell group. Green represents the expression of connexin 43, a marker for cardiomyocytes and therefore indicating viable tissue, whereas the darker areas represent infarcted areas. To verify whether the therapeutic effect of the stem

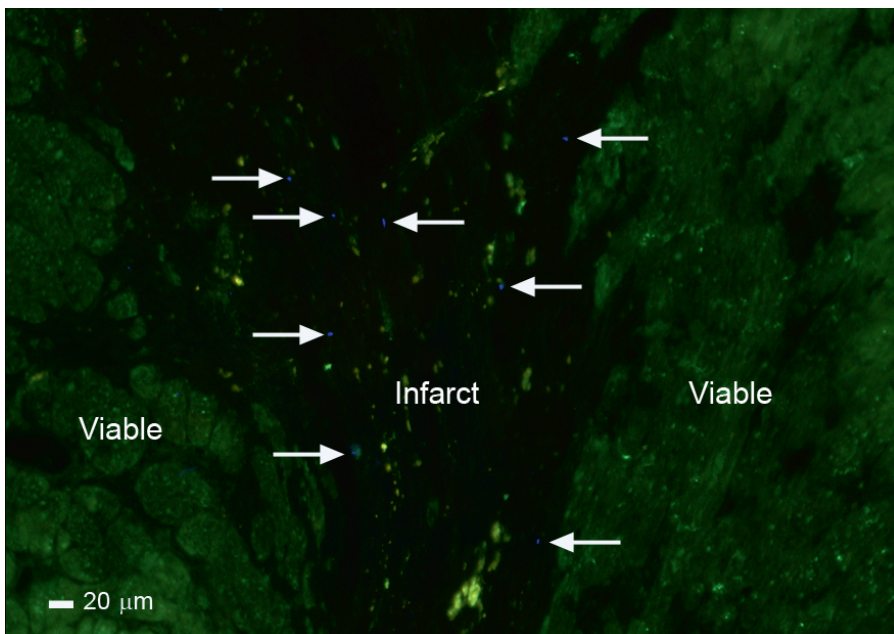


FIGURE 6.5: Fluorescence image of a connexin 43 (green) stained heart slide from the StemBell group showing presence of stem cells (blue dots, indicated by the arrows) within the infarct area at day 42.

cells coincided with differentiation into cardiomyocytes, retrieved Hoechst labeled adipose derived stem cells were tested for the expression of two cardiomyocyte markers: connexin 43 (Figure 6.6A) and troponin T (Figure 6.6B) [131]. Expression of both markers was found in all retrieved stem cells, not different between ASC and StB. However, the intensity levels of these markers were lower compared with healthy cardiomyocytes.

Finally, the number and subtype of macrophages within the infarcted area were quantified to determine a putative effect of the stem cells on the healing process post-AMI inflammation. The total number of macrophages (CD68 positive) per mm^2 did not differ between all groups, as shown in Figure 6.7A. The ratio of anti-inflammatory ED2 positive macrophages as a percentage of the total number of macrophages provides an indication for the healing rate in the infarcted area. Interestingly, this ratio was significantly higher in the StB group (0.85 ± 0.14) compared with Vehicle (0.50 ± 0.18 , $p < 0.05$), as shown in Figure 6.7B.

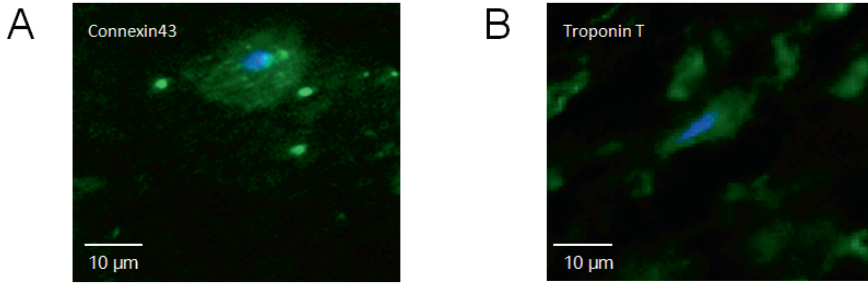


FIGURE 6.6: Retrieved Hoechst labeled stem cells at day 42 stained positive for cardiomyocyte specific markers connexin 43 (A) and troponin-T (B).

6.4 Discussion

In this study we described the development a novel technique to target stem cells specifically to the infarcted area by assembling stem cell-microbubble complexes, named StemBells. These StemBells were first characterized *in vitro*, showing high viability after assembly and ultrasound exposure, as well as susceptibility to acoustic radiation force. In a functional long-term study it was shown that administration of StemBells significantly improved cardiac outcome at day 42 post-AMI. After intravenous injection of StemBells or ASC no shortness of breath or other complications were observed and concordantly no massive obstruction by the injected stem cells were found in the lungs. In addition, these retrieved stem cells expressed cardiac markers. Finally, StemBell-treated rats showed a significantly higher percentage of anti-inflammatory macrophages within the infarcted area compared with controls.

The aim of this study was to optimize current stem cell therapy by our novel StemBell therapy. Previously, bi-directional antibodies against myosin light chain in mice [123] or VCAM in rats [168] were used to increase homing of hematopoietic stem cells to the heart, leading to better cardiac function after infarction measured by echocardiography. However, StemBells are in addition also susceptible to ultrasound, since we demonstrated that that ultrasound was able to displace StemBells

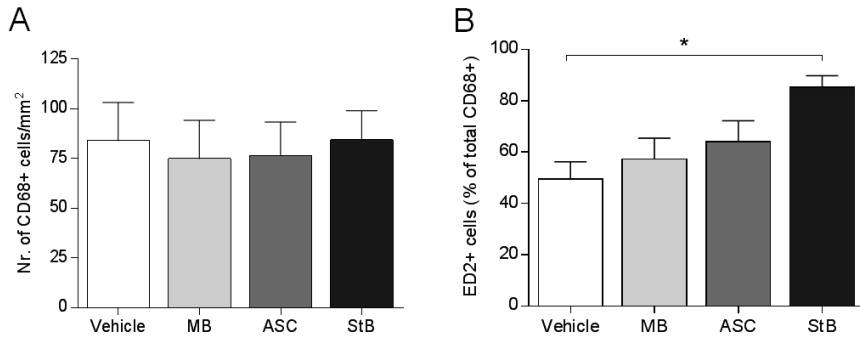


FIGURE 6.7: A) Quantification of the total number of macrophages (CD68 positive cells) in the infarcted area showed no differences between the groups. B) Quantification of anti-inflammatory macrophages (ED2 positive cells) expressed as percentage of total number of macrophages showed an increase in StB (85.2 ± 13.6%) compared with Vehicle (49.7 ± 17.6%, $p < 0.05$). Data is shown as mean ± SD.

over a relevant distance of tenths of microns *in vitro*. Therefore, the applied ultrasound *in vivo* theoretically facilitated contact to the dysfunctional endothelium in larger arterioles, where no initial contact of the StemBells occurred, by exerting acoustic radiation force [27]. Moreover, it can be hypothesized that ultrasound also caused an increase in the number of retrieved stem cells via exerting extra pressure to already-adhered StemBells, resulting in firmer adherence to the vessel wall, thereby enhancing the extravasation rate in relation to detachment by shear stress. The susceptibility of microbubbles and thus StemBells to ultrasound emphasizes the additional effect of using microbubbles in this technique in addition to using e.g. only targeting antibodies directly coupled to the stem cell. Using the StemBell technique, we found an improved cardiac outcome after therapy, such as a significant decrease in infarct size. Infarct size was reduced significantly by a striking 60% compared with the control group. ASC alone also reduced the infarct size compared with the control group by 33%, but not significantly. In other rat AMI studies wherein BM-MSc were injected 7 days post-AMI, two studies did not find a significant infarct size reduction (0% to 14% reduction) [169, 170], whereas three studies did (33% to 58% reduction) [158, 171, 172]. However, a comparison between the studies is difficult due to variations in the study set up, i.e. different time point of analysis, and different methods of injection. In the MB

group, infarct size was non-significantly reduced by approximately 15% compared with the Vehicle group. Dörner et al. found that treatment four days post-AMI with ultrasound and microbubbles had beneficial effects on the heart post-AMI by a significant 40% infarct reduction in mice two weeks post-AMI [173]. No later time point was shown in this study, thus whether this is a long term effect is not known. In addition, Dörner et al applied a 3-fold higher acoustic pressure than used in this study, at which the microbubble will display more violent behaviour such as collapse and jetting [89]. It can be hypothesized that indeed this may affect the infarcted heart. In our study, the acoustic pressure was set low to prevent microbubble destruction for an optimal effect of the primary acoustic radiation force on the StemBells. We did not aim for any possible effects on the infarcted as a result of cavitation itself, for which higher amplitudes might be more beneficial.

Finally, we analyzed by which mechanisms the administered stem cells might have improved cardiac function post-therapy. Interestingly, we could find stem cell within the infarcted area *in vivo* at day 42 post-AMI, indicating that the cells were able to survive within this harsh environment, as previously implied [155, 174]. These findings are in accordance with previous studies that found that BM-MSC were also located within the infarcted area in dogs seven days after injection [175] and 16 days after injection in rats [176]. The presence of cardiomyocyte specific markers connexin 43 and troponin-T on the retraced stem cells indicated differentiation towards cardiomyocytes [131, 177]. However, the low number of retraced stem cells, makes it highly unlikely that differentiation is a key mechanism. Recently it was described that the percentage pro- vs. anti-inflammatory macrophages is essential for infarct repair [178]. Therefore, we analyzed macrophage subpopulations to determine a potential effect of ASC on the course of inflammation post-AMI. We found that the StemBell group showed a significant increase in the percentage of anti-inflammatory macrophages compared with the control group. It has been described previously that BM-MSC therapy increased the percentage of anti-inflammatory macrophages in the infarcted area of mice three to four days post-AMI by a switch in subtype of the infiltrating macrophages [178, 179]. The results of this study indicate high potential of this

novel targeting technique. Although we focused on cardiac repair, this StemBell technique bears the perspective to be applicable in a variety of diseases that require regenerative cellular therapy, such as in neurodegenerative disease [180]. Recently triple-targeted microbubbles have been developed which further widened opportunities for specific targeting [43].

In conclusion, we demonstrated that the StemBell technique is feasible, and resulted in a significantly reduced infarct size post-AMI. As such, this StemBell platform is a promising technique to improve stem cell therapy.

Acknowledgments

This work was financially supported by the Dutch Technology Foundation (STW).

Conclusions and future perspectives

Abstract

Targeted microbubbles were the leitmotif of the work described in this thesis. The first part of the thesis focused on more generic aspects relevant to their utilization. These studies were performed to gain insight that aim for a better understanding and eventually an improved application of targeted microbubbles in general. In the second part of the thesis we report on the development of a novel application for targeted microbubbles: local stem cell delivery. In this chapter we present concluding remarks and future perspectives.

Molecular ultrasound imaging uses targeted microbubbles to detect molecular events *in vivo* [17]. This offers opportunities to non-invasively diagnose and monitor various diseases. It can also be used to detect the recurrence of a disease, a major issue in cancer treatment. The success of molecular ultrasound imaging depends on the ability to distinguish between adherent and freely-floating microbubbles. A common approach is to wait for 15-30 minutes until the free-floating microbubbles have been cleared from the circulation and only the adherent microbubbles remain. However, this is a rather time-consuming approach. Moreover, in the mean time the echogenicity of the adherent bubbles can deteriorate as a result of bubble deflation or bubble detachment. Alternative approaches have been proposed and include the use of low-pass interframe filtering to detect stationary bubbles [181] or the use of differences in binding dynamics in response to acoustic radiation force [182]. However, a robust discrimination solely based on the signature of the bounced echoes would be desirable.

Simulations have proven to be very helpful to improve the detection schemes for circulating contrast agents [183, 184]. Due to the complexity of the problem, no satisfactory model has been developed so far for adherent microbubbles, resulting in discrepancies between experiments and simulations [47, 185]. Current models developed for microbubbles *attached to* a wall, in fact represent bubbles *in contact with* a wall [185]. However, binding has a major effect on the vibrational response of a bubble [47, 186], most likely due to the mechanical constraint imposed on the microbubbles by the binding area with the substrate. These observations motivated us to characterize the binding area of adherent microbubbles using high-resolution fluorescence microscopy, which was presented in Chapter 2. A linear dependence between binding area radius (R_{bind}) and the resting radius before binding (R_0) was found. Interestingly, we found major differences in the binding area (> factor 5) between similarly sized microbubbles dependent on the main lipid component. This was also evident from the differences in shape between the two types of bubbles upon binding. These findings not only stress the influence of the shell composition, but will also aid in our understanding of adherent microbubbles and foster the development of improved models for adherent microbubbles.

In Chapter 3 we studied the effect of ultrasound application on adherent bubbles. More specifically, we focused on the quantification of the mutual interaction between (targeted) microbubbles, known as the *secondary Bjerknes force*. These experiments were inspired by the finding that ultrasound application resulted in the detachment of bound microbubbles and the formation of clusters, effects that were attributed to secondary Bjerknes forces [85]. Detachment of adherent microbubbles during ultrasound application will complicate molecular ultrasound imaging. Moreover, it will counteract the beneficial effect of the primary Bjerknes force on the binding efficiency [128]. Cluster formation can change the echogenicity and has been related to an increase in the fundamental response observed for adherent bubbles [83], making non-linear contrast detection techniques less effective. Understanding the effect of ultrasound on adherent microbubbles is crucial in order to optimally benefit from the potential of targeted microbubbles. We therefore investigated the mutual interaction between adherent microbubbles in detail using combined top and side view high-speed optical imaging [89]. An adherent microbubble, subjected to an attractive secondary Bjerknes force, was shown to deform in the direction of the neighboring bubble, up to a point where it detached from the functionalized substrate. A simplified hydrodynamic model, including a restoring term, captured the translational dynamics of the adherent bubbles during and after ultrasound application in detail.

The use of microbubbles as delivery vehicles for drugs and genes is well-established [22]. In Chapter 4 we have demonstrated that microbubbles can also be used for local stem cell delivery, for which we employed the susceptibility of the microbubbles to acoustic radiation forces. Stem cells surrounded by a layer of microbubbles can be propelled by acoustic radiation forces. By applying acoustic radiation force, we successfully delivered stem cells locally at the wall of chicken embryo vasculature, increasing the number of cells in the area receiving ultrasound therapy. Saturated StemBells were observed to vibrate as one entity with a relatively low resonance frequency, governed by the collective behavior of the surrounding microbubbles. A theoretical Rayleigh-Plesset-type model, only incorporating the total gas volume

of the microbubble layer, showed excellent agreement with the measured lower resonance frequency (Chapter 5). Finally, in Chapter 6 we have tested the feasibility of this technique for cardiac repair after a myocardial infarction in a rat model. Importantly, the intravenous injection of StemBells did not lead to major obstructions in the lungs and none of the animals showed complications (e.g. shortness of breath) afterwards. We found that only animals receiving StemBell-therapy showed a significant reduction ($> 60\%$) in infarct size compared to the control group. Moreover, only the StemBell-treated group showed an improvement in the long-term cardiac muscle function. These initial findings indicate that StemBells are highly promising to augment the outcome of stem cell therapy for cardiac repair.

Future perspectives

Based on the findings of the studies presented in this thesis, new ideas for future research evolved. These future perspectives are presented in this section.

Adherent microbubbles

As mentioned before, the behavior of microbubbles *adherent to* a wall is different from microbubbles *in contact with* a wall. The exact mechanism behind the observed differences remains to be solved. However, most likely the mechanical constraint imposed by the binding will result in an increased coupling between bubble dynamics and the wall [47], affecting the microbubble dynamics. We quantified the binding area of adherent microbubbles using high-resolution microscopy. A next step would be to investigate the dependency of the acoustic response of an adherent bubble (e.g. frequency of maximum response, amplitude of oscillation) on the binding area. For instance, it can be hypothesized that the acoustic response of adherent DSPC microbubbles, with a relatively small binding area (see Figure 2.6), will be more similar to the response of microbubbles in free contact

with a wall than in case of DPPC microbubbles. These studies could reveal the importance of the binding area on the microbubble dynamics. Furthermore, it would be interesting to investigate whether differences in the density of the target molecule on the substrate influence the vibrational dynamics of a microbubble. This would raise the opportunity to sense the degree of the expression of a target molecule based on the acoustic signature of the microbubbles, provided that these changes can also be detected in an *in vivo* setting.

The presumed therapeutic effect of long ultrasound pulses

In multiple studies on therapeutic applications of microbubbles, long ultrasound pulses (several thousands of cycles) were proven to be beneficial over shorter pulses. Moreover, not seldomly these long ultrasound pulses are used in combination with high acoustic pressures in the MegaPascal range [187], far above the destruction threshold of individual microbubbles. An important question is whether the therapeutical effects of long ultrasound pulses at destructive mechanical index ($MI > 0.4$), should be ascribed to the cavitation of the microbubbles or the effect of the ultrasound itself. However, Leeman and coworkers showed that, in case of microbubble-mediated sonothrombolysis, ultrasound alone did not have a thrombolytic effect [187], implying a significant role for the microbubbles in the thrombolysis event. Detailed information about the response of microbubbles to long ultrasound pulses (>100 cycles) is hampered by the limited time span ultrafast-framing cameras (> 10 MHz) cover. We therefore developed a new imaging mode for the Brandaaris 128 camera, facilitating high-speed imaging during small time windows (segments), equally distributed over a relatively large time span in the millisecond range (for details see [188]). This new mode was dubbed *segmented high-speed imaging*. We hypothesize that this new imaging technique will provide new insights why long cycles are beneficial over shorter cycles in the therapeutic realm of microbubbles. One of the explanations could be the formation of microbubble clusters due to secondary Bjerknes forces, which are known to be resistant to pressures and duty cycles destructive to single microbubbles

[84]. Alternative hypotheses include the formation of "daughter" bubbles as a result of bubble fragmentation or the continuous formation and collapse of new unencapsulated bubbles originating from the poorly soluble perfluorocarbon gas [187].

StemBells

Stem cell tracking using ultrasound

Several studies have shown a wide variability in the homing of cells between patients receiving stem cell therapy [189]. At the same time, it was shown that the amount of stem cells retained in the myocardium correlates with long-term cardiac improvement [190]. These findings emphasize that for a correct assessment of the efficacy of the therapy, there is a need to trace the fate and biodistribution of stem cells following injection. Currently, single-photon emission computed tomography (SPECT) and positron emission tomography (PET) are the most frequently used techniques to track stem cell *in vivo*. However, both techniques have some major drawbacks: (1) the requirement of a radioactive tracer, (2) the low spatial resolution and (3) a rather high detection limit of $\sim 10^4$ cells [191]. Ultrasound-mediated stem cell tracking would be an interesting alternative to these techniques. In the first place because there is no exposure to damaging radiation. Second, ultrasound outperforms both techniques on spatial resolution [191]. Furthermore, ultrasound has the ability to detect single microbubbles [57]. A recent study showed that ultrasound can detect single progenitor cells that had internalized lipid-shelled ultrasound contrast agents [192]. However, coating the stem cells with microbubbles, as performed in the studies described in this work, has some advantages over phagocytosing the microbubbles. First of all, when bubbles surround the cell, microbubbles can be equipped with targeting ligands against the target endothelium, as described in Chapter 6. Furthermore, because phagocytosis increases the volume of the cell and decreases the plasma membrane, a cell can only internalize a limited amount of particles [193]. In the study by Cui *et al*, cells contained 3-4 microbubbles on average [192], which is most likely not enough to facilitate

radiation-force assisted cell delivery at low mechanical index (see Chapter 4). On the other hand, StemBells would facilitate active targeting of the complex and radiation force-assisted delivery, in addition to stem cell tracking, therefore optimally benefiting from the presence of the microbubbles.

After StemBells have been constructed, single (unbound) microbubbles will still be present in the solution (see Figure 4.4A). To be able to track stem cells, it is paramount to either (1) separate the StemBells from the single microbubbles in the solution prior to injection *or* (2) to be able to discriminate between them acoustically after injection. Pilot experiments exploring the possibility to separate StemBells from single microbubbles, using among others Fluorescence Activated Cell Sorting (FACS) and Magnetic Activated Cell Sorting (MACS), were unsuccessful. Even though with FACS single microbubbles could be removed from the sample very efficiently within 20 minutes, the microbubbles attached to the stem cell were severely deflated by the static pressure imposed on the samples during FACS (data not shown). Separation using MACS was hampered by the low separation efficiency achieved with each washing step, eventually resulting in a low StemBells yield. Therefore, to facilitate stem cell tracking with ultrasound, a robust method to discriminate acoustically between single microbubbles and StemBells is desirable.

In Chapter 5 it was shown that saturated StemBells are not responsive at clinically relevant imaging frequencies (i.e. at frequencies >2 MHz). Because the StemBells do not vibrate at these frequencies, they will passively scatter the transmitted ultrasound, impeding the use of non-linear detection techniques typically used in ultrasound contrast imaging. Therefore, other options to discriminate between single bubbles and StemBells should be explored.

Microbubble aggregates are known to persist at acoustic pressures and duty cycles that destroy individual microbubbles [84]. A similar effect was observed when comparing the stability of individual microbubbles with those of StemBells in response to ultrasound exposure using high-speed imaging. An example is shown in Figure 7.1. Whereas the single microbubbles (bubbles 2, 3, 4 and 7) shrink in response

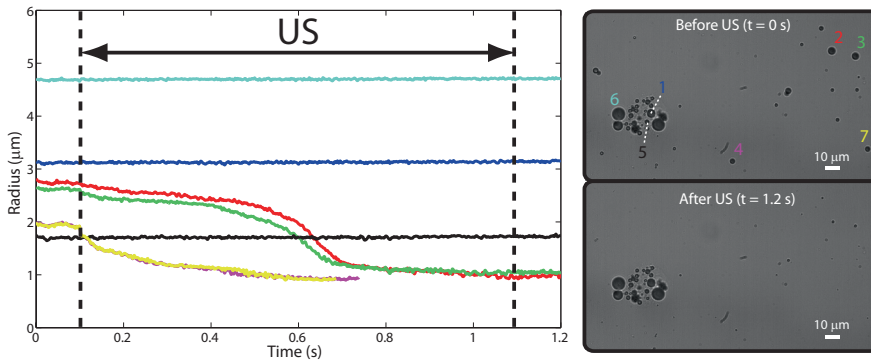


FIGURE 7.1: Selective crushing of unbound microbubbles at 37°C. The sample was insonified with ultrasound bursts of 3 cycles at 2.5 MHz and 100 kPa (duty cycle 1.2 %). The time window of ultrasound application is indicated by the black bar. On the right the corresponding microscopic images before (top) and after (bottom) ultrasound application. Each line represents the radius-time curve of the bubble annotated with the same color.

to ultrasound exposure, the microbubbles within the StemBell (bubbles 1, 5 and 6) remain stable throughout the experiment. Microbubble dissolution dynamics can be exploited with ultrafast plane wave imaging, facilitating the detection of changes in scattering with a temporal resolution of milliseconds [194]. Different dissolution rates were found for bound and free-flowing microbubbles, offering a possible criterium to discriminate between bound and unbound microbubbles in molecular imaging [194]. Based on the results shown in Figure 7.1, a similar approach may be proven successful to discriminate between single microbubbles and StemBells.

Another potential method involves employing the effect of acoustic radiation force. Acoustic radiation force can displace microbubbles (or StemBells, see Chapter 4) over a significant distance [148] and maximum displacement is observed when the driving frequency is near their resonance frequencies [145]. When a scatterer is displaced, the phase of the backscattered echo will change correspondingly which can produce evident Doppler effects [195, 196]. Differences in the displacements between microbubbles and StemBells could therefore be revealed by the phase shifts between successive imaging pulses, which can be interleaved by longer ultrasound bursts to generate enhanced radiation force effects. A dual-frequency

probe could facilitate independent optimization of both the acoustic radiation force pulses (lower frequency, longer pulses) and imaging pulses (higher frequency, short pulses). Moreover, to minimize motion effects generated by sources other than the radiation force (e.g. pulsatile blood flow), high frame rate imaging modalities should be employed. As this approach is based on radiation force-induced displacements, it is only feasible during the inflow and circulation phase of the contrast and not after the bubbles and StemBells have been immobilized at the endothelium. For example, it may provide information about the success of the injection procedure or about the potency of the StemBells to pass the pulmonary barrier and reach certain parts of the body, but not about their fate after extravasation.

An alternative approach is to use potential differences in the amplitude at the fundamental frequency in the echo spectrum of StemBells and individual bubbles. Dayton and colleagues found that the echo spectra of microbubble aggregates, when compared to individual microbubbles, are characterized by a higher intensity at the fundamental frequency [84]. In another study, Zhao et al. observed a significant increase in the intensity at the fundamental frequency (i.e. 14-22 dB), after forcing the microbubbles to bind to a coated vessel phantom using acoustic radiation force [49]. Interestingly, optical observation indicated that the adherent microbubbles had formed aggregates, suggesting the increase in intensity at the fundamental frequency of the echo spectrum resulted from aggregate formation, as reported before by Dayton et al. [84]. StemBells can also be interpreted as a aggregate of bubbles surrounding a cell. It would therefore be interesting to investigate whether StemBells also display a similar increase in the intensity at the fundamental frequency compared to the individual bubbles. Furthermore, higher frequency peaks might be suppressed, similar to what has been found for aggregates, resulting in a more narrow-band StemBell echo response [84]. This would offer possibilities for an acoustical discrimination between StemBells and individual bubbles, e.g. by employing the ratio between the intensity at the fundamental frequency and higher frequencies.

Finally, differences in the *in vivo* stability between individual microbubbles and StemBells could be an additional and relatively simple discrimination criterium on the long term. Selective StemBell imaging can then be performed after the individual microbubbles have disappeared.

The total time window available for ultrasound-mediated stem cell tracking depends on the lifetime of the microbubbles around the stem cells *in vivo*. Microbubbles that were internalized by progenitor cells could be detected up to 5 days after injection [192]. A similar study should be performed to assess the *in vivo* echogenicity of StemBells in time, e.g. by using the chicken embryo model described earlier in Chapter 4.

Effect of microbubbles on cellular response

In Chapter 6 we have shown that coating the stem cells with microbubbles and the application of the ultrasound does not affect the viability of the cells (see Figure 6.3D). However, whether the addition of the bubbles and application of ultrasound influences the proliferation, differentiation or paracrine pathways of the stem cells remains elusive and needs further investigation. For instance, it has been shown that during ultrasound exposure microbubbles can cause a hyperpolarization of the cell membrane [197], which has been shown to trigger cardiomyogenic differentiation of progenitor cells [198]. This can therefore offer possibilities to force stem cell differentiation in a specific direction. However, in cancerous cell lines, microbubble-mediated sonoporation was found to induce developmental delays [199]. Further optimization studies of our novel StemBell technique should therefore also include a thorough investigation of the (short and long term) cellular responses after ultrasound exposure. The outcome of such a study would facilitate the use of any desirable effects (e.g. directing the differentiation of the stem cells) while at the same time, prevent any unwanted side effects.

Additional steps to foster clinical translation

Large animal experiments (e.g. in pigs) need to be conducted to see whether StemBells can still cross the pulmonary passage and whether similar improvements can be obtained in cardiac functioning (infarct size, contractility). An intracoronary

injection could serve as an alternative route for an intravenous administration. This route was also used in the first human trial on adipose tissue-derived stem cells for cardiac repair [160]. Moreover, the immunogenic character of avidin [200], impedes clinical use of the current generation of StemBells. An alternative bridging strategy should therefore be developed to attach the ligands to the microbubbles, e.g. by using covalent thiol-maleimide linkages [82].

Bibliography

- [1] Samer Aljishi and Jakub Tatarkiewicz. Why does heating water in a kettle produce sound? *American Journal of Physics*, 59(7):628–632, 1991.
- [2] M. Versluis, B. Schmitz, A. von der Heydt, and D. Lohse. How snapping shrimp snap: through cavitating bubbles. *Science*, 289(5487):2114–7, 2000.
- [3] J. Roberts. The Codex Hammer of Leonardo da Vinci (Giunti Barbera, Florence, Italy), 1981.
- [4] A. Prosperetti. Bubbles. *Physics of Fluids*, 16(6):1852–1865, 2004.
- [5] Lord Rayleigh. On the pressure developed in a liquid during the collapse of a spherical cavity. *Phil. Mag.*, 34:94–98, 1917.
- [6] M.S. Plesset. The dynamics of cavitation bubbles. *J. Appl. Mech.*, 16:277–282, 1949.
- [7] R. Gramiak and P. M. Shah. Echocardiography of the aortic root. *Invest Radiol*, 3(5):356–66, 1968.
- [8] A. L. Klibanov. Ultrasound contrast agents: Development of the field and current status. *Contrast Agents Ii*, 222:73–106, 2002.
- [9] A. L. Klibanov. Ultrasound molecular imaging with targeted microbubble contrast agents. *J Nucl Cardiol*, 14(6):876–84, 2007.
- [10] J. A. Straub, D. E. Chickering, T. G. Hartman, C. A. Gloff, and H. Bernstein. AI-700 pharmacokinetics, tissue distribution and exhaled elimination kinetics in rats. *Int J Pharm*, 328(1):35–41, 2007.

-
- [11] N. de Jong, P. J. A. Frinking, A. Bouakaz, and F. J. Ten Cate. Detection procedures of ultrasound contrast agents. *Ultrasonics*, 38(1–8):87–92, 2000.
- [12] N. de Jong, M. Emmer, A. van Wamel, and M. Versluis. Ultrasonic characterization of ultrasound contrast agents. *Med Biol Eng Comput*, 47(8):861–73, 2009.
- [13] V. Mor-Avi, E. G. Caiani, K. A. Collins, C. E. Korcarz, J. E. Bednarz, and R. M. Lang. Combined assessment of myocardial perfusion and regional left ventricular function by analysis of contrast-enhanced power modulation images. *Circulation*, 104(3):352–357, 2001.
- [14] E. Unger, T. Porter, J. Lindner, and P. Grayburn. Cardiovascular drug delivery with ultrasound and microbubbles. *Adv Drug Deliv Rev*, 72C:110–126, 2014.
- [15] T. Fritzsich, D. Heldmann, and Weitschies W. Microparticle preparations made from biodegradable copolymers. *World Patent WO 94/07539*, 1994.
- [16] A. L. Klibanov, M. S. Hughes, J. N. Marsh, C. S. Hall, J. G. Miller, J. H. Wible, and G. H. Brandenburger. Targeting of ultrasound contrast material. an in vitro feasibility study. *Acta Radiol Suppl*, 412:113–20, 1997.
- [17] N. Deshpande, A. Needles, and J. K. Willmann. Molecular ultrasound imaging: current status and future directions. *Clin Radiol*, 65(7):567–81, 2010.
- [18] H. Wijkstra, M. Smeenge, J. de la Rosette, S. Pochon, I. Tardy-Cantalupi, and F. Tranquart. Targeted microbubble prostate cancer imaging with BR55. *Abstract Book of the 17th European symposium on Ultrasound Contrast Imaging, Jan. 19-20, Rotterdam, The Netherlands*, 2012.
- [19] Shiping Bao, Brian D. Thrall, and Douglas L. Miller. Transfection of a reporter plasmid into cultured cells by sonoporation in vitro. *Ultrasound in Medicine and Biology*, 23(6):953–959, 1997.
- [20] A. van Wamel, K. Kooiman, M. Harteveld, M. Emmer, F. J. ten Cate, M. Versluis, and N. de Jong. Vibrating microbubbles poking individual

- cells: drug transfer into cells via sonoporation. *J Control Release*, 112(2):149–55, 2006.
- [21] K. Kooiman, H. J. Vos, M. Versluis, and N. de Jong. Acoustic behavior of microbubbles and implications for drug delivery. *Advanced Drug Delivery Reviews*, 72(0):28–48, 2014.
- [22] P. A. Dijkmans, L. J. Juffermans, R. J. Musters, A. van Wamel, F. J. ten Cate, W. van Gilst, C. A. Visser, N. de Jong, and O. Kamp. Microbubbles and ultrasound: from diagnosis to therapy. *Eur J Echocardiogr*, 5(4):245–56, 2004.
- [23] J. Slikkerveer, P. A. Dijkmans, G. T. Sieswerda, P. A. Doevendans, A. P. van Dijk, F. W. Verheugt, T. R. Porter, and O. Kamp. Ultrasound enhanced pre-hospital thrombolysis using microbubbles infusion in patients with acute st elevation myocardial infarction: rationale and design of the sonolysis study. *Trials*, 9:72, 2008.
- [24] J. Slikkerveer, S. A. Kleijn, Y. Appelman, T. R. Porter, G. Veen, A. C. van Rossum, and O. Kamp. Ultrasound enhanced prehospital thrombolysis using microbubbles infusion in patients with acute ST elevation myocardial infarction: pilot of the sonolysis study. *Ultrasound Med Biol*, 38(2):247–52, 2012.
- [25] M. W. Keller, S. S. Segal, S. Kaul, and B. Duling. The behavior of sonicated albumin microbubbles within the microcirculation: a basis for their use during myocardial contrast echocardiography. *Circ Res*, 65(2):458–67, 1989.
- [26] V. F. K. Bjerknes. Fields of force. *Colombia University Press*, 1906.
- [27] P. Dayton, A. Klibanov, G. Brandenburger, and K. Ferrara. Acoustic radiation force in vivo: A mechanism to assist targeting of microbubbles. *Ultrasound in Medicine and Biology*, 25(8):1195–1201, 1999.

- [28] J. J. Rychak, A. L. Klibanov, K. F. Ley, and J. A. Hossack. Enhanced targeting of ultrasound contrast agents using acoustic radiation force. *Ultrasound Med Biol*, 33(7):1132–9, 2007.
- [29] Ryan C. Gessner, Jason E. Streeter, Roshni Kothadia, Steven Feingold, and Paul A. Dayton. An in vivo validation of the application of acoustic radiation force to enhance the diagnostic utility of molecular imaging using 3-D ultrasound. *Ultrasound in Medicine and Biology*, 38(4):651–660, 2012.
- [30] S. B. Feinstein, J. Cheirif, F. J. Ten Cate, P. R. Silverman, P. A. Heidenreich, C. Dick, R. M. Desir, W. F. Armstrong, M. A. Quinones, and P. M. Shah. Safety and efficacy of a new transpulmonary ultrasound contrast agent: initial multicenter clinical results. *J Am Coll Cardiol*, 16(2):316–24, 1990.
- [31] J. M. Correas, O. Helenon, L. Pourcelot, and J. F. Moreau. Ultrasound contrast agents. examples of blood pool agents. *Acta Radiol Suppl*, 412: 101–12, 1997.
- [32] C. Greis. Ultrasound contrast agents as markers of vascularity and microcirculation. *Clin Hemorheol Microcirc*, 43(1):1–9, 2009.
- [33] S. Kaul. Myocardial contrast echocardiography: a 25-year retrospective. *Circulation*, 118(3):291–308, 2008.
- [34] D. Cosgrove and C. Harvey. Clinical uses of microbubbles in diagnosis and treatment. *Med. Biol. Eng. Comput.*, 47(8):813–26, 2009.
- [35] A. L. Klibanov. Ultrasound contrast agents: Development of the field and current status. *Topics in Current Chemistry*, 222:73–105, 2002.
- [36] J. T. Sutton, K. J. Haworth, G. Pyne-Geithman, and C. K. Holland. Ultrasound-mediated drug delivery for cardiovascular disease. *Expert Opin Drug Deliv*, 10(5):573–92, 2013.
- [37] J. R. Lindner. Molecular imaging of myocardial and vascular disorders with ultrasound. *JACC-Cardiovasc. Imag.*, 3(2):204–211, 2010.

- [38] F. Kiessling, J. Bzyl, S. Fokong, M. Siepmann, G. Schmitz, and M. Palmowski. Targeted ultrasound imaging of cancer: an emerging technology on its way to clinics. *Curr Pharm Des*, 18(15):2184–99, 2012.
- [39] T. Faez, M. Emmer, K. Kooiman, M. Versluis, A. van der Steen, and N. de Jong. 20 years of ultrasound contrast agent modeling. *IEEE Trans Ultrason Ferroelectr Freq Control*, 60(1):7–20, 2013.
- [40] ICUS. What is CEUS? <http://www.icus-society.org/about-ceus/what-is-ceus>, 2014.
- [41] J. J. Rychak, J. R. Lindner, K. Ley, and A. L. Klibanov. Deformable gas-filled microbubbles targeted to P-selectin. *J Control Release*, 114(3):288–99, 2006.
- [42] E. A. Ferrante, J. E. Pickard, J. Rychak, A. Klibanov, and K. Ley. Dual targeting improves microbubble contrast agent adhesion to VCAM-1 and P-selectin under flow. *Journal of Controlled Release*, 140(2):100–107, 2009.
- [43] J. M. Warram, A. G. Sorace, R. Saini, H. R. Umphrey, K. R. Zinn, and K. Hoyt. A triple-targeted ultrasound contrast agent provides improved localization to tumor vasculature. *J Ultrasound Med*, 30(7):921–31, 2011.
- [44] A. S. Ham, A. L. Klibanov, and M. B. Lawrence. Action at a distance: lengthening adhesion bonds with poly(ethylene glycol) spacers enhances mechanically stressed affinity for improved vascular targeting of microparticles. *Langmuir*, 25(17):10038–44, 2009.
- [45] M. A. Borden, G. V. Martinez, J. Ricker, N. Tsvetkova, M. Longo, R. J. Gillies, P. A. Dayton, and K. W. Ferrara. Lateral phase separation in lipid-coated microbubbles. *Langmuir*, 22(9):4291–4297, 2006.
- [46] L. M. Kornmann, K. D. Reesink, R. S. Reneman, and A. P. Hoeks. Critical appraisal of targeted ultrasound contrast agents for molecular imaging in large arteries. *Ultrasound Med Biol*, 36(2):181–91, 2010.

- [47] M. Overvelde, V. Garbin, B. Dollet, N. de Jong, D. Lohse, and M. Versluis. Dynamics of coated microbubbles adherent to a wall. *Ultrasound Med Biol*, 37(9):1500–8, 2011.
- [48] P. A. Dayton, D. Pearson, J. Clark, S. Simon, P. A. Schumann, R. Zutshi, T. O. Matsunaga, and K. W. Ferrara. Ultrasonic analysis of peptide- and antibody-targeted microbubble contrast agents for molecular imaging of $\alpha_v\beta_3$ -expressing cells. *Mol Imaging*, 3(2):125–34, 2004.
- [49] S. K. Zhao, D. E. Kruse, K. W. Ferrara, and P. A. Dayton. Acoustic response from adherent targeted contrast agents. *Journal of the Acoustical Society of America*, 120(6):E163–E169, 2006.
- [50] T. J. A. Kokhuis, V. Garbin, K. Kooiman, B. A. Naaijken, L. J. M. Juffermans, O. Kamp, A. F. W. van der Steen, M. Versluis, and N. de Jong. Secondary Bjerknes forces deform targeted microbubbles. *Ultrasound in Medicine and biology*, 39(3):490–506, 2013.
- [51] D. H. Kim, A. L. Klibanov, and D. Needham. The influence of tiered layers of surface-grafted poly(ethylene glycol) on receptor-ligand-mediated adhesion between phospholipid monolayer-stabilized microbubbles and coated glass beads. *Langmuir*, 16(6):2808–2817, 2000.
- [52] V. Sboros, E. Glynos, J. A. Ross, C. M. Moran, S. D. Pye, M. Butler, W. N. McDicken, S. B. Brown, and V. Koutsos. Probing microbubble targeting with atomic force microscopy. *Colloids Surf B Biointerfaces*, 80(1):12–7, 2010.
- [53] T. M. Maul, D. D. Dudgeon, M. T. Beste, D. A. Hammer, J. S. Lazo, F. S. Villanueva, and W. R. Wagner. Optimization of ultrasound contrast agents with computational models to improve selection of ligands and binding strength. *Biotechnol Bioeng*, 107(5):854–64, 2010.
- [54] K. Kooiman, M. Foppen-Harteveld, A. F. van der Steen, and N. de Jong. Sonoporation of endothelial cells by vibrating targeted microbubbles. *J Control Release*, 154(1):35–41, 2011.

- [55] M. Schneider, M. Arditì, M. B. Barrau, J. Brochot, A. Broillet, R. Ventrone, and F. Yan. BR1: a new ultrasonographic contrast agent based on sulfur hexafluoride-filled microbubbles. *Invest Radiol*, 30(8):451–7, 1995.
- [56] FDA. Definity label. <http://www.fda.gov>, 2014.
- [57] A. L. Klibanov, P. T. Rasche, M. S. Hughes, J. K. Wojdyla, K. P. Galen, Jr. Wible, J. H., and G. H. Brandenburger. Detection of individual microbubbles of ultrasound contrast agents: imaging of free-floating and targeted bubbles. *Invest Radiol*, 39(3):187–95, 2004.
- [58] J. R. Lindner, J. Song, J. Christiansen, A. L. Klibanov, F. Xu, and K. Ley. Ultrasound assessment of inflammation and renal tissue injury with microbubbles targeted to P-selectin. *Circulation*, 104(17):2107–12, 2001.
- [59] S. Hell and E. H. K. Stelzer. Fundamental improvement of resolution with a 4Pi-confocal fluorescence microscope using two-photon excitation. *Optics Communications*, 93(5-6):277–282, 1992.
- [60] S. W. Hell, M. Schrader, and H. T. M. VanderVoort. Far-field fluorescence microscopy with three-dimensional resolution in the 100-nm range. *Journal of Microscopy*, 187:1–7, 1997.
- [61] W. A. van Cappellen, A. Nigg, and A.B. Houtsmuller. Enhancement of optical resolution by 4Pi single and multiphoton confocal fluorescence microscopy. In *Cellular Imaging Techniques for Neuroscience and beyond*, pages 55–80. Academic Press, Oxford, 2012.
- [62] G. Taubin. Estimation of planar curves, surfaces, and nonplanar space curves defined by implicit equations with applications to edge and range image segmentation. *Pattern Analysis and Machine Intelligence, IEEE Transactions on*, 13(11):1115–1138, 1991.
- [63] J. Schindelin, I. Arganda-Carreras, E. Frise, V. Kaynig, M. Longair, T. Pietzsch, S. Preibisch, C. Rueden, S. Saalfeld, B. Schmid, J. Y. Tinevez, D. J. White, V. Hartenstein, K. Eliceiri, P. Tomancak, and A. Cardona. Fiji:

- an open-source platform for biological-image analysis. *Nat Methods*, 9(7):676–82, 2012.
- [64] N. Emans, J. Biwersi, and A. S. Verkman. Imaging of endosome fusion in BHK fibroblasts based on a novel fluorometric avidin-biotin binding assay. *Biophysical Journal*, 69(2):716–728, 1995.
- [65] N. Marme, J. P. Knemeyer, M. Sauer, and J. Wolfrum. Inter- and intramolecular fluorescence quenching of organic dyes by tryptophan. *Bioconjug Chem*, 14(6):1133–9, 2003.
- [66] M. M. Lozano and M. L. Longo. Microbubbles coated with disaturated lipids and DSPE-PEG2000: Phase behavior, collapse transitions, and permeability. *Langmuir*, 2009.
- [67] M. A. Borden, G. Pu, G. J. Runner, and M. L. Longo. Surface phase behavior and microstructure of lipid/PEG-emulsifier monolayer-coated microbubbles. *Colloids and Surfaces B-Biointerfaces*, 35(3-4):209–223, 2004.
- [68] D. H. Kim, M. J. Costello, P. B. Duncan, and D. Needham. Mechanical properties and microstructure of polycrystalline phospholipid monolayer shells: Novel solid microparticles. *Langmuir*, 19(20):8455–8466, 2003.
- [69] M. M. Lozano and M. L. Longo. Complex formation and other phase transformations mapped in saturated phosphatidylcholine/DSPE-PEG2000 monolayers. *Soft Matter*, 5(9):1822–1834, 2009.
- [70] J. J. Kwan and M. A. Borden. Lipid monolayer collapse and microbubble stability. *Adv Colloid Interface Sci*, 183-184:82–99, 2012.
- [71] I. Lentacker, B. Geers, J. Demeester, S. C. De Smedt, and N. N. Sanders. Design and evaluation of doxorubicin-containing microbubbles for ultrasound-triggered doxorubicin delivery: Cytotoxicity and mechanisms involved. *Mol Ther*, 18(1):101–108, 2010.

- [72] A. L. Klibanov. Preparation of targeted microbubbles: ultrasound contrast agents for molecular imaging. *Medical and Biological Engineering and Computing*, 47(8):875–882, 2009.
- [73] Y. Kurniawan, C. Scholz, and G. D. Bothun. n-Butanol partitioning into phase-separated heterogeneous lipid monolayers. *Langmuir*, 29(34):10817–23, 2013.
- [74] Patrycja Dynarowicz-Latka and Katarzyna Hac-Wydro. Interactions between phosphatidylcholines and cholesterol in monolayers at the air/water interface. *Colloids and Surfaces B: Biointerfaces*, 37(1–2):21–25, 2004.
- [75] M. Emmer, H. J. Vos, M. Versluis, and N. de Jong. Radial modulation of single microbubbles. *IEEE Trans Ultrason Ferroelectr Freq Control*, 56(11):2370–9, 2009.
- [76] P. N. Burns, J. E. Powers, and T. Fritzsche. Harmonic imaging: A new imaging and Doppler method for contrast enhanced ultrasound. *Radiology*, 185:142, 1992.
- [77] N. de Jong, R. Cornet, and C. T. Lancée. Higher harmonics of vibrating gas-filled microspheres. Part two: measurements. *Ultrasonics*, 32(6):455–459, 1994.
- [78] O. Lotsberg, J. M. Hovem, and B. Aksum. Experimental observation of subharmonic oscillations in Infuson bubbles. *Journal of the Acoustical Society of America*, 99(3):1366–1369, 1996.
- [79] J. Sijl, B. Dollet, M. Overvelde, V. Garbin, T. Rozendal, N. de Jong, D. Lohse, and M. Versluis. Subharmonic behavior of phospholipid-coated ultrasound contrast agent microbubbles. *J Acoust Soc Am*, 128(5):3239–52, 2010.
- [80] D. H. Simpson, C. T. Chin, and P. N. Burns. Pulse inversion Doppler: a new method for detecting nonlinear echoes from microbubble contrast agents. *IEEE Trans Ultrason Ferroelectr Freq Control*, 46(2):372–82, 1999.

- [81] J. K. Willmann, R. Paulmurugan, K. Chen, O. Gheysens, M. Rodriguez-Porcel, A. M. Lutz, I. Y. Chen, X. Chen, and S. S. Gambhir. US imaging of tumor angiogenesis with microbubbles targeted to vascular endothelial growth factor receptor type 2 in mice. *Radiology*, 246(2):508–18, 2008.
- [82] M. A. Pysz, K. Foygel, J. Rosenberg, S. S. Gambhir, M. Schneider, and J. K. Willmann. Antiangiogenic cancer therapy: monitoring with molecular US and a clinically translatable contrast agent (BR55). *Radiology*, 256(2):519–27, 2010.
- [83] A. A. Doinikov, S. Zhao, and P. A. Dayton. Modeling of the acoustic response from contrast agent microbubbles near a rigid wall. *Ultrasonics*, 49(2):195–201, 2009.
- [84] P. A. Dayton, K. E. Morgan, A. L. Klibanov, G. H. Brandenburger, and K. W. Ferrara. Optical and acoustical observations of the effects of ultrasound on contrast agents. *IEEE Trans Ultrason Ferroelectr Freq Control*, 46(1):220–32, 1999.
- [85] B. J. Schmidt, I. Sousa, A. A. van Beek, and M. R. Bohmer. Adhesion and ultrasound-induced delivery from monodisperse microbubbles in a parallel plate flow cell. *Journal of Controlled Release*, 131(1):19–26, 2008.
- [86] T. G. Leighton. The acoustic bubble. *Academic Press*, 1994.
- [87] V. Garbin, M. Overvelde, B. Dollet, N. de Jong, D. Lohse, and M. Versluis. Unbinding of targeted ultrasound contrast agent microbubbles by secondary acoustic forces. *Phys Med Biol*, 56(19):6161–6177, 2011.
- [88] E. Y. Park, M. J. Smith, E. S. Stropp, K. R. Snapp, J. A. DiVietro, W. F. Walker, D. W. Schmidtke, S. L. Diamond, and M. B. Lawrence. Comparison of PSGL-1 microbead and neutrophil rolling: microvillus elongation stabilizes P-selectin bond clusters. *Biophys J*, 82(4):1835–47, 2002.

- [89] H. J. Vos, B. Dollet, M. Versluis, and N. de Jong. Nonspherical shape oscillations of coated microbubbles in contact with a wall. *Ultrasound in Medicine and Biology*, 37(6):935–948, 2011.
- [90] V. Garbin, B. Dollet, M. Overvelde, D. Cojoc, E. Di Fabrizio, L. van Wijngaarden, A. Prosperetti, N. de Jong, D. Lohse, and M. Versluis. History force on coated microbubbles propelled by ultrasound. *Physics of Fluids*, 21(9):–, 2009.
- [91] Lawrence A. Crum. Bjerknes forces on bubbles in a stationary sound field. *The Journal of the Acoustical Society of America*, 57(6):1363–1370, 1975.
- [92] C. D. Ohl, A. Tjink, and A. Prosperetti. The added mass of an expanding bubble. *Journal of Fluid Mechanics*, 482:271–290, 2003.
- [93] L. D. Landau and E. M. Lifshitz. Fluid mechanics, 2nd edition. *Pergamon Press*, 1987.
- [94] F. Takemura and J. Magnaudet. The history force on a rapidly shrinking bubble rising at finite Reynolds number. *Physics of Fluids*, 16(9):3247–3255, 2004.
- [95] P. Marmottant, S. van der Meer, M. Emmer, M. Versluis, N. de Jong, S. Hilgenfeldt, and D. Lohse. A model for large amplitude oscillations of coated bubbles accounting for buckling and rupture. *Journal of the Acoustical Society of America*, 118(6):3499–3505, 2005.
- [96] V. Garbin, D. Cojoc, E. Ferrari, E. Di Fabrizio, M. L. J. Overvelde, S. M. van der Meer, N. de Jong, D. Lohse, and M. Versluis. Changes in microbubble dynamics near a boundary revealed by combined optical micromanipulation and high-speed imaging. *Applied Physics Letters*, 90(11):114103, 2007.
- [97] C. T. Chin, C. Lancee, J. Borsboom, F. Mastik, M. E. Frijlink, N. de Jong, M. Versluis, and D. Lohse. Brandaris 128: A digital 25 million frames per second camera with 128 highly sensitive frames. *Review of Scientific Instruments*, 74(12):5026–5034, 2003.

-
- [98] S. M. van der Meer, B. Dollet, M. M. Voormolen, C. T. Chin, A. Bouakaz, N. de Jong, M. Versluis, and D. Lohse. Microbubble spectroscopy of ultrasound contrast agents. *Journal of the Acoustical Society of America*, 121(1):648–656, 2007.
- [99] J. Leach, H. Mushfique, S. Keen, R. Di Leonardo, G. Ruocco, J. M. Cooper, and M. J. Padgett. Comparison of Faxen’s correction for a microsphere translating or rotating near a surface. *Physical Review E*, 79(2), 2009.
- [100] S. S. Ozarkar and A. S. Sangani. A method for determining Stokes flow around particles near a wall or in a thin film bounded by a wall and a gas-liquid interface. *Physics of Fluids*, 20(6), 2008.
- [101] G. I. Bell. Models for the specific adhesion of cells to cells. *Science*, 200(4342):618–27, 1978.
- [102] D. A. Hammer and S. M. Apte. Simulation of cell rolling and adhesion on surfaces in shear flow: general results and analysis of selectin-mediated neutrophil adhesion. *Biophys J*, 63(1):35–57, 1992.
- [103] K. C. Chang and D. A. Hammer. Adhesive dynamics simulations of sialyl-Lewis(x)/E-selectin-mediated rolling in a cell-free system. *Biophys J*, 79(4):1891–902, 2000.
- [104] E. Evans and K. Ritchie. Dynamic strength of molecular adhesion bonds. *Biophys J*, 72(4):1541–55, 1997.
- [105] R. Merkel, P. Nassoy, A. Leung, K. Ritchie, and E. Evans. Energy landscapes of receptor-ligand bonds explored with dynamic force spectroscopy. *Nature*, 397(6714):50–3, 1999.
- [106] C. Ounkomol, H. Xie, P. A. Dayton, and V. Heinrich. Versatile horizontal force probe for mechanical tests on pipette-held cells, particles, and membrane capsules. *Biophys J*, 96(3):1218–31, 2009.
- [107] D. Garrivier, E. Decave, Y. Brechet, F. Bruckert, and B. Fourcade. Peeling model for cell detachment. *Eur Phys J E Soft Matter*, 8(1):79–97, 2002.

- [108] B. A. Naaijkens, A. van Dijk, O. Kamp, P. A. Krijnen, H. W. Niessen, and L. J. Juffermans. Therapeutic application of adipose derived stem cells in acute myocardial infarction: Lessons from animal models. *Stem Cell Rev*, 10(3):389–398, 2014.
- [109] A. B. Carvalho and A. C. de Carvalho. Heart regeneration: Past, present and future. *World J Cardiol*, 2(5):107–11, 2010.
- [110] K. D. Poss, L. G. Wilson, and M. T. Keating. Heart regeneration in zebrafish. *Science*, 298(5601):2188–90, 2002.
- [111] O. Bergmann, R. D. Bhardwaj, S. Bernard, S. Zdunek, F. Barnabe-Heider, S. Walsh, J. Zupicich, K. Alkass, B. A. Buchholz, H. Druid, S. Jovinge, and J. Frisen. Evidence for cardiomyocyte renewal in humans. *Science*, 324(5923):98–102, 2009.
- [112] H. C. Quevedo, K. E. Hatzistergos, B. N. Oskouei, G. S. Feigenbaum, J. E. Rodriguez, D. Valdes, P. M. Pattany, J. P. Zambrano, Q. Hu, I. McNiece, A. W. Heldman, and J. M. Hare. Allogeneic mesenchymal stem cells restore cardiac function in chronic ischemic cardiomyopathy via trilineage differentiating capacity. *Proc Natl Acad Sci U S A*, 106(33):14022–7, 2009.
- [113] G. V. Silva, S. Litovsky, J. A. R. Assad, A. L. S. Sousa, B. J. Martin, D. Vela, S. C. Coulter, J. Lin, J. Ober, W. K. Vaughn, R. V. C. Branco, E. M. Oliveira, R. M. He, Y. J. Geng, J. T. Willerson, and E. C. Perin. Mesenchymal stem cells differentiate into an endothelial phenotype, enhance vascular density, and improve heart function in a canine chronic ischemia model. *Circulation*, 111(2):150–156, 2005.
- [114] Y. L. Tang, Q. Zhao, Y. C. Zhang, L. Cheng, M. Liu, J. Shi, Y. Z. Yang, C. Pan, J. Ge, and M. I. Phillips. Autologous mesenchymal stem cell transplantation induce VEGF and neovascularization in ischemic myocardium. *Regul Pept*, 117(1):3–10, 2004.
- [115] M. Gnecci, Z. Zhang, A. Ni, and V. J. Dzau. Paracrine mechanisms in adult stem cell signaling and therapy. *Circ Res*, 103(11):1204–19, 2008.

- [116] I. M. Barbash, P. Chouraqui, J. Baron, M. S. Feinberg, S. Etzion, A. Tesone, L. Miller, E. Guetta, D. Zipori, L. H. Kedes, R. A. Kloner, and J. Leor. Systemic delivery of bone marrow-derived mesenchymal stem cells to the infarcted myocardium: feasibility, cell migration, and body distribution. *Circulation*, 108(7):863–8, 2003.
- [117] M. Hofmann, K. C. Wollert, G. P. Meyer, A. Menke, L. Arseniev, B. Hertenstein, A. Ganser, W. H. Knapp, and H. Drexler. Monitoring of bone marrow cell homing into the infarcted human myocardium. *Circulation*, 111(17):2198–2202, 2005.
- [118] J. Bartunek, W. Sherman, M. Vanderheyden, F. Fernandez-Aviles, W. Wijns, and A. Terzic. Delivery of biologics in cardiovascular regenerative medicine. *Clinical Pharmacology and Therapeutics*, 85(5):548–552, 2009.
- [119] V. F. Segers, I. Van Riet, L. J. Andries, K. Lemmens, M. J. Demolder, A. J. De Becker, M. M. Kockx, and G. W. De Keulenaer. Mesenchymal stem cell adhesion to cardiac microvascular endothelium: activators and mechanisms. *Am J Physiol Heart Circ Physiol*, 290(4):H1370–7, 2006.
- [120] A. Ghanem, C. Steingen, F. Brenig, F. Funcke, Z. Y. Bai, C. Hall, C. T. Chin, G. Nickenig, W. Bloch, and K. Tiemann. Focused ultrasound-induced stimulation of microbubbles augments site-targeted engraftment of mesenchymal stem cells after acute myocardial infarction. *J Mol Cell Cardiol*, 47(3):411–8, 2009.
- [121] F. H. Seeger, A. M. Zeiher, and S. Dimmeler. Cell-enhancement strategies for the treatment of ischemic heart disease. *Nat Clin Pract Cardiovasc Med*, 4 Suppl 1:S110–3, 2007.
- [122] J. Yamaguchi, K. F. Kusano, O. Masuo, A. Kawamoto, M. Silver, S. Murasawa, M. Bosch-Marce, H. Masuda, D. W. Losordo, J. M. Isner, and T. Asahara. Stromal cell-derived factor-1 effects on ex vivo expanded endothelial progenitor cell recruitment for ischemic neovascularization. *Circulation*, 107(9):1322–1328, 2003.

- [123] R. J. Lee, Q. Fang, P. A. Davol, Y. Gu, R. E. Sievers, R. C. Grabert, J. M. Gall, E. Tsang, M. S. Yee, H. Fok, N. F. Huang, J. F. Padbury, J. W. Larrick, and L. G. Lum. Antibody targeting of stem cells to infarcted myocardium. *Stem Cells*, 25(3):712–7, 2007.
- [124] J. H. Jeong, J. J. Schmidt, R. E. Kohman, A. T. Zill, R. J. DeVolder, C. E. Smith, M. H. Lai, A. Shkumatov, T. W. Jensen, L. G. Schook, S. C. Zimmerman, and H. Kong. Leukocyte-mimicking stem cell delivery via in situ coating of cells with a bioactive hyperbranched polyglycerol. *J Am Chem Soc*, 135(24):8770–3, 2013.
- [125] O. Levy, W. Zhao, L. J. Mortensen, S. Leblanc, K. Tsang, M. Fu, J. A. Phillips, V. Sagar, P. Anandakumaran, J. Ngai, C. H. Cui, P. Eimon, M. Angel, C. P. Lin, M. F. Yanik, and J. M. Karp. mRNA-engineered mesenchymal stem cells for targeted delivery of interleukin-10 to sites of inflammation. *Blood*, 122(14):e23–32, 2013.
- [126] L. E. Bayliss. The axial drift of the red cells when blood flows in a narrow tube. *J Physiol*, 149:593–613, 1959.
- [127] J. R. Lindner. Microbubbles in medical imaging: current applications and future directions. *Nature Reviews Drug Discovery*, 3(6):527–532, 2004.
- [128] P. J. Frinking, I. Tardy, M. Theraulaz, M. Arditi, J. Powers, S. Pochon, and F. Tranquart. Effects of acoustic radiation force on the binding efficiency of BR55, a VEGFR2-specific ultrasound contrast agent. *Ultrasound in Medicine and Biology*, 2012.
- [129] L. J. M. Juffermans. Ultrasound and microbubble-targeted delivery of drugs and genes: Cellular bioeffects and mechanisms. *Ph.D. thesis*, 2009.
- [130] L. J. M. Juffermans, A. van Dijk, B. A. Naaijken, T. J. A. Kokhuis, M. Hartevelde, R. J. P. Musters, V. W. M. van Hinsbergh, M. Helder, Kamp O., N. de Jong, and H. W. M. Niessen. Directing adipose derived stem cells to the area at risk in the heart after myocardial infarction using targeted

- microbubbles. *Abstract Book of the 15th European symposium on Ultrasound Contrast Imaging, 21-22 January 2010, Rotterdam, the Netherlands*, 2010.
- [131] B. A. Naaijkens, H. W. M. Niessen, H. J. Prins, P. A. J. Krijnen, T. J. A. Kokhuis, N. Jong, V. W. M. Hinsbergh, O. Kamp, M. N. Helder, R. J. P. Musters, A. Dijk, and L. J. M. Juffermans. Human platelet lysate as a fetal bovine serum substitute improves human adipose-derived stromal cell culture for future cardiac repair applications. *Cell and Tissue Research*, 348(1):119–130, 2012.
- [132] V. Hamburger and H. L. Hamilton. A series of normal stages in the development of the chick embryo. 1951. *Dev Dyn*, 195(4):231–72, 1992.
- [133] V. F. Segers and R. T. Lee. Stem-cell therapy for cardiac disease. *Nature*, 451(7181):937–42, 2008.
- [134] J. E. Chomas, P. A. Dayton, D. May, J. Allen, A. L. Klibanov, and K. Ferrara. Optical observation of contrast agent destruction. *Applied Physics Letters*, 77(7):1056–1058, 2000.
- [135] J. F. Beltrame, F. Crea, and P. Camici. Advances in coronary microvascular dysfunction. *Heart Lung Circ*, 18(1):19–27, 2009.
- [136] S. Kaul and H. Ito. Microvasculature in acute myocardial ischemia: part I: evolving concepts in pathophysiology, diagnosis, and treatment. *Circulation*, 109(2):146–9, 2004.
- [137] T. D. Miller, T. F. Christian, M. R. Hopfenspirger, D. O. Hodge, B. J. Gersh, and R. J. Gibbons. Infarct size after acute myocardial infarction measured by quantitative tomographic ^{99m}Tc sestamibi imaging predicts subsequent mortality. *Circulation*, 92(3):334–41, 1995.
- [138] A. Schmidt, D. Ladage, C. Steingen, K. Brixius, T. Schinkothe, F. J. Klinz, R. H. Schwinger, U. Mehlhorn, and W. Bloch. Mesenchymal stem cells transigrate over the endothelial barrier. *Eur J Cell Biol*, 85(11):1179–88, 2006.

- [139] W. A. Muller. Mechanisms of leukocyte transendothelial migration. *Annu Rev Pathol*, 6:323–44, 2011.
- [140] E. Chavakis and S. Dimmeler. Homing of progenitor cells to ischemic tissues. *Antioxid Redox Signal*, 15(4):967–80, 2011.
- [141] K. Cheng, D. Shen, Y. Xie, E. Cingolani, K. Malliaras, and E. Marban. Brief report: Mechanism of extravasation of infused stem cells. *Stem Cells*, 30(12):2835–42, 2012.
- [142] B. Wang, W. J. Zang, M. Wang, H. Ai, Y. W. Wang, Y. P. Li, G. S. He, L. Wang, and X. J. Yu. Prolonging the ultrasound signal enhancement from thrombi using targeted microbubbles based on sulfur-hexafluoride-filled gas. *Academic Radiology*, 13(4):428–433, 2006.
- [143] R. Basilio, M. J. K. Blomley, D. O. Cosgrove, J. B. Lull, A. Broillet, A. Bauer, and L. Bonomo. The first phase I study of a novel ultrasound contrast agent (BR14): Assessment of safety and efficacy in liver and kidneys. *Academic Radiology*, 9:S380–S381, 2002.
- [144] S. Zhao, M. Borden, S. H. Bloch, D. Kruse, K. W. Ferrara, and P. A. Dayton. Radiation-force assisted targeting facilitates ultrasonic molecular imaging. *Mol Imaging*, 3(3):135–48, 2004.
- [145] T. Segers and M. Versluis. Acoustic bubble sorting for ultrasound contrast agent enrichment. *Lab Chip*, 14(10):1705–14, 2014.
- [146] C. E. Murry, H. Reinecke, and L. M. Pabon. Regeneration gaps: observations on stem cells and cardiac repair. *J Am Coll Cardiol*, 47(9):1777–85, 2006.
- [147] K. Malliaras and E. Marban. Cardiac cell therapy: where we’ve been, where we are, and where we should be headed. *British Medical Bulletin*, 98(1):161–185, 2011.
- [148] P. A. Dayton, J. S. Allen, and K. W. Ferrara. The magnitude of radiation force on ultrasound contrast agents. *Journal of the Acoustical Society of America*, 112(5):2183–2192, 2002.

- [149] E. C. Gelderblom, H.J. Vos, F. Mastik, T. Faez, Y. Luan, T. J. A. Kokhuis, A. F. W. van der Steen, D. Lohse, N. de Jong, and M. Versluis. Brandaris 128 ultra-high-speed imaging facility: 10 years of operation, updates, and enhanced features. *Review of Scientific Instruments*, 83(10):103706, 2012.
- [150] R. Omta. Oscillations of a cloud of bubbles of small and not so small amplitude. *The Journal of the Acoustical Society of America*, 82(3):1018–1033, 1987.
- [151] N. de Jong, A. Bouakaz, and P. Frinking. Basic acoustic properties of microbubbles. *Echocardiography*, 19(3):229–240, 2002.
- [152] V.K. Shah and K.K. Shalia. Stem cell therapy in acute myocardial infarction: A pot of gold or Pandora’s box. *Stem Cells Int.*, 2011:536758, 2011.
- [153] K.C. Wollert, G.P. Meyer, J. Lotz, S. Ringes-Lichtenberg, P. Lippolt, C. Breidenbach, S. Fichtner, T. Korte, B. Hornig, D. Messinger, L. Arseniev, B. Hertenstein, A. Ganser, and H. Drexler. Intracoronary autologous bone-marrow cell transfer after myocardial infarction: the BOOST randomised controlled clinical trial. *Lancet*, 364(9429):141–148, 2004.
- [154] H. Rozemuller, H.J. Prins, B. Naaijken, J. Staal, H.J. Buhning, and A.C. Martens. Prospective isolation of mesenchymal stem cells from multiple mammalian species using cross-reacting anti-human monoclonal antibodies. *Stem Cells Dev.*, 19(12):1911–1921, 2010.
- [155] Dijk A. van, B.A. Naaijken, W.J. Jurgens, R. Oerlemans, G.L. Scheffer, J. Kassies, J. Aznou, M. Brouwer, A.C. van Rossum, G.J. Schuurhuis, F.J. van Milligen, and H.W. Niessen. The multidrug resistance protein breast cancer resistance protein (BCRP) protects adipose-derived stem cells against ischemic damage. *Cell Biol. Toxicol.*, 28(5):303–315, 2012.
- [156] P.A. Zuk, M. Zhu, H. Mizuno, J. Huang, J.W. Futrell, A.J. Katz, P. Benhaim, H.P. Lorenz, and M.H. Hedrick. Multilineage cells from human adipose tissue: implications for cell-based therapies. *Tissue Eng*, 7(2):211–228, 2001.

- [157] G.R. Berardi, C.K. Rebelatto, H.F. Tavares, M. Ingberman, P. Shiginov, F. Barchiki, A.M. Aguiar, N.I. Miyague, J.C. Francisco, A. Correa, A.C. Senegaglia, P.H. Suss, J.A. Moutinho, V.S. Sotomaior, L.S. Nakao, and P.S. Brofman. Transplantation of SNAP-treated adipose tissue-derived stem cells improves cardiac function and induces neovascularization after myocardium infarct in rats. *Exp.Mol.Pathol.*, 90(2):149–156, 2011.
- [158] A. van Dijk, B. A. Naaijkens, W. J. Jurgens, K. Nalliah, S. Sairras, R. J. van der Pijl, K. Vo, A. B. Vonk, A. C. van Rossum, W. J. Paulus, F. J. van Milligen, and H. W. Niessen. Reduction of infarct size by intravenous injection of uncultured adipose derived stromal cells in a rat model is dependent on the time point of application. *Stem Cell Res*, 7(3):219–29, 2011.
- [159] Y. Yamada, X.D. Wang, S. Yokoyama, N. Fukuda, and N. Takakura. Cardiac progenitor cells in brown adipose tissue repaired damaged myocardium. *Biochem.Biophys.Res.Comm.*, 342(2):662–670, 2006.
- [160] J. H. Houtgraaf, W. K. den Dekker, B. M. van Dalen, T. Springeling, R. de Jong, R. J. van Geuns, M. L. Geleijnse, F. Fernandez-Aviles, F. Zijlsta, P. W. Serruys, and H. J. Duckers. First experience in humans using adipose tissue-derived regenerative cells in the treatment of patients with ST-segment elevation myocardial infarction. *Journal of the American College of Cardiology*, 59(5):539–540, 2012.
- [161] S. Janssens, C. Dubois, J. Bogaert, K. Theunissen, C. Deroose, W. Desmet, M. Kalantzi, L. Herbots, P. Sinnaeve, J. Dens, J. Maertens, F. Rademakers, S. Dymarkowski, O. Gheysens, Cleemput J. Van, G. Bormans, J. Nuyts, A. Belmans, L. Mortelmans, M. Boogaerts, and F. Van de Werf. Autologous bone marrow-derived stem-cell transfer in patients with ST-segment elevation myocardial infarction: double-blind, randomised controlled trial. *Lancet*, 367(9505):113–121, 2006.

- [162] V. Schachinger, S. Erbs, A. Elsasser, W. Haberbosch, R. Hambrecht, H. Holschermann, J. Yu, R. Corti, D.G. Mathey, C.W. Hamm, T. Suselbeck, B. Assmus, T. Tonn, S. Dimmeler, and A.M. Zeiher. Intracoronary bone marrow-derived progenitor cells in acute myocardial infarction. *N.Engl.J.Med.*, 355(12):1210–1221, 2006.
- [163] A.R. Williams and J.M. Hare. Mesenchymal stem cells: biology, pathophysiology, translational findings, and therapeutic implications for cardiac disease. *Circ.Res.*, 109(8):923–940, 2011.
- [164] V. Benson, A.C. McMahon, and H.C. Lowe. ICAM-1 in acute myocardial infarction: a potential therapeutic target. *Curr.Mol.Med.*, 7(2):219–227, 2007.
- [165] M.A. Pfeffer, J.M. Pfeffer, M.C. Fishbein, P.J. Fletcher, J. Spadaro, R.A. Kloner, and E. Braunwald. Myocardial infarct size and ventricular function in rats. *Circ.Res.*, 44(4):503–512, 1979.
- [166] X. M. Gao, A. M. Dart, E. Dewar, G. Jennings, and X. J. Du. Serial echocardiographic assessment of left ventricular dimensions and function after myocardial infarction in mice. *Cardiovasc Res*, 45(2):330–8, 2000.
- [167] R. S. Vasan, M. G. Larson, E. J. Benjamin, J. C. Evans, and D. Levy. Left ventricular dilatation and the risk of congestive heart failure in people without myocardial infarction. *New England Journal of Medicine*, 336(19):1350–1355, 1997.
- [168] L.G. Lum, H. Fok, R. Sievers, M. Abedi, P.J. Quesenberry, and R.J. Lee. Targeting of Lin-Sca+ hematopoietic stem cells with bispecific antibodies to injured myocardium. *Blood Cells Mol.Dis.*, 32(1):82–87, 2004.
- [169] A.A. Karpov, Y.K. Uspenskaya, S.M. Minasian, M.V. Puzanov, R.I. Dmitrieva, A.A. Bilibina, S.V. Anisimov, and M.M. Galagudza. The effect of bone marrow- and adipose tissue-derived mesenchymal stem cell transplantation on myocardial remodelling in the rat model of ischaemic heart failure. *Int.J.Exp.Pathol.*, 94(3):169–177, 2013.

- [170] J.G. Rasmussen, O. Frobert, C. Holst-Hansen, J. Kastrup, U. Baandrup, V. Zachar, T. Fink, and U. Simonsen. Comparison of human adipose-derived stem cells and bone marrow-derived stem cells in a myocardial infarction model. *Cell Transplant.*, 2012.
- [171] L. Wang, J. Deng, W. Tian, B. Xiang, T. Yang, G. Li, J. Wang, M. Gruwel, T. Kashour, J. Rendell, M. Glogowski, B. Tomanek, D. Freed, R. Deslauriers, R.C. Arora, and G. Tian. Adipose-derived stem cells are an effective cell candidate for treatment of heart failure: an MR imaging study of rat hearts. *Am.J.Physiol Heart Circ.Physiol*, 297(3):H1020–H1031, 2009.
- [172] X. Zhang, H. Wang, X. Ma, A. Adila, B. Wang, F. Liu, B. Chen, C. Wang, and Y. Ma. Preservation of the cardiac function in infarcted rat hearts by the transplantation of adipose-derived stem cells with injectable fibrin scaffolds. *Exp.Biol.Med.(Maywood.)*, 235(12):1505–1515, 2010.
- [173] J. Dorner, R. Struck, S. Zimmer, C. Peigney, G.D. Duerr, O. Dewald, S.C. Kim, D. Malan, T. Bettinger, G. Nickenig, and A. Ghanem. Ultrasound-mediated stimulation of microbubbles after acute myocardial infarction and reperfusion ameliorates left-ventricular remodelling in mice via improvement of borderzone vascularization. *PLoS One*, 8(2):e56841, 2013.
- [174] A.C. Assis, J.L. Carvalho, B.A. Jacoby, R.L. Ferreira, P. Castanheira, S.O. Diniz, V.N. Cardoso, A.M. Goes, and A.J. Ferreira. Time-dependent migration of systemically delivered bone marrow mesenchymal stem cells to the infarcted heart. *Cell Transplant.*, 19(2):219–230, 2010.
- [175] D.L. Kraitchman, M. Tatsumi, W.D. Gilson, T. Ishimori, D. Kedziorek, P. Walczak, W.P. Segars, H.H. Chen, D. Fritzges, I. Izbudak, R.G. Young, M. Marcelino, M.F. Pittenger, M. Solaiyappan, R.C. Boston, B.M. Tsui, R.L. Wahl, and J.W. Bulte. Dynamic imaging of allogeneic mesenchymal stem cells trafficking to myocardial infarction. *Circulation*, 112(10):1451–1461, 2005.

- [176] J. Ma, J. Ge, S. Zhang, A. Sun, J. Shen, L. Chen, K. Wang, and Y. Zou. Time course of myocardial stromal cell-derived factor 1 expression and beneficial effects of intravenously administered bone marrow stem cells in rats with experimental myocardial infarction. *Basic Res. Cardiol.*, 100(3):217–223, 2005.
- [177] X. Bai, Y. Yan, Y.H. Song, M. Seidensticker, B. Rabinovich, R. Metzeler, J.A. Bankson, D. Vykoukal, and E. Alt. Both cultured and freshly isolated adipose tissue-derived stem cells enhance cardiac function after acute myocardial infarction. *Eur. Heart J.*, 31(4):489–501, 2010.
- [178] T. Ben-Mordechai, R. Holbova, N. Landa-Rouben, T. Harel-Adar, M.S. Feinberg, I.A. Elrahman, G. Blum, F. Epstein, Z. Silman, S. Cohen, and J. Leor. Macrophage subpopulations are essential for infarct repair with and without stem cell therapy. *J. Am. Coll. Cardiol.*, 62(20):1890–901.
- [179] V. Dayan, G. Yannarelli, F. Billia, P. Filomeno, X.H. Wang, J.E. Davies, and A. Keating. Mesenchymal stromal cells mediate a switch to alternatively activated monocytes/macrophages after acute myocardial infarction. *Basic Res. Cardiol.*, 106(6):1299–1310, 2011.
- [180] N. Joyce, G. Annett, L. Wirthlin, S. Olson, G. Bauer, and J.A. Nolte. Mesenchymal stem cells for the treatment of neurodegenerative disease. *Regen. Med.*, 5(6):933–946, 2010.
- [181] A. Needles, O. Couture, and F. S. Foster. A method for differentiating targeted microbubbles in real time using subharmonic micro-ultrasound and interframe filtering. *Ultrasound Med Biol*, 35(9):1564–73, 2009.
- [182] S. Wang, J. A. Hossack, A. L. Klibanov, and Jr. Mauldin, F. W. Binding dynamics of targeted microbubbles in response to modulated acoustic radiation force. *Phys Med Biol*, 59(2):465–84, 2014.
- [183] N. de Jong, R. Cornet, and C. T. Lancée. Higher harmonics of vibrating gas-filled microspheres. Part one: simulations. *Ultrasonics*, 32(6):447–453, 1994.

- [184] C. C. Church. The effects of an elastic solid surface layer on the radial pulsations of gas bubbles. *The Journal of the Acoustical Society of America*, 97(3):1510–1521, 1995.
- [185] A. A. Doinikov, L. Aired, and A. Bouakaz. Dynamics of a contrast agent microbubble attached to an elastic wall. *IEEE Trans Med Imaging*, 31(3):654–62, 2012.
- [186] B. L. Helfield, E. Cherin, F. S. Foster, and D. E. Goertz. The effect of binding on the subharmonic emissions from individual lipid-encapsulated microbubbles at transmit frequencies of 11 and 25 MHz. *Ultrasound Med Biol*, 39(2):345–59, 2013.
- [187] J. E. Leeman, J. S. Kim, F. T. Yu, X. Chen, K. Kim, J. Wang, F. S. Villanueva, and J. J. Pacella. Effect of acoustic conditions on microbubble-mediated microvascular sonothrombolysis. *Ultrasound Med Biol*, 38(9):1589–98, 2012.
- [188] T. J. A. Kokhuis, Y. Luan, F. Mastik, R. H. S. H. Beurskens, M. Versluis, and N. de Jong. Segmented high speed imaging of vibrating microbubbles during long ultrasound pulses. *2012 IEEE International Ultrasonics Symposium (IUS)*, pages 1343–1346, 2012.
- [189] L. M. Barbosa da Fonseca, B. Gutfilen, P. H. Rosado de Castro, V. Battistella, R. C. Goldenberg, T. Kasai-Brunswick, C. L. Chagas, E. Wajnberg, A. Maiolino, S. Salles Xavier, C. Andre, R. Mendez-Otero, and G. R. de Freitas. Migration and homing of bone-marrow mononuclear cells in chronic ischemic stroke after intra-arterial injection. *Exp Neurol*, 221(1):122–8, 2010.
- [190] B. Vrtovec, G. Poglajen, L. Lezaic, M. Sever, A. Socan, D. Domanovic, P. Cernelc, G. Torre-Amione, F. Haddad, and J. C. Wu. Comparison of transendocardial and intracoronary CD34+ cell transplantation in patients with nonischemic dilated cardiomyopathy. *Circulation*, 128(11 Suppl 1):S42–9, 2013.

- [191] P. K. Nguyen, J. Riegler, and J. C. Wu. Stem cell imaging: from bench to bedside. *Cell Stem Cell*, 14(4):431–44, 2014.
- [192] W. Cui, S. Tavri, M. J. Benchimol, M. Itani, E. S. Olson, H. Zhang, M. Decyk, R. G. Ramirez, C. V. Barback, Y. Kono, and R. F. Mattrey. Neural progenitor cells labeling with microbubble contrast agent for ultrasound imaging in vivo. *Biomaterials*, 34(21):4926–35, 2013.
- [193] S. I. Simon and G. W. Schmid-Schonbein. Biophysical aspects of microsphere engulfment by human neutrophils. *Biophys J*, 53(2):163–73, 1988.
- [194] O. Couture, S. Bannouf, G. Montaldo, J. F. Aubry, M. Fink, and M. Tanter. Ultrafast imaging of ultrasound contrast agents. *Ultrasound Med Biol*, 35(11):1908–16, 2009.
- [195] P. Tortoli, F. Guidi, R. Mori, and H. J. Vos. The use of microbubbles in Doppler ultrasound studies. *Med Biol Eng Comput*, 47(8):827–38, 2009.
- [196] P. Tortoli, D. Bagnai, and D. Righi. Quantitative analysis of Doppler spectrum modifications yielded by contrast agents insonified at high pressure. *IEEE Trans Ultrason Ferroelectr Freq Control*, 46(1):247–51, 1999.
- [197] L. J. M. Juffermans, O. Kamp, P. A. Dijkmans, C. A. Visser, and R. J. Musters. Low-intensity ultrasound-exposed microbubbles provoke local hyperpolarization of the cell membrane via activation of BK(Ca) channels. *Ultrasound Med Biol*, 34(3):502–8, 2008.
- [198] P. van Vliet, T. P. de Boer, M. A. van der Heyden, M. K. El Tamer, J. P. Sluijter, P. A. Doevendans, and M. J. Goumans. Hyperpolarization induces differentiation in human cardiomyocyte progenitor cells. *Stem Cell Rev*, 6(2):178–85, 2010.
- [199] X. Chen, J. M. Wan, and A. C. Yu. Sonoporation as a cellular stress: induction of morphological repression and developmental delays. *Ultrasound Med Biol*, 39(6):1075–86, 2013.

-
- [200] G. M. Lanza and S. A. Wickline. Targeted ultrasonic contrast agents for molecular imaging and therapy. *Curr Probl Cardiol*, 28(12):625–53, 2003.

Summary

Blood is a poor ultrasound scatterer and can not be visualized with ultrasound. To enhance the backscattering of the blood, ultrasound contrast agent (UCA) microbubbles can be injected intravenously. These microbubbles are typically 1 – 10 μm in size and consist of a gas core, coated by a lipid, polymer or protein shell for increased stability. Microbubbles exhibit volumetric oscillations in response to the incoming ultrasound waves. It is this vibration, in combination with the large difference in compressibility with the surrounding tissue, that makes these microbubbles excellent ultrasound scatterers.

Microbubbles can also be equipped with ligands against disease specific targets *in vivo*, creating so called *targeted microbubbles*. After injection, these targeted microbubbles will bind to the diseased target area. The concentration of these echogenic microbubbles at the target site produces a strong backscattering signal during ultrasound examination, facilitating *molecular ultrasound imaging*. Moreover, by loading drugs into or onto the bubble, which can be released upon ultrasound insonification, diagnosis can be combined with treatment using the very same microbubble population. A general introduction to microbubbles and their diagnostic and therapeutic value is provided in **Chapter 1**.

In **Chapter 2** we characterized the binding area and shape of adherent microbubbles using high-resolution fluorescence microscopy. These studies were motivated by the fact that current models for bound microbubbles in fact represent microbubbles in contact with a wall. However, several studies have shown that binding has a major effect on the vibrational response of a bubble, presumably as a result of

the mechanical constraint imposed on the microbubbles by the binding area. We found a linear relation between the binding area radius (R_{bind}) and the resting radius of the microbubble before binding (R_0). Changing the main lipid component of the microbubble shell had a major impact on the binding area and shape of the bound bubbles, which most likely will also influence the acoustical behaviour of the microbubbles. The gained insights are of relevance to an improved understanding of the behaviour of targeted microbubbles upon binding and the development of improved models for adherent microbubbles.

Ultrasound application induces a strong interaction between vibrating microbubbles called secondary Bjerknes force. In **Chapter 3** we investigated the effects of this secondary Bjerknes force on adherent microbubbles using high-speed optical imaging. We observed that adherent microbubbles of similar size deformed toward each other under influence of the secondary Bjerknes force, but snapped back to their initial position after the ultrasound was turned off. For increasing magnitude of the secondary Bjerknes force, binding of the microbubbles was ruptured resulting in clustering of the bubbles. A hydrodynamic model captured the translational dynamics of the interacting microbubbles during and after ultrasound application.

In the second part of the thesis (**Chapter 4, 5 and 6**) we report on the development of a novel therapeutic application of targeted microbubbles: ultrasound-mediated local stem cell delivery. By coating the stem cells with microbubbles, echogenic complexes dubbed *StemBells* are created, which vibrate in response to incoming ultrasound waves. This vibration makes them very susceptible to acoustic radiation forces, which can be employed to propel circulating StemBells from the centerline of the vessel to the wall, increasing the number of stem cells delivered in the insonified area. The working principle of this technique was demonstrated using intravital microscopy in a chicken embryo and was described in **Chapter 4**. Only stem cells which were fully saturated with targeted microbubbles (i.e. > 30 bubbles/cell) could be propelled toward and arrested at the vessel wall.

In **Chapter 5** we have investigated the vibrational dynamics of these saturated StemBells in response to ultrasound application using high-speed optical imaging.

It was found that saturated StemBells are resonant at much lower driving frequencies than what might be expected based on the individual resonance behavior of the bubbles around the cell. A modified Rayleigh-Plesset equation, considering the total gas volume of the surrounding layer of microbubbles, captured the resonance behavior and vibrational dynamics of the saturated StemBells. The results of this particular study are useful for a further optimization of the delivery technique.

In **Chapter 6**, we have reported on a long-term functional study in rats, in which we investigated the feasibility of our StemBell technique for the repair of damaged cardiac tissue after an acute myocardial infarction (AMI). Importantly, none of the rats showed complications following the intravenous injection with StemBells and cells were successfully retrieved in the infarcted area. In the StemBell-treated rats the infarct size was reduced significantly by a striking 60% compared with the control group. For comparison, bare stem cells reduced the infarct size compared with the control group by 33%, but not significantly. Moreover, only the StemBell-treated group showed a trend towards improved cardiac functioning post-therapy. In conclusion, these findings show that the StemBell-platform is a promising tool to augment the outcome of stem cell therapy for cardiac repair after a myocardial infarction.

In this thesis we only focused two aspects offered by the microbubbles around the stem cell: (1) radiation force effects and (2) active targeting of the StemBells using dual-targeted microbubbles. However, the presence of the microbubbles also opens possibilities for ultrasound-mediated stem cell tracking. Ideas for potential detection mechanisms are discussed in **Chapter 7**.

Samenvatting

Beeldvorming met behulp van ultrageluid, beter bekend als echografie, wordt veelvuldig gebruikt in de medische wereld voor de visualisatie van interne lichaamsstructuren. De bekendste voorbeelden zijn de zwangerschapsecho's en hartecho's. Om een beeld te creëren worden herhaaldelijk korte, hoogfrequente geluidsgolven uitgezonden door een zogenaamde ultrageluid transducent, die via een aangebrachte gel contact maakt met het lichaam. Deze geluidsgolven, buiten het bereik van het menselijk gehoor, verplaatsten zich vervolgens door het lichaam en reflecteren daarbij op de diverse weefselovergangen in het lichaam. De gereflecteerde geluidsgolven (echo's) worden weer opgepikt door dezelfde transducent en worden vervolgens gebruikt om een beeld te vormen op het scherm. De tijd tussen het zenden en ontvangen van de geluidsgolven is daarbij een maat voor de diepte waarop de desbetreffende weefselovergang zich bevindt.

Bot is een goede reflector van ultrageluid en daarom uitstekend te visualiseren met behulp van echografie. Bloed daarentegen is een uitermate slechte ultrageluid reflector. Om de visualisatie van bloed te verbeteren zijn daarom zogenaamde ultrageluid contrastmiddelen ontwikkeld. Deze contrastmiddelen bevatten kleine gasballetjes (1-10 μm in diameter¹) die omgeven zijn door een dunne schil bestaande uit lipiden (vetachtige stoffen), eiwitten of een polymeer ter bevordering van de stabiliteit. Deze gasballetjes, ook wel microbellen genaamd, vertonen volumetrische oscillaties (trillingen) als gevolg van de excitatie door het ultrageluid, waardoor ze zelf weer een bron van geluid worden. Het zijn deze trillingen, in combinatie met de grote verschillen in compressibiliteit met het omringende weefsel, wat deze

¹Ter vergelijking: een menselijk haar heeft een diameter van 50-100 μm

microbellen tot uitstekende ultrageluid reflectoren maakt. Door deze microbellen te injecteren in de bloedbaan van de patiënt, kan de doorbloeding (perfusie) van organen uitstekend gevisualiseerd worden.

Door de microbellen uit te rusten met liganden aan de buitenkant van de schil, doorgaans een antilichaam, kunnen zogenaamde getargete microbellen worden gemaakt. Door de aanwezigheid van deze liganden zullen deze getargete microbellen alleen binden aan specifieke cellen in het lichaam, bijvoorbeeld cellen van beschadigd weefsel. Deze verhoogde concentratie microbellen produceert een sterk signaal tijdens de echografie, zodat moleculaire veranderingen als gevolg van een ziekte kunnen worden waargenomen. Deze techniek heet daarom ook wel moleculaire beeldvorming. Microbellen kunnen verder ook nog worden geladen met geneesmiddelen, welke kunnen worden vrijgegeven door aanstraling met ultrageluid. Hierdoor kan diagnose worden gecombineerd met behandeling, gebruikmakende van dezelfde populatie microbellen. **Hoofdstuk 1** geeft een algemene inleiding in de wereld van de medische microbellen, waarbij ook de diagnostische en therapeutische toepassingen aan bod komen.

Hoofdstuk 2 beschrijft de experimentele bepaling van het bindingsoppervlak en de vorm van gebonden microbellen gebruikmakende van hoge resolutie fluorescentie microscopie. De motivatie voor dit onderzoek resulteerde uit het feit dat de huidige modellen voor gebonden microbellen onvolledig zijn en in feite ongebonden microbellen in contact met een wand beschrijven. Echter, diverse experimentele studies hebben laten zien dat de binding alleen al een groot effect heeft op de respons van een microbel, vermoedelijk door de mechanische beperking ten gevolge van het bindingsoppervlak. In deze studie vonden we een lineaire relatie tussen de radius van het bindingsoppervlak (R_{bind}) en de initiële radius van de microbel voor de binding (R_0). Het vervangen van de belangrijkste lipide component van de schil van de microbel had een groot effect op het bindingsoppervlak en vorm van de gebonden microbellen, wat hoogstwaarschijnlijk ook gevolgen zal hebben voor het akoestisch gedrag van de microbellen. De inzichten verworven in deze studie dragen bij aan een beter begrip van het gedrag van gebonden microbellen, wat de ontwikkeling van verbeterde modellen zal bespoedigen.

Ultrageluid kan een sterke interactie teweegbrengen tussen vibrerende microbellen. Deze interactie staat ook wel bekend als de *secundaire Bjerknæs kracht*. In **Hoofdstuk 3** hebben we het effect van deze kracht op gebonden microbellen onderzocht gebruikmakende van de Brandaris128 hogesnelheidscamera. Onze observatie was dat vibrerende microbellen van soortgelijke grootte elkaar aantrekken. Als gevolg van deze aantrekking deformeert een gebonden microbel in de richting van zijn naburige microbel. Echter, zodra het ultrageluid wordt uitgezet, schieten de bellen weer terug naar hun beginpositie. Voor hogere akoestische drukken (en dus grotere secundaire Bjerknæs krachten) kan de binding van de microbellen worden verbroken, wat uiteindelijk resulteert in een cluster van microbellen. We laten zien dat de verplaatsingsdynamica van gebonden microbellen onder invloed van deze secundaire Bjerknæs kracht kan worden voorspeld door een hydrodynamisch model.

In het tweede deel van dit proefschrift (**Hoofdstuk 4, 5 and 6**) beschrijven we een nieuwe therapeutische toepassing van getargete microbellen: lokale stamcel afgifte met behulp van ultrageluid. Door de buitenkant van de stamcellen te voorzien van een laagje microbellen, kunnen echogene complexen genaamd *StemBells* worden gevormd. Net als microbellen, vibreren deze StemBells zodra ze worden aangestraald met ultrageluid. Deze vibratie maakt de StemBells zeer vatbaar voor akoestische stuwkracht. De stuwkracht kan vervolgens worden gebruikt om langstromende StemBells richting de wand van een bloedvat te sturen waar ze kunnen binden aan endotheelcellen. Dit verhoogt daardoor de afgifte van stamcellen in de met ultrageluid behandelde regio, bijvoorbeeld het infarctgebied. Om het werkingsprincipe van deze techniek te demonstreren hebben we gebruik gemaakt van intravitale microscopie in een kippenembryo. De resultaten staan beschreven in **Hoofdstuk 4**.

In **Hoofdstuk 5** geven we een experimentele en theoretische beschrijving van het resonantiegedrag van StemBells. Voor het experimentele gedeelte zijn hogesnelheidsopnames gemaakt van vibrerende StemBells bij verschillende ultrageluid frequenties. De resonantiefrequentie van StemBells bleek aanzienlijk lager te liggen dan wat verwacht mag worden op basis van het resonantiegedrag van individuele microbellen. Numerieke simulaties, gebruikmakende van een gemodificeerde

Rayleigh-Plesset vergelijking, laten zien dat deze verschuiving in de resonantiefrequentie begrepen kan worden door de laag met microbellen te beschouwen als één continue schil van gas. De resultaten beschreven in dit hoofdstuk zijn nuttig voor een verdere optimalisatie van de StemBell techniek.

In **Hoofdstuk 6** staan de resultaten van een lange termijn studie met ratten beschreven. In deze studie hebben we gekeken naar de effecten van verschillende behandelmethoden (waaronder StemBell-transplantatie) op zowel het herstel in contractiliteit van het hart als de grootte van het infarct. Hiervoor is gebruikt gemaakt van een infarctmodel in ratten, waarbij een kunstmatig infarct wordt geïnduceerd door een kransslagader gedurende 40 minuten af te binden. Een week na de inductie van het infarct kregen de ratten een intraveneuze injectie van ofwel: (1) placebovloeistof, (2) microbellen, (3) stamcellen of (4) StemBells. Ratten in de StemBell-groep hadden een 60% kleiner infarct vergeleken met de placebogroep. Ter vergelijking, in ratten behandeld met stamcellen alleen was de infarctgrootte reduceerd met een niet-significante 33%. Bovendien lieten de ratten in de StemBell-groep als enige een trend richting verbeterde contractiliteit van het hart zien. Het StemBell-platform is dan ook een veelbelovend techniek om het herstel van de hartspier na een hartinfarct te verbeteren.

In dit proefschrift is met name gefocust op twee specifieke functies van de getargete bellen rondom de cel: (1) stamcellen vatbaar maken voor akoestische stuwkracht en (2) het actief targeten van stamcellen met behulp van dubbel-getargete microbellen. Echter, de aanwezigheid van de microbellen biedt ook mogelijkheden voor het detecteren en volgen (*tracken*) van stamcellen na injectie met behulp van ultrageluid. Ideeën voor detectiemethoden zijn beschreven in **Hoofdstuk 7**.

Dankwoord

De tied hold gen schoft ofwel de tijd houdt geen pauze, luidt een oude Twentse wijsheid. Mijn aio-periode bij de afdeling Biomedical Engineering is dan ook voorbij gevlogen. Ik kan me de zomeravond in 2009 nog goed herinneren toen ik mevrouw Pruijsten een brief schreef om te solliciteren op de PhD positie '*Local drug delivery and imaging of new therapeutic nanocarriers*'. Eenmaal op gesprek in Rotterdam bleek het onderwerp van het project te zijn veranderd in '*local stem cell delivery*', maar dat mocht de pret niet drukken. Dat ik hier te maken had met een inventieve afdeling, werd me trouwens al snel duidelijk uit de onconventionele vragen die me werden gesteld tijdens het interview: '*Wat is een coaxkabel?*' en '*Hoe ziet je bureau eruit?*' Ik kijk met ontzettend veel plezier terug op mijn promotieperiode. Naast een interessant project, was het namelijk een voorrecht om op de afdeling Biomedical Engineering te morgen werken. Een afdeling waar zelfs de vloerpolijstmachine ultrahoge snelheden kan halen (zie Figuur).



Figuur: De ultrasnelle vloerpolijstmachine van de afdeling Biomedical Engineering

Allereerst wil ik mijn promotoren Prof.dr.ir. Nico de Jong, Prof.dr.ir. Ton van der Steen en Prof.dr. Michel Versluis bedanken voor het vertrouwen en de goede begeleiding. Nico, jouw laagdrempelige karakter in combinatie met 30 jaar bubbelervaring zorgden altijd voor uitstekende wetenschappelijke discussies. Daarnaast

was je indien nodig altijd bereid om even mee te helpen met de Brandaris camera, waarvoor dank. Ton, ik heb veel respect voor de professionele wijze waarop je de afdeling runt. Bovendien vond ik het altijd erg leuk betrokken te worden bij het organiseren van diverse demonstraties voor bezoekers uit het bedrijfsleven. Michel, jouw kritische blik en expertise op het gebied van beldynamica waren van onschatbare waarde voor het StemBell-project. Naast goede promotoren waren jullie alledrie bovendien ook goed gezelschap tijdens de vele internationale conferenties.

The work presented in this thesis would not have been possible without the help of my direct colleagues, better known as *the bubble people*. Ying, you were a great colleague who was always willing to help, but above all you became a good friend. I will never forget the warm welcome by your family after Anke and I arrived in Nanjing, China. We had a great time. The Chinese martial arts performances of your grandfather were impressive. Skachkov, I really enjoyed working with you on the experiments in the chicken embryo. The moment we finally got this setup working after all the struggle was one of the best moments of my PhD. Besides that, you gave the word cell biologist another dimension with your in depth knowledge about cell phones. Thanks for being my paranymp during the defense. Jason, you joined our bubble-team as a guest scientist from Cincinnati during the final year of my PhD. Thanks for all the discussions and for showing us the Boston area after the ASA meeting. Good luck with finishing your thesis. Klazina, jij bedankt voor alle hulp en advies op het gebied van targetting, bellen, cellen en cursussen. Veel succes met je Veni-onderzoek. En Tom, bedankt voor je gezelschap in onze trench en succes met de tweede helft van je PhD.

Ook wil ik de technici Robert (*'Nicht verzagen, Robert fragen'*), Frits, Gerard, Jan, Charles, Hans Verdoes, Michiel en Geert bedanken voor alle technische ondersteuning de afgelopen jaren. Altijd wisten jullie weer een creatieve en werkende oplossing te verzinnen. Of het nou ging om de fabricatie van een flitslamp met een lichtsterkte waar een paard de hik van krijgt, een nieuwe waterbak of problemen met de 'mirrorpulse', altijd wist iemand van jullie weer een oplossing op maat te vinden.

Mieke, Gracia en Rita: bedankt voor jullie hulp en advies gedurende het hele promotietraject.

I also would like to thank Hans, Pieter, Verva(sonics), Rik, Alex, Zeynettin, Jacopo, Gijs, Guillaume, David, Deep, Muthu, Harm, Jelle, Lambert, Kim, Frank, Jolanda and all other (former) colleagues from the department of Biomedical Engineering for the good working atmosphere.

Uit Amsterdam wil ik graag Lynda, Benno, Hans en Otto bedanken voor de goede samenwerking binnen het StemBell-project. Anders dan in het voetbal, hebben we bewezen dat 010 en 020 prima samengaan.

From the Physics of Fluids group in Twente I would like to thank Erik, Alex, Tim, Guillaume, Marlies, Prof.dr. Leen van Wijngaarden and Prof.dr. Andrea Prosperetti for the good collaboration and discussions. I also would like to thank Valeria Garbin from the Imperial College London for the Skype and e-mail conversations about the dynamics of targeted microbubbles.

Ook wil ik mijn kameraden uit Twente, Nijmegen en Lombok bedanken voor alle gezelligheid door de jaren heen.

En dan mijn fantastische familie. Pa en ma, zonder jullie onvoorwaardelijke steun was dit proefschrift er nooit geweest. Jullie hebben mij altijd vrij gelaten en gesteund in de keuzes die ik maakte; ook als dat betekende dat ik naar Nijmegen wilde verhuizen terwijl er een universiteit 'om de hoek' lag. Coen en Rik, jullie zijn twee geweldige broers waar ik altijd op kan rekenen. Bovendien had ik me geen leukere schoonzussen kunnen wensen dan Ilse en Susan. En Madelief, Pepijn en Guusje, ravotten met jullie is de beste ontspanning. De skivakanties naar Biberwier met het hele gezin is altijd een van de hoogtepunten van het jaar. Ik hoop dat er nog vele skivakanties (al dan niet op de Gröbigen Alm) zullen volgen. Ook mijn schoonfamilie van der Wal wil ik bedanken voor de oprechte interesse en de altijd gezellige avondjes in Hedel.

Anke, ik weet dat je niet graag in de spotlight staat, maar ik ga deze dankbetuiging toch afsluiten met een paar woorden aan jou. Het feit dat ik jou heb leren

kennen in Nijmegen voelt nog steeds als een lot uit de loterij. Je hebt een groot hart en ik heb ongelooflijk veel respect hoe jij je inzet voor het welzijn van ouderen in Utrecht. Dit zegt veel over jou als persoon. Daarnaast ben je ook nog eens een begenadigd schilder, al zul je dit zelf altijd ten stelligste blijven ontkennen. Ik heb de afgelopen maanden steeds weer genoten van je creaties in onze studeerkamer als ik weer even over mijn laptop tuurde, op zoek naar goede zinsconstructies. Ik kijk uit naar aan onze toekomst samen...

Tom,

Utrecht, 26 september 2014

Publications and presentations

Peer-reviewed papers

- **T.J.A. Kokhuis**, I. Skachkov, B.A. Naaijken, L.J.M. Juffermans, O. Kamp, K. Kooiman, A.F.W. van der Steen, M. Versluis and N. de Jong. Intravital microscopy of localized stem cell delivery using microbubbles and acoustic radiation force *Biotechnology and Bioengineering*, in press, 2014.
- K. Kooiman, **T.J.A. Kokhuis**, T. van Rooij, I. Skachkov, A. Nigg, J.G. Bosch, A.F.W. van der Steen, W.A. van Cappellen and N. de Jong. DSPC or DPPC as main shell component influences ligand distribution and binding area of lipid-coated targeted microbubbles *European Journal of Lipid Science and Technology*, 116(9): 1217-1227, 2014.
- **T.J.A. Kokhuis**, V. Garbin, K. Kooiman, B.A. Naaijken, L.J.M. Juffermans, O. Kamp, A.F.W. van der Steen, M. Versluis and N. de Jong. Secondary Bjerknes forces deform targeted microbubbles. *Ultrasound in Medicine and Biology*, 39(3): 490-506, 2013.
- O. Shpak, **T.J.A. Kokhuis**, Y. Luan, D. Lohse, N. de Jong, B. Fowlkes, M. Fabiilli and M. Versluis. Ultrafast dynamics of the acoustic vaporization of phase-change microdroplets. *Journal of the Acoustical Society of America*, 134(2): 610-621, 2013.
- B.A. Naaijken, H.W.M. Niessen, H.J. Prins, P.A.J. Krijnen, **T.J.A. Kokhuis**, N. de Jong, V.W.M. van Hinsbergh, O. Kamp, M.N. Helder, R.J.P. Musters,

- A. van Dijk and L.J.M. Juffermans. Human platelet lysate as a fetal bovine serum substitute improves human adipose-derived stromal cell culture for future cardiac repair applications. *Cell and Tissue Research*, 348(1): 119-130, 2012.
- E.C. Gelderblom, H.J. Vos, F. Mastik, T. Faez, Y. Luan, **T.J.A. Kokhuis**, A.F.W. van der Steen, D. Lohse, N. de Jong and M. Versluis. Brandaris 128 ultra-high-speed imaging facility: 10 years of operation, updates, and enhanced features. *Review of scientific instruments*, 83(10):103706, 2012.

Papers in preparation for submission

- **T.J.A. Kokhuis**, B.A. Naaijken, L.J.M. Juffermans, O. Kamp, A.F.W. van der Steen, M. Versluis and N. de Jong. On the dynamics of StemBells: microbubble-conjugated stem cells for ultrasound-controlled delivery.
- B.A. Naaijken, **T.J.A. Kokhuis**, P.A.J. Krijnen, S.J.P. Bogaards, E. Meinster, I.A.E. Bollen, H. Baltzer, M.N. Helder, V.W.M. van Hinsbergh, R.J.P. Musters, N. de Jong, O. Kamp, H.W.M. Niessen, A. van Dijk and L.J.M. Juffermans. Directing stem cells to the infarcted area using targeted microbubbles: StemBells.
- I. Skachkov, **T.J.A. Kokhuis**, Y. Luan, A.F.W. van der Steen, N. de Jong and K. Kooiman. Cell membrane permeability dynamics after sonoporation.

Articles in conference proceedings

- **T.J.A. Kokhuis**, I. Skachkov, B.A. Naaijken, L.J.M. Juffermans, O. Kamp, A.F.W. van der Steen, M. Versluis and N. de Jong. Experimental and numerical investigation of microbubble-loaded stem cell dynamics during ultrasound exposure. *Proceedings IEEE International Ultrasonics Symposium*, Prague, Czech Republic, 2013.

- **T.J.A. Kokhuis**, Y. Luan, F. Mastik, R.H.S.H. Beurskens, M. Versluis and N. de Jong. Segmented high speed imaging of vibrating microbubbles during long ultrasound pulses. *Proceedings IEEE International Ultrasonics Symposium*, Dresden, Germany, 2012.
- **T.J.A. Kokhuis**, B.A. Naaijken, L.J.M. Juffermans, O. Kamp, M. Versluis and N. de Jong. Secondary Bjerknes forces deform targeted microbubbles. *Proceedings IEEE International Ultrasonics Symposium*, Dresden, Germany, 2012.
- K. Kooiman, **T.J.A. Kokhuis**, I. Skachkov, J.G. Bosch, A.F.W. van der Steen, W.A. van Cappellen and N. de Jong Surface contact of bound targeted microbubbles. *Proceedings IEEE International Ultrasonics Symposium*, Dresden, Germany, 2012.
- **T.J.A. Kokhuis**, V. Garbin, K. Kooiman, B.A. Naaijken, L.J.M. Juffermans, O. Kamp, A.F.W. van der Steen, M. Versluis and N. de Jong. Probing microbubble adhesion using secondary acoustic radiation force. *Proceedings IEEE International Ultrasonics Symposium*, Orlando, Florida, USA, 2011.
- K. Kooiman, M. Emmer, **T.J.A. Kokhuis**, J.G. Bosch, H.M. de Gruiter, M.E. van Royen, W.A. van Cappellen, A.B. Houtsmuller, A.F.W. van der Steen, N. de Jong. Lipid distribution and viscosity of coated microbubbles, *Proceedings IEEE International Ultrasonics Symposium*, San Diego, California, USA, 2010.

Oral presentations

- **T.J.A. Kokhuis**, I. Skachkov, B.A. Naaijken, L.J.M. Juffermans, O. Kamp, A.F.W. van der Steen, M. Versluis and N. de Jong. StemBells: localized stem cell delivery using targeted microbubbles and acoustic radiation force. 167th Meeting of the Acoustical Society of America, Providence, Rhode Island, USA, 2014.

- **T.J.A. Kokhuis**, I. Skachkov, B.A. Naaijken, L.J.M. Juffermans, O. Kamp, A.F.W. van der Steen, M. Versluis and N. de Jong. StemBells: localized stem cell delivery using targeted microbubbles and acoustic radiation force. Academic Expo, BCF Career Event, Amsterdam, the Netherlands, 2014.
- **T.J.A. Kokhuis**, I. Skachkov, B.A. Naaijken, L.J.M. Juffermans, O. Kamp, A.F.W. van der Steen, M. Versluis and N. de Jong. StemBells: localized stem cell delivery using microbubbles and acoustic radiation force. Spring Meeting of the Dutch Society for Medical Ultrasound, Enschede, the Netherlands, 2014.
- **T.J.A. Kokhuis**, I. Skachkov, B.A. Naaijken, L.J.M. Juffermans, O. Kamp, A.F.W. van der Steen, M. Versluis and N. de Jong. Intravital microscopy of localized stem cell delivery using microbubbles and acoustic radiation force. 19th European Symposium on Ultrasound Contrast Imaging, Rotterdam, the Netherlands, 2014.
- **T.J.A. Kokhuis**, B.A. Naaijken, L.J.M. Juffermans, O. Kamp, A.F.W. van der Steen, M. Versluis, N. de Jong. Experimental and numerical investigation of microbubble-loaded stem cell dynamics during ultrasound exposure. IEEE International Ultrasonics Symposium, Prague, Czech Republic, 2013.
- **T.J.A. Kokhuis**, B.A. Naaijken, L.J.M. Juffermans, O. Kamp, A.F.W. van der Steen, M. Versluis, N. de Jong. Dynamics of StemBells in an ultrasound field. International Symposium on Therapeutic Ultrasound, Shanghai, China, 2013.
- **T.J.A. Kokhuis**, B.A. Naaijken, L.J.M. Juffermans, O. Kamp, A.F.W. van der Steen, M. Versluis, N. de Jong. Dynamics of StemBells in an ultrasound field. 18th European symposium on Ultrasound Contrast Imaging, Rotterdam, the Netherlands, 2013.
- **T.J.A. Kokhuis**, V. Garbin, K. Kooiman, B.A. Naaijken, L.J.M. Juffermans, O. Kamp, M. Versluis and N. de Jong. Probing microbubble adhesion

using secondary acoustic radiation force. IEEE International Ultrasonics Symposium, Orlando, Florida, USA, 2011.

- **T.J.A. Kokhuis**, V. Garbin, K. Kooiman, B.A. Naaijken, L.J.M. Juffermans, O. Kamp, M. Versluis and N. de Jong. Detachment of targeted microbubbles using secondary acoustic radiation force. Spring Meeting of the Dutch Society for Medical Ultrasound, Delft, the Netherlands, 2011.
- **T.J.A. Kokhuis**, V. Garbin, K. Kooiman, B.A. Naaijken, L.J.M. Juffermans, O. Kamp, M. Versluis and N. de Jong. Detachment of targeted microbubbles under influence of secondary acoustic radiation force; 16th European symposium on Ultrasound Contrast Imaging, Rotterdam, the Netherlands, 2011.

Poster presentations

- **T.J.A. Kokhuis**, I. Skachkov, B.A. Naaijken, L.J.M. Juffermans, O. Kamp, A.F.W. van der Steen, M. Versluis and N. de Jong. StemBells: localized stem cell delivery using targeted microbubbles. Innovation for Health, Amsterdam, the Netherlands, 2014.
- **T.J.A. Kokhuis**, I. Skachkov, B.A. Naaijken, L.J.M. Juffermans, O. Kamp, A.F.W. van der Steen, M. Versluis and N. de Jong. StemBells: localized stem cell delivery using targeted microbubbles and acoustic radiation force. Academic Expo, BCF Career Event, Amsterdam, the Netherlands, 2014.
- **T.J.A. Kokhuis**, B.A. Naaijken, L.J.M. Juffermans, O. Kamp, A.F.W. van der Steen, M. Versluis, N. de Jong. StemBells: localized stem cell delivery using targeted microbubble. STW Annual Conference, Nieuwegein, the Netherlands, 2013.
- **T.J.A. Kokhuis**, B.A. Naaijken, L.J.M. Juffermans, O. Kamp, M. Versluis, and N. de Jong. Secondary Bjerknes forces deform targeted microbubbles. IEEE International Ultrasonics Symposium, Dresden, Germany, 2012.

- **T.J.A Kokhuis**, Y. Luan, F. Mastik, R.H.S.H. Beurskens, M. Versluis and N. de Jong. Segmented high speed imaging of vibrating microbubbles during long ultrasound pulses. IEEE International Ultrasonics Symposium, Dresden, Germany, 2012.
- **T.J.A. Kokhuis**, B.A. Naaijken, L.J.M. Juffermans, O. Kamp, M. Versluis and N. de Jong. Mutually interacting targeted microbubbles. Leeds Microbubble Symposium, United Kingdom, 2012.

Academic reports

- **T.J.A. Kokhuis**, StemBells: a novel stem cell delivery platform using microbubbles and ultrasound, PhD thesis, Erasmus University Rotterdam, the Netherlands, 2014.
- **T.J.A. Kokhuis**, Biogenic magnetite studied by scanning probe microscopy and magnetometry, MSc thesis, Radboud University Nijmegen, the Netherlands, 2007

Honors and awards

- Upcoming Scientist Award, Innovation for Health, Amsterdam, the Netherlands, 2014.
- Biomedical Acoustics Paper Award, 167th Meeting of the Acoustical Society of America, Providence, RI, USA, 2014
- Academic Expo Award, BCF Career Event, Amsterdam, the Netherlands, 2014.
- Student Travel Award, International Society for Therapeutic Ultrasound, Shanghai, China, 2013.

- Maney Publishing Award, Microbubble Symposium, Leeds, United Kingdom, 2012.

PhD portfolio

PhD training	Year	Workload (ECTS)
Courses		
Fluid mechanics (TU Delft, grade: A++)	2010	3
Cardiovascular Imaging and Diagnostics (COEUR)	2010	1.5
Animal Imaging Workshop (MolMed)	2011	1.4
Ultrasound contrast agents: theory and experimental results (IEEE, Orlando, USA)	2011	0.15
Ultrasound Imaging Systems: from principles to implementation (IEEE, Orlando, USA)	2011	0.15
Masterclass Presenting Research (KNAW)	2012	0.3
Plane Wave Imaging and Applications for Ultrafast Doppler, Elastography, and Contrast (IEEE, Prague, Czech Republic)	2013	0.15
Presentations		
The 16 th European Symposium on Ultrasound Contrast Imaging, Rotterdam, the Netherlands (Oral)	2011	1.0
Spring Meeting of the Dutch Society For Medical Ultrasound, Delft, the Netherlands (Oral)	2011	1.0
IEEE International Ultrasonics Symposium, Orlando, Florida, USA (Oral)	2011	1.0
Microbubble Symposium, Leeds, United Kingdom (Poster)	2012	0.5

IEEE International Ultrasonics Symposium, Dresden, Germany (Two posters)	2012	1.0
The 18 th European Symposium on Ultrasound Contrast Imaging, Rotterdam, the Netherlands (Oral)	2013	1.0
International Symposium on Therapeutic Ultrasound, Shanghai, China (Oral)	2013	1.0
STW Annual Conference, Nieuwegein, the Netherlands (Poster)	2013	0.5
IEEE International Ultrasonics Symposium, Prague, Czech Republic (Oral)	2013	1.0
The 19 th European Symposium on Ultrasound Contrast Imaging, Rotterdam, the Netherlands (Oral)	2014	1.0
Spring Meeting of the Dutch Society for Medical Ultrasound, Enschede, the Netherlands (Oral)	2014	1.0
Academic Expo, BCF Career Event, Amsterdam, the Netherlands (Poster + oral)	2014	1.5
Innovation for Health, Amsterdam, the Netherlands (Poster)	2014	0.5
167 th Meeting of the Acoustical Society of America, Providence, Rhode Island, USA (Poster + oral)	2014	1.5
Conferences		
The 15 th European Symposium on Ultrasound Contrast Imaging, Rotterdam, the Netherlands	2010	0.6
The 16 th European Symposium on Ultrasound Contrast Imaging, Rotterdam, the Netherlands	2011	0.6
IEEE International Ultrasonics Symposium, Orlando, Florida, USA	2011	0.9
The 17 th European Symposium on Ultrasound Contrast Imaging, Rotterdam, the Netherlands	2012	0.6
Microbubble Symposium, Leeds, United Kingdom	2012	0.6
IEEE International Ultrasonics Symposium, Dresden, Germany	2012	0.9
The 18 th European Symposium on Ultrasound Contrast Imaging, Rotterdam, the Netherlands	2013	0.6
International Symposium on Therapeutic Ultrasound, Shanghai, China	2013	0.9

IEEE International Ultrasonics Symposium, Prague, Czech Republic	2013	0.9
The 19 th European Symposium on Ultrasound Contrast Imaging, Rotterdam, the Netherlands	2014	0.6
Innovation for Health, Amsterdam, the Netherlands	2014	0.3
167 th Meeting of the Acoustical Society of America, Providence, Rhode Island, USA	2014	1.5

Research seminars

Spring Meeting of the Dutch Society for Medical Ultrasound, Enschede, the Netherlands	2010	0.3
Spring Meeting of the Dutch Society for Medical Ultrasound, Delft, the Netherlands	2011	0.3
Spring Meeting of the Dutch Society for Medical Ultrasound, Enschede, the Netherlands	2014	0.3

Teaching activities & Demonstrations

Lecture 'Ultrasound Molecular Imaging: oncology & cardiology applications' Biomedical Research Techniques Course (MolMed), Erasmus MC, Rotterdam, the Netherlands	2012	1.0
Demonstration Brandaris128-camera for the Translational Imaging Workshop (AMIE)	2011	0.3
Demonstration Brandaris128-camera for the Translational Imaging Workshop (AMIE)	2012	0.3
Demonstration Brandaris128-camera for the Translational Imaging Workshop (AMIE)	2013	0.3
Demonstration Brandaris128-camera for the Netherlands Academy of Technology and Innovation (AcTI)	2013	0.3

Total	32.25
--------------	--------------

About the author

Tom Kokhuis was born on November 16th, 1982, in Geesteren, a small village in the green countryside of Twente, the Netherlands. He obtained his pre-university diploma (Atheneum) in 2001 from the Scholengemeenschap St. Canisius in Almelo. The same year he started studying Natural Sciences at the Radboud University Nijmegen. In 2002 he obtained his propaedeutic



diploma with *cum laude* classification, after which he continued to work toward his MSc degree. His studies included several research internships. The first internship was performed at the Department of Cell and Applied Biology, where he studied the growth stage dependency of mitochondrial morphology in normal rat kidney fibroblasts using confocal laser scanning microscopy. The second internship was performed at the Department of Scanning Probe Microscopy. His project was concerned with investigating the (magnetic) properties of biogenic magnetic nanocrystals found in the nose and lateral line system of Atlantic Salmon (*Salmo salar*) and their potential role in magnetoreception. During his studies he was a member of the Activities Committee of the Natural Sciences Student Union "Leonardo da Vinci". In 2007 he obtained his MSc degree in Natural Sciences, with specialization in Biophysics. After graduation he started working at the Pharmacovigilance department of Organon Biosciences, Oss, the Netherlands, which

merged with Schering-Plough Pharmaceuticals in 2008.

In November 2009 he started his PhD studies at the Department of Biomedical Engineering, Erasmus Medical Center in Rotterdam, under the supervision of Prof. Dr. Ir. Nico de Jong, Prof. Dr. Ir. Antonius F.W. van der Steen and Prof. Dr. Michel Versluis. His research project focused on the development of a novel stem cell delivery platform using ultrasound and microbubbles and was conducted in close collaboration with the VU Medical Center in Amsterdam. The project was funded by the Dutch technology foundation Stichting Toegepaste Wetenschappen (STW). The results of the work are described in this thesis.

Tom Kokhuis will continue his career at Medtronic as a Technical Specialist for Cardiac Rhythm Disease Management (CRDM) devices. He lives together with Anke van der Wal in Utrecht, the Netherlands.

Wonderland

Bij het pompstation
bleken acht van de negen
pompen super te leveren
en maar één normaal

Op m'n vraag of het geen
tijd werd de bordjes te ver-
hangen keek de pompbediende
mij niet begrijpend aan

Toen ik later in een
etalage op een bord las
dat men bij aanschaf van
vijf batterijen één

staaflantaarn cadeau gaf
begreep ik dat ik
in de omgekeerde wereld
was beland.

Jules Deelder
uit: 'Interbellum', 1987

